

공학박사학위논문

판의 무기저 손상 탐지를 위한 압전소자와 보체계의  
동탄성학적 해석

Elasto-Dynamic Interpretation of a Coupled PZT Beam  
System for Reference-free Damage Diagnosis of a Plate

동아대학교 대학원

토 목 공 학 과

김 은 진

2011 학 년 도

Elasto-Dynamic Interpretation of a Coupled PZT  
Beam System for Reference-free Damage  
Diagnosis of a Plate

by

Kim, Eun-Jin

Submitted to

The Graduate School of Dong-A University in Partial Fulfillment of the

Requirements for the Degree of Doctor of Engineering

in

Civil Engineering

Jun. 2011

Elato-Dynamic Interpretation of a Coupled PZT Beam  
System for Reference-free Damage Diagnosis of a Plate

I have examined the final copy of this dissertation for format and content and recommend that it be accepted in partial fulfillment of the requirements for the degree of Doctor of Engineering, with a major in Civil Engineering.

---

Committee Chair Ph.D. Soo Bong Shin

We have read this dissertation(thesis) and recommend  
its acceptance :

---

---

Committee Vice-chair Dr. Hyun Woo Park

---

Committee Member Dr. Hyun Woo Park

---

Committee Member Dr. Hyun Woo Park

---

Committee Member Dr. Hyun Woo Park

## **Abstract**

### Elasto-Dynamic Interpretation of a Coupled PZT Beam System for Reference-free Damage Dignosis of a Plate

*by*  
*Kim, Eun-Jin*

*Dept. of Civil Engineering*  
*Graduate School, Dong-A University*  
*Busan, Korea*

This paper presents the elasto-dynamic interpretation of a coupled PZT beam system (CPBS) for reference-free damage dignosis of a plate. In particular, theoretical approaches on electro-mechanical (EM) signal for detecting damage are conducted in the perspective of the modal characteristics of a plate, and then the following reserches are proposed to overcome the limitation of previous impedance-based damage detection which requires the base signal associated with prestine condition of a plate.

In this paper, the EM signal is understood by elasto-dynamic correlation between Lamb wave(LW) and EM signals. The correlations between LW and EM signals are quantitatively investigated through the temporal spectrums and pulse superposition. A pair of identical piezoelectric (PZT) wafers collocated on a plate enable extraction of mode-converted signal due to their polarization characteristics.

Through the FFT (Fast Fourier transform) of the mode-converted LW signals truncated by a series of time windows, the convergence of the temporal spectrums are demonstrated resulting in the resonance of the plate within the driving frequency range. The root mean squares (RMS) of the temporal spectrums indicate that the signal to noise ratio associated with damage is amplified as the time window size increases. In this regard, the mode-converted LW singles can be integrated to the EM impedance signals for damage detection of the plate.

The spectral element (SE) for the CPBS is formulated to compute the EM signals in the frequency domain. The Euler-Bernoulli beam theory and one-dimensional linear piezoelectricity are used to model the electro-mechanical behavior of the PZT wafer. The effects of rotational mass inertia and shear deformation in the base beam are represented by the Mindlin-Herrmann theory and the Timoshenko beam theory, respectively. The validity of the proposed SE analysis is demonstrated through the comparison to the numerical results from FE analysis and experimental results.

Finally, the effects of the size and the location of damage on the mode-converted EM signals are investigated through parameter study using SE analysis. Through the parameter study, the feasibility of the reference-free damage diagnosis using EM signal is presented in a plate mode-converted.

---

Key Words: Elasto-dynamic, Lamb wave (LW), Electro-mechanical (EM) impedance, Plate, Coupled PZT-beam system (CPBS), Integrated damage detection, Temporal spectrum, Spectral element (SE), Finite element (FE), Root mean square (RMS).

# Contents

<b>1. Introduction</b>	<b>1</b>
1.1 Overview and Motivation	1
1.2 Literature Review	4
1.2.1 Lamb Wave-based Techniques Using PZT in Active SHM	4
1.2.2 EM Impedance-based Techniques Using PZT in Active SHM	7
1.2.3 Numerical Analysis of Surface-bonded PZT	8
1.3 Objectives and Scopes	11
1.4 Contribution and Uniqueness	14
 <b>2. Temporal Spectrum Analysis of Mode-converted Lamb Waves for Detecting Damage in a Plate</b>	 <b>17</b>
2.1 Pulse-superposition of Lamb Wave Induced by PZT	20
2.2 Analysis of the Temporal Spectrum of Lamb Wave Signals in the Intact Case	24
2.3 Decompositon of Lamb Wave Mode Signals Using the Poling Directionality of Collocated PZT Wafers	30
2.4 Decomposition of Lamb Wave Mode Signals Converging to the Steady-State Dynamic Response	34
2.4.1 Temporal spectrum of Mode-converted Signal by the Harmonic Input on the PZT	35
2.4.2 Temporal Spectrum of Mode-converted Signal by the	

Tone Burst Input on the PZT .....	40
2.4.3 Summary .....	47
<b>3. Spectral Element Formulation for EM Interaction between PZT</b>	
<b>and Structure .....</b>	<b>48</b>
3.1 Equation of Motion .....	48
3.1.1 Kinematic and Constitutive Assumptions of a CPBS .....	50
3.1.2 Deriving the Equations of Motion of a CPBS through	
the Hamilton's Principle .....	53
3.2 Spectral Element Formulation .....	61
3.2.1 Spectral Representation of Response Variables .....	62
3.2.2 Characteristic Equations and a Shape Function Matrix	
for a Spectral Element .....	63
3.2.3 Dynamic Stiffness Matrix and Admittance .....	65
3.3 Damage Spectral Element .....	67
3.4 Experimental and Numerical Analysis Studies .....	69
3.4.1 Case I: Admittance Comparison of Single PZT Model .....	70
3.4.2 Case II: Comparison of Mode Shape and Displacement	
FRF of Intact Model with Single PZT .....	75
3.4.3 Case III: Electro-Mechanical Signal Comparison of	
Intact Model with Collocated PZT .....	84
3.4.4 Case IV: Electro-Mechanical Signal Comparison of	
Notch Model with Collocated PZT .....	86
3.4.5 Case V: Comparison of proposed SE and Lee's	
Analysis .....	92
<b>4. Parameter Study for Reference-free Damage Detection .....</b>	<b>95</b>



4.1 The Varying Location and the Severity of Damage .....	95
4.2 The Effects of the Model Surface Strain Shape (MSSS) on the Amplitude of $EMS_{MC}$ .....	103
4.3 Imperfection Problem of the PZT Wafer .....	106
<b>5. Concluding Remarks</b> .....	109
5.1 Executive Summary .....	109
5.2 Further Study .....	112
<b>Appendix Remarks</b> .....	114
<b>Reference</b> .....	121
<b>Summary (In Korean)</b> .....	137

## List of Figures

Fig. 2.1 Two types of sensing schemes for damage detection using PTZs .....	20
Fig. 2.2 Wave propagation modes of initial Lamb wave .....	21
Fig. 2.3 Principle of wave pulses through signal superposition when harmonic input excited .....	23
Fig. 2.4 Propagation characteristic of tone burst input signal through the pulse wave superposition .....	24
Fig. 2.5 Temporal Spectrum analysis of LW signals truncated by different time windows when the harmonic input is imposed .....	25
Fig. 2.6 Convergence of transient LW signals to resonant standing wave signals with a harmonic excitation .....	27
Fig. 2.7 Temporal spectrum when the tone burst type input excited on the PZT .....	29
Fig. 2.8 Comparison of relative arrival time and phase information of decomposed Lamb waves .....	32
Fig. 2.9 Decomposition of the LW mode signals measured from the intact and damaged conditions when harmonic inputs are applied .....	37
Fig. 2.10 Temporal spectrums of $LWS_{MC}$ truncated by different time windows and RMS values when harmonic input signal is imposed .....	39
Fig. 2.11 Calculation of the RMS from a continuous function .....	40
Fig. 2.12 Decomposition of the LW mode signals when tone burst input with 10 kHz center frequency are applied .....	41
Fig. 2.13 Temporal spectrums of $LWS_{MC}$ when 10kHz tone burst input signal is imposed .....	42
Fig. 2.14 RMS values when tone burst input signal is imposed on the top PZT of a cantilever beam .....	43
Fig. 2.15 Determination of time window size through the comparing mode in the modal and temporal spectrum analysis .....	44
Fig. 2.16 Temporal spectrums of $LWS_{MC}$ truncated by different time windows when 100kHz tone burst input signal is imposed .....	45
Fig. 2.17 RMS values when 100kHz tone burst input signal is imposed .....	46

Fig. 3.1 Schematic illustration of a coupled PZT and beam system (CPBS) .....	50
Fig. 3.2 Procedures for spectral element formulation .....	61
Fig. 3.3 Schematic model of the transverse crack configuration .....	68
Fig. 3.4 Experimental and numerical models for the EM admittance of a PZT wafer bonded on a cantilever beam .....	71
Fig. 3.5 Comparison of resonance frequencies between proposed method and FEM .....	72
Fig. 3.6 Relative difference of resonance frequencies between SEM and 3-D FEM up to the 25 <sup>th</sup> mode .....	73
Fig. 3.7 Comparison of the electro-mechanical admittance from proposed method and experiment .....	73
Fig. 3.8 An experimental setup and a numerical model for FRF .....	74
Fig. 3.9 Perspective view of mode shapes from 3-D FEM (left side) and PSV (right side) .....	77
Fig. 3.10 Relative difference of the resonance frequencies between numerical analyses [SE, 2D-FE] and the test [PSV] up to the 11 <sup>th</sup> bending-dominant mode .....	78
Fig. 3.11 Quantitative comparison of resonant mode shapes from SE and PSV .....	80
Fig. 3.12 Comparison of frequency response functions corresponding to vertical displacement from SE and PSV at three points depicted as I, II, and III in Fig. 3.9 .....	82
Fig. 3.13 Comparison of mode ratio and frequency response functions ratio from SE and PSV at points I, II and III in Fig. 3.7 .....	83
Fig. 3.14 Comparison of admittance corresponding to the location of sensing PZT from proposed method (SE) and 2-D FE .....	84
Fig. 3.15 Relative differences between the resonance frequencies computed from the proposed method and 2-D FEM up to the 15 <sup>th</sup> mode .....	85
Fig. 3.16 Relative difference between the cantilever beam with a single and collocated PZT wafers at each resonance mode .....	85
Fig. 3.17 A damaged cantilever beam with collocated PZT wafers for measuring EM signals .....	86
Fig. 3.18 Comparison of the EMS and the resonance frequencies computed from the SE and FE analyses of the damaged cantilever beam in Fig. 3.17 .....	88

Fig. 3.19 Comparisons of the resonance frequencies obtained by SE and FE analyses of the intact and damaged conditions of the cantilever beam .....	89
Fig. 3.20 The EM signals obtained from collocated PZT wafers on the intact and the damaged cantilever beams in Fig 2.7 .....	90
Fig. 3.21 Decomposed EM signals through the application of Eq. (2.8) to EM signals from intact and damaged conditions in Fig 3.20 .....	91
Fig. 3.22 A beam partially covered with a rigidly bonded PZT layer ·	92
Fig. 3.23 Comparison of the FRFs and the Relative difference of the resonance frequencies from the proposed method, Lee' s method and 2-D FEM .....	93
Fig. 4.1 Parameter study model for simulating different damage scenarios .....	95
Fig. 4.2 Comparison of decomposed EMS signals corresponding to damage case at the 80mm notch location from the fixed end ·	97
Fig. 4.3 Comparison of decomposed EMS signals corresponding to damage case at the 100mm notch location from the fixed end .....	98
Fig. 4.4 Comparison of decomposed EMS signals corresponding to damage case at the 150mm notch location from the fixed end .....	99
Fig. 4.5 Comparison of extracted $EMS_{MC}$ signals and the peak values when the notch occurs at the 80, 100 and 150mm notch location from the fixed end .....	100
Fig. 4.6 $EMS_{MC}$ and their RMS amplitudes corresponding to a notch with varying depth and location in Fig. 4.1 .....	103
Fig. 4.7 The effects of MSSS at the PZT and notch locations on the amplitude of $EMS_{MC}$ .....	105
Fig. 4.8 Parameter study model for simulating PZT imperfection .....	106
Fig. 4.9 The variation of total RMS values according to the PZT bonding state when the 100kHz tone burst input excited and window size increse imperfection .....	107

## List of Table

Table 2.1 Damage detection techniques for SHM using PZT .....	106
---	-----

# Chapter 1

## Introduction

### 1.1 Overview and Motivation

Advances in sensor and IT technologies enable structural health monitoring (SHM) systems to assess damage using near real-time dynamic responses measured from structures. A large volume of research has been conducted to detect incipient damage such as crack and delamination in metallic and composite structures using electro-mechanical (EM) interaction between a piezoelectric transducer and a structure [Giu02, Par03, Rag07]. Wafer-type piezoelectric transducers made of lead zirconate titanate (PZT) can easily be bonded onto the surface of a structure to create and measure high-frequency dynamic responses sensitive to incipient damage. Due to the small, lightweight and nonintrusive nature of PZT, it has become popular for online SHM and nondestructive testing (NDT) applications [Cha95, Cha01, Wan99, Bol99, Kes02, Giu03]. When PZT is adopted for damage detection in a plate-like structure, two representative approaches are usually utilized: (1) wave propagation using Lamb wave (LW) signals in plates (e.g., either pitch-catch or pulse-echo) and (2) EM signals, such as impedance or admittance [Giu05, Par00, Bha04, Bul09].

In LW-based damage detection techniques using PZT, LW signals can exist in thin plates with parallel free boundaries and travel through

the entire thickness of a material. LW signals are especially important because they are elastic perturbations that can travel a long distance in thin-wall structures with only minimal energy loss [Kei95, Mou97, Giu00, Soh07]. Thus, LW signals enable the SHM of large areas from a single location. LW signals can also travel inside curved walls and composite plates [Lin01, Liu03]. These properties make them well suited for detecting surface defects of aircraft, pipelines, and others [Sun00, Giu01, Dal01, Tho02, Kes05]. However, NDT techniques using LW signals have major limitations because LW testing is generally complicated by the coexistence of dispersive and refractive modes at any given frequency [All92a, All92b, Wil01].

PZT wafers can be used as high-frequency modal sensors in the EM impedance-based method. The EM impedance-based method couples the mechanical impedance of the structural substrate with the electrical impedance measured at PZT wafer terminals. The EM impedance measured in high-frequency is sensitive to local incipient damage [Lia94], and has shown promise in detecting local defects in complex structures [Sun95a, Sun95b, Giu00a, Giu00b, Zag02].

From the above mentioned advantages, impedance-based damage detections have been conducted in various field applications. The basic scheme of EM impedance-based method for damage detection is to compare the response signals between intact and damaged statuses. However, it has been also reported that the base line signal of intact state is greatly affected by those operational and environmental variations. Furthermore, analytic model for EM interaction between

PZT and a host structure has been generally applied as a simplified Liang' s model of PZT actuator-driven system. The dynamic behavior of the host structure, whereby the substructure with bonded PZT is modeled by an one-dimensional equivalent spring, damping and mass, cannot be exactly represented. Therefore, the specific location and degree of damage are difficult to be identified in SHM, which relies on the characteristics of the host structure and damage.

The aforementioned problems are the motivations of this study. In order to overcome the limitations of conventional NDT method, a full understanding of the elasto-dynamic relations between the transient response of LW signals and steady state response, such as EM signals, is required. Also, reference-free technique based on the impedance signature is developed for reliable damage detection.

## 1.2 Literature Review

SHM can be performed either passively or actively. Passive SHM uses passive sensors that “listen,” but do not interact with the structure [Ree92, Kud93, Van95, Ell97, Kol98, Sch98, Hau99, Cha99].

Surface-bonded PZT wafers, which can capture guided wave, such as LW and EM signals, have great potential in active SHM. PZT wafer was initially used by Craweley et al. for structural vibration control [Cra87, Cra90]. PZT wafers are inexpensive, nonintrusive, unobtrusive, and minimally invasive devices that can be surface-mounted on existing structures, between the layers of lap joints, or inside composite materials. The use of PZT wafer in active SHM has been experimentally explored for civil, mechanical, and aerospace structures [Cha95, Kei95, Giu00, Lin01a, Lin01b, Ihn02, Kes04, Zha07, Soh10, Par10].

### 1.2.1 Lamb Wave-based Techniques Using PZT in Active SHM

Acousto-ultrasonic techniques are based on stress waves introduced into a host structure. Various mechanisms of wave propagation are utilized for damage detection. Ultrasonic inspection, such as NDE, is well established and has been used in the engineering community for several decades [Kra90, Sta03, Ost09].

In an infinite solid medium, elastic waves can propagate in two basic modes: pressure (P) and shear (S) waves. However, if the medium is bounded, wave reflections occur at the boundary, and more complicated



wave patterns emerge. Guided waves propagate along the midsurface of thin-wall plates and shallow shells. They can travel a relatively long distance with very little attenuation, offering the advantage of large-area coverage with a minimum of installed sensors. One guided wave is Rayleigh wave, which propagates close to the free surface of elastic solids [Ray87]. Other examples are Stoneley, Love, and Scholte waves, which travel at material interfaces [Sto24, Lov26, Lov 44, Sch42]. Also, Gazis developed and analyzed the dispersion equations for guided waves in cylinders [Gaz58, Gaz59].

A very important class among these guided waves is Lamb wave (LW), which can propagate in solid plates (or shells) with free surfaces. Due to the abundance of plate- and shell-like structural configurations, this class of guided waves has been the subject of much scrutiny. LW signals were first mathematically predicted and described by Horace Lamb [Lam17] a century ago. However, he was not able to experimentally produce guided waves. This was achieved by Worlton [Wor61], who was likely the first to recognize the potential of guided waves for NDE. LW theory is fully documented in a number of textbooks [Vik67, Gra75, Ach99, Ros99]. Guided LW signals have opened new opportunities for cost-effective detection of damage; a large number of papers have been published on this subject [Dal01, Tho02]. Traditionally, guided waves are obliquely generated by impinging the plate with a tone burst from a relatively large ultrasonic transducer [All92].

In recent years, several investigators have explored the generation

of Lamb-waves with PZT-wafer active sensors [Kei95, Giu00, Giu02, Soh07, Par10]. PZT wafers can be used as transmitters and/or receivers of LW signals in the specimen, by using pitch-catch and pulse-echo methods. In the former, a pulse signal is sent across the specimen under interrogation, and a sensor at the other end of the specimen receives the signal [Caw96, Wai04, Pra04, Tua05, Par06, Cuc07, Ihn08]. In the pulse-echo method, after exciting the structure with a narrow bandwidth pulse, a sensor collocated with an actuator is used to “listen” for echoes of the pulse coming from discontinuities [Ros94, All01, Giu04]. The LW-based approaches using the pitch-catch and pulse-echo method have been utilized by identifying the changes in the transmission velocity and energy of the elastic waves associated with damages.

The reference-free approach has been proposed as an alternative for more effective damage detection using PZT wafer. This approach utilizes the time reversal process [Par07, Soh07] and LW propagation on a plate using polarization of collocated PZT wafers [Kim07]. The reference-free technique has been advanced from the time domain into the frequency domain. The improved reference-free technique is based on the premise that crack-induced Lamb mode in time domain is converted through fast Fourier transform (FFT) into the frequency domain, thereby estimating the energy of the converted Lamb mode [Par10]. These techniques do not rely on previously obtained baseline data for crack detection and extraction of the damage sensitive features. Therefore, the reference-free technique is robust to

operational and environmental changes, such as varying temperatures.

### 1.2.2 EM Impedance-based Techniques Using PZT in Active SHM

EM signals, such as impedance and admittance, are affected by the theoretical development of applying impedance measurements to SHM. This was first proposed by Liang et al. [Lia94]. A brief introduction of the concept of the impedance method is presented below.

EM impedance-based analysis of the dynamic response of active material systems based on the interaction between actuators and structures being governed by the EM characteristics of the actuator and the dynamic characteristics of the structure, (i.e., the structural impedance). The structural impedance includes mass, damping, boundary condition, rigidity, spatial location, and acoustic impedance if fluid coupling effect needs to be included.

Liang et al. proposed two approaches currently used in the dynamic analysis of active material systems; static approach and dynamic finite element approach. In static approach, the pin-force model is widely used [Cra89]. In pin-force model, the mechanical interaction between a bonded actuator and its host structure is assumed to occur at the ends of the actuator in the form of concentrated forces. These concentrated forces, which represent the effects of the induced strain actuator in static and dynamic analyses, are determined based on strain compatibility and static force equilibrium between the actuator and structure. Crawley et al. used this approach for determining the static

equivalent force or moment uses of Euler–Bernoulli beam equations. Additionally, Giurgiutiu et al. developed a new model based on the pin–force theory [Giu05].

In dynamic approach, the EM modeling of PZT actuator–driven systems is based on the impedance method developed by Liang et al. This is a one–degree–of–freedom mode for dynamic approach, consisting of spring, mass and damper system driven by a PZT actuator. The dynamic interaction between the PZT and the structure is determined by coupling one of the constitutive relations of PZT and the structure with equilibrium, compatibility conditions, and the equations of motion for both the PZT actuator and the structure.

This is a simplified model; however, the variation of EM signal according to dynamic specific of host structure cannot be accurately interpreted. Wang et al. extended the work of Liang et al. to PZT stack actuators with structures at both sides, and checked their sensing and actuation ability in detail [Wan96a, Lia93a]. Subsequently, this model has been developed by other researchers. [Giu88a, Giu88b, Cha95, Ayr98, Giu00, Giu03, Zag01, Bha02a, Par03, Par05]. In these studies, the PZT patches required very low–level voltage, typically less than 1 V, to produce high–frequency excitation in the host structure.

### 1.2.3 Numerical Analysis of Surface–bonded PZT.

In terms of modeling the effect of surface–bonded PZT wafer, researchers hold different opinions. A few works have suggested that surface–bonded PZT wafers act similarly to conventional ultrasonic

transducers. Conventional ultrasonic transducers act through surface “tapping,” which means applying vibrational pressure to the object’s surface, thereby causing uniform normal traction over their contact area. In contrast, majority of the previous works (including ours) have suggested that PZT wafers are more effectively modeled through “pinching,” which means applying strain coupled with the object surface. This idea was inspired by the work of Crawley et al., who proposed this model for quasi-static induced strain actuation of PZT wafer bonded on a beam [Cra87, Cra91].

In previous works, finite element method (FEM) have been adopted to compute coupled dynamic responses between a PZT wafer and a plate-like structure [Alf74, Par06]. However, each element in FEM should be sufficiently small to guarantee accuracy of the solution. FEM requires a large number of elements and, consequently, huge computational cost for simulating the coupled dynamic responses in a high-frequency range.

Spectral element method (SEM) is one of the alternatives to FEM for computing the coupled dynamic responses because the inertia effect of the structure can be properly represented without dense mesh refinement. Narayanan et al. were the first to introduce the basic concept of SEM [Nar78]. They derived the exact dynamic stiffness matrix of the beam element and employed FFT techniques for dynamic analysis of plane frames. Their work was further improved and generalized by Spyrakos et al. [Spy82]. Later, Doyle applied SEM to wave propagation in structures [Doy88]. The SEM applications to

wave propagation problems by Doyle et al. the related references up to year of 1997 are found in the book by Doyle [Doy97]. Furthermore, various spectral elements have been introduced to analyze the dynamic responses of rods, beams, and plates [Gop94, Lee00, Doy00]. In impedance analysis, application of SEM to various structural dynamic problems was conducted by Lee et al. This study is one of the few works dealing with the development of a spectral element that can simulate the coupled dynamic responses between a base beam and a surface bonded PZT wafer. Lee et al. developed spectral elements for modeling the dynamic interaction of a base beam and a surface-bonded PZT wafer [Lee01]. They formulated two sets of motion equations: (1) a two-layer beam model consisting of a base beam and a PZT layer and (2) a three-layer beam model consisting of a base beam, an adhesive layer and a PZT layer. In their formulation, the longitudinal and flexural behaviors of both the base beam and the PZT layer are assumed to follow the elementary rod and Euler-Bernoulli beam theories, respectively. Although these assumptions generally work well in a low-frequency range, lateral contraction, rotational mass inertia and shear deformation, which play significant roles in high-frequency response, cannot be properly represented in the elementary rod and Euler-Bernoulli beam theories.

### 1.3 Objectives and Scopes

The objective of this research is to study an EM signal-based reference-free damage detection technique, regardless of environmental and operational variations. Damage detection base on the EM signal has been a limitation due to the variation of the base signal and a lack of the understanding the EM signal. Additionally, the Liang's model is a simplified one-dimensional model, which is difficult to exactly calculate the EM signal considering to the modal behavior of a host structure. Therefore, the correlation analysis between LW and EM signals, which are currently being independently used, is examined to exactly understand the EM signal, and then the signal decomposition technique of the EM signals is derived. Also, full modeling techniques that simulate dynamic behavior of host structure and PZT wafer are proposed. The specific objective and scope of this research are represented as follow;

In Chapter 2, elasto-dynamic analysis of transient LW mode signal on the plate-like structure is introduced. The correlations between LW and EM signals are investigated through the wave pulse and temporal spectrums of LW signals when input voltage signals are excited by two types of excitation (i.e., harmonic and tone burst) on the PZT. Here, finite element (FE) analysis is adopted to calculate an approximate solution. Also, the mode-converted LW signal is computed by the LW decomposition technique, and then the temporal spectrums are investigated according to different time window size to truncate the

mode-converted LW signal. Through the temporal spectrums and RMS (root mean square) values of temporal spectrum, understanding the signal characteristics of EM signals and the possibility of the reference-free damage detection using the mode-converted signal will be shown by the EM signal decomposition technique.

In chapter 3, the full modeling theory of using proposed spectral element (SE) is explained to interpret EM interaction between a host structure and PZT wafers; the equation of motion is formulated prior to a spectral element for a coupled PZT and beam system (CPBS) that can properly take into account of lateral contraction, rotational mass inertia and shear deformation in the high frequency range. In the analysis of intact condition using CPBS model, the longitudinal and flexural behaviors of the base beam are represented by the Mindlin-Herrmann theory and the Timoshenko beam theory, respectively [Min51, Tim22, Doy97]. Because the thickness of the PZT wafer is relatively small compared to that of the base beam, the longitudinal and flexural behaviors of the PZT wafer are represented by the elementary rod theory and the Euler-Bernoulli beam theory, respectively. In the case of damage analysis, additional damage spectral element is proposed to describe the damaged base beam and the mode-converted signal which is steady-state signal as the EM signal is extracted by the signal-decomposition technique based on the EM signals. The FE analysis and experimental test through impedance analyzer and laser scanning vibrometer are performed for validation of proposed SE analysis.



In chapter 4, the parameter studies are conducted to verify the possibility of the integrated damage detection. Numerical simulation is performed through the proposed spectral element (SE) analysis using a coupled PZT-beam system (CPBS). The RMS value is used for damage quantification. First, the decomposed mode-converted signal corresponding to the varying notch location and depth is calculated and the RMS of each mode-converted signal is compared to define the damage. Then, the correlation between the model surface strain shape (MSSS) and the peak-size of the decomposed EM signals due to damage is analyzed to know additional characteristic of EM signal. Finally, imperfection effect is considered to confirm the limitation of the proposed method. Here, the imperfection represents the anti-symmetric condition of the collocated PZT wafer on the top and bottom surface in the plate-like structure. When the input voltage and imperfection condition are changed, the relative criterion for damage detection will be properly predicted in the frequency domain.

## 1.4 Contribution and Uniqueness

This study proposes a great potential to EM signal-based damage diagnosis. As removing the unexpected changes in environmental effects and operational variations, existing EM signal-based techniques will have attractions to real-structure applications since this technique is very sensitive to local damage. The uniqueness of this study is listed below.

1. Qualitative and quantitative analysis of the Electro-mechanical signal with respect to the mode characteristics by the elasto-dynamic behavior of the Lamb:

Through the finite element (FE) analysis, the modal harmonic motion of Lamb wave by the time history analysis and the natural mode shape by the modal analysis are qualitatively analyzed as the same. Therefore, it is shown that Lamb wave signal in the time domain and EM signal in the frequency domain are not individual signals. If the frequency of Lamb wave pulse signal is the same as the resonance frequency of the structure, the magnitude of temporal spectrum to be depended on the linear superposition of pulse is theoretically shown. As the time window size increases, the magnitude variation of temporal spectrum has the correlation of converging Lamb wave in the time domain into EM signal in the frequency domain.

The EM signal which is considered to the modal characteristics of a

host structure is quantitative verified with respect to the elasto-dynamic behavior of Lamb wave through pulse-superposition and temporal spectrum.

2. Theoretical verification of reference-free damage diagnosis using EM signal:

The temporal spectrum is used to investigate a mode-converted Lamb wave signal which is extrated by a polarization direction of collocated PZT on the both side of a plate. In particular, the correlation analysis associated with the electro-mechanical signal is conducted through a comparison of spectrum signals in the frequency domain, and then EM signal-based reference-free damage diagnosis technique is first proposed. Through the FFT (fast Fourier transform) of the mode-converted LW signals truncated by a series of time windows, the temporal spectrums and RMS values of the temporal spectrum are equally incresed as the time window size increases. In this regard, theretical basis and validation shows that the damage detection using the electro-mechanical signal is more efficient than the one using Lamb wave in the reference-free technique because the signal to noise ratio associated with damage is amplified.

3. Formulation of spectrum element and parameter study using spectral element analysis for refrence-free damage detection:

The spectral element (SE) for the CPBS is formulated to compute the

EM signals in the frequency domain. The SE analysis using the CPBS is a good alternative to FE analysis because the mass inertia effect of a host structure can be exactly considered without dense mesh refinement in the high-frequency range. The thickness of the PZT is assumed relatively small compared to that of the base beam, and it is assumed that PZT and base beam are perfectly bonded. The Euler–Bernoulli beam theory and one-dimension linear piezoelectricity are used to model the electro-mechanical behavior of the PZT wafer. The effects of rotational mass inertia and shear deformation in the base beam are represented by the Mindlin–Herrmann theory and the Timoshenko beam theory, respectively. The validity of the proposed SE analysis is demonstrated through the comparison to the numerical results from FE analysis and experimental results.

Finally, the effects of the size and the location of damage on the mode-converted EM signals are investigated through parameter study using SE analysis. Through the parameter study, the feasibility of the integrated damage detection of a plate is presented.

## Chapter 2

### Temporal Spectrum Analysis of Mode-converted Lamb Waves for Detecting Damage in a Plate

In Lamb wave (LW)– and electro–mechanical (EM) impedance–based SHM using the PZT which are either permanently attached to the structure or inserted between the layers of composite lay–up, the input voltage signals of actuator generating LW and EM signals are excited by some high–frequency pulse signal (typically a modulated sinusoidal harmonic, chirp or tone burst of the narrow band frequency range). Especially, LW modes (such as the S0 and A0 Lamb wave) and EM impedance that are strongly influenced by small changes in the material stiffness and thickness are well suited for damage detection of the structure.

In general procedure of NDT using LW signals and EM signals, such as impedance and admittance, the LW signals are scattered as the different modes by the reflection and propagation when the LW signals pass through a structural discontinuity. The EM signals are also changed according to a discontinuity. The structural discontinuity could be divided into several types, such as a crack, delamination, a structural feature (such as a stiffener) or a structural boundary. Therefore, prior information is required about the structure in its undamaged state to be able to distinguish between damages and structural features. Although there are some differences to compare variables, such as the case of LW signals examine a phase, dispersion,

and time of flight; or EM signals are a frequency value and amplitude of resonance frequency, etc. These signals comparing, “current” measured signal with “pristine” measured signal, are equally applied to LW and EM signals for damage detection. The traditional damage detection techniques using LW and EM signals can be summarized as shown in Tab. 2.1 according to the types of dynamic response signals and sensing schemes.

Table 2.1 Damage detection techniques for SHM using PZT.

Sensing Signal type	Self sensing	Remote sensing
Transient Signal ( $T \ll 1$ )	Pulse echo method	Pitch-catch method
Steady-state Signal ( $T \gg 1$ )	EM impedance-based method	Transfer impedance-based method

First, signal type can be divided into transient signal and steady-state dynamic response signals, respectively. When a host structure is excited, the transient signal represents the generated and measured ones in relatively short period of time. On the contrary steady-state signals indicate those measured during a relatively long time. Next, there are also two approaches depending on the sensing layout to detect damage. Self-sensing and remote-sensing utilize the single or dual PZTs, respectively for generating and sensing the response signals. The schematic of the self-sensing and remote-sensing are shown in Fig. 2.1 [Sho07, Kim07, Par10, Sho10]. The Fig. 2.1(a) represents the remote-sensing consists of the pitch-catch and transfer

impedance method which are classified as the applying signal depending on time. Two or more PZTs are generally used for remote sensing to analyze the transient state and steady-state signals. An input pulse signal is exerted on one PZT and LW signals travel across the specimen under interrogation. Then another PZT at the opposite side of the specimen receives the response signals which are LW or impedance signals. From this way, the remote method can be used to detect the presence of cracks. When LW signals encounter a crack, the incident waves get scattered. The scattered signals can be extracted through the comparison of the pristine and damaged wave signals. Analysis of the scattered signal allows for extracting the wave modes created by damage evolution. [Lin01(a), Liu03, Giu03(a), Ihn03]. The boundaries of a structure do not affect this method. On the other hand, the self sensing method is presented in Fig. 2.1(b) [Par10, Kim10(a), Kim10(b)]. The same PZT is used to “listen” for echoes of the pulse coming from discontinuities after a bonding PZT on the structure is excited with input voltage signal. Because the boundaries and the wave speed for a given center actuation frequency of narrow band pulse such as tone burst are known, the signals from the boundaries can be filtered out (or alternatively the test signal can be subtracted from the baseline signal). Then, signals from the defects are left. Depending on the type of applying signal can be separated as pulse-echo and EM impedance method.

Until recently, the above mentioned methods have been used independently in the SHM of utilizing PZT. The efforts are under way

to improve or to integrate above methods for the more efficient damage detection in the SHM of utilizing PZT.

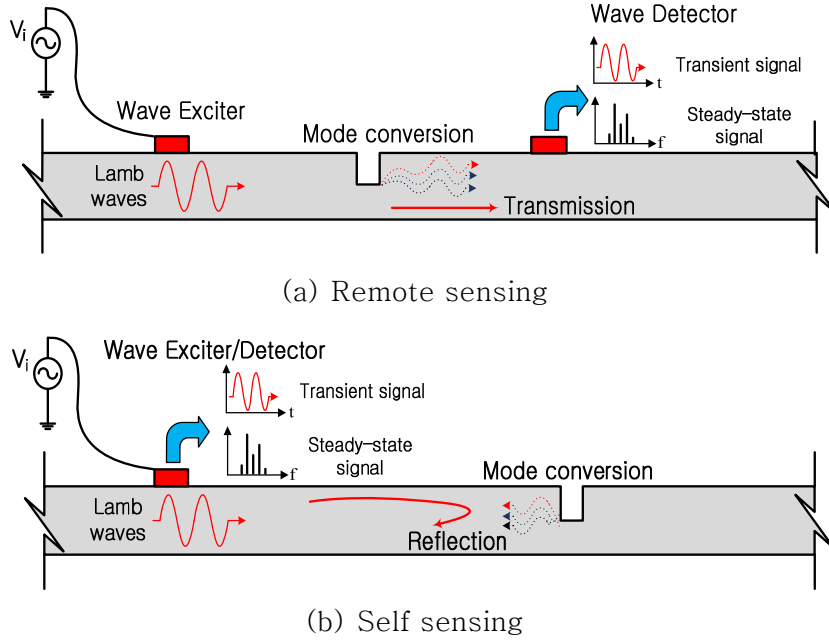
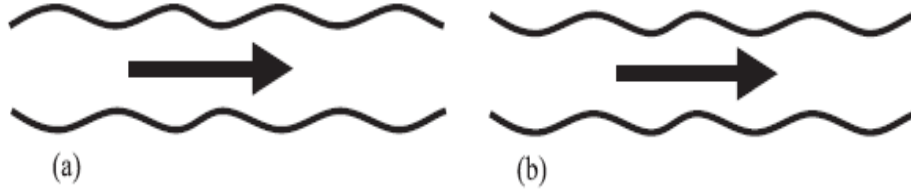


Figure 2.1 Two types of sensing schemes for damage detection using PZTs.

## 2.1 Pulse–superposition of Lamb Wave Induced by PZT.

Plate waves can be propagated only in very thin metals. LW signals are the most commonly used plate waves in NDT. LW signals are complex vibrational waves that travel through the entire thickness of a material. Propagation of LW signals depends on the density and the elastic material properties of a component. They are also influenced a great deal by the test frequency and material thickness.





(a) Symmetric mode (extension) (b) anti-symmetric mode (bending)

Fig 2.2 Wave propagation modes of initial Lamb wave (LW).

Using PZT wafers placed on a host structure, LW signals consist of symmetric ( $S_0, S_1, \dots$ ) and anti-symmetric modes ( $A_0, A_1, \dots$ ) are generated. As shown in Fig. 2.2, a symmetric and an anti-symmetric mode wave behave like an extensional and a bending wave, respectively.

Also, the characteristics of wave pulses according to the applying input signal types on the PZT are defined by the following equations based upon the simple harmonic motion. The transmission wave pulses ( $y$ ) and reflection wave pulses ( $y'$ ) described by Eq.(2.1a) and Eq.(2.1b), respectively.

$$y = a_n \cdot \cos(\omega_n \cdot t + \varphi_n) \quad (2.1a)$$

$$y' = a_n \cdot \cos(\omega_n \cdot t + \varphi'_n) \quad (2.1b)$$

Where,  $a_n$ ,  $\omega_n$  and  $\varphi_n$  represent amplitude, angular frequency and initial phase angel of the motion.

The superfosition of two wave pulses is defined as follows:

$$\bar{y} = y + y' = \bar{a}_n \cdot \cos(\omega_n \cdot t + \bar{\varphi}_n) \quad (2.2)$$

Where,  $\bar{a}_n = 2a_n \cdot \cos\{(\varphi_n - \varphi'_n)/2\}$  and  $\bar{\varphi}_n = (\varphi_n + \varphi'_n)/2$ .

Note that, the superpositions of wave pulses in Eq. (2.2) are generated as various wave pulses according to the phase angle ( $\bar{\varphi}_n$ ). Two kinds of representative wave pulses are defined as follows:

– Resonance state ( $\bar{\varphi}_n = \varphi_n = \varphi'_n$ )

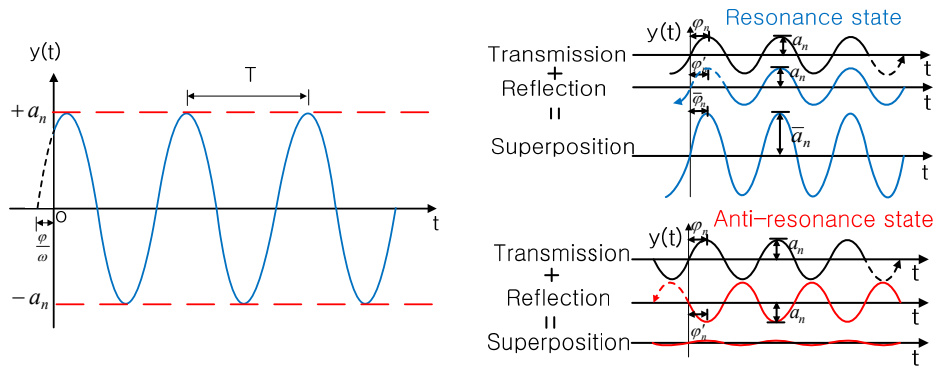
$$\begin{aligned}\bar{y} &= 2a_n \cdot \cos(\omega_n \cdot t + \varphi_n) = 2a_n \cdot \cos(\omega_n \cdot t + \varphi'_n) \\ \bar{a}_n &= 2a_n \cdot \cos\left(\frac{\varphi_n - \varphi'_n}{2}\right) = 2a_n\end{aligned}\tag{2.3}$$

– Anti-resonance state ( $\bar{\varphi}_n = (\varphi_n + \varphi'_n)/2$ ,  $\bar{\varphi}_n \Rightarrow \pi/2$ )

$$\begin{aligned}\bar{y} &= 2a_n \cdot \cos\left(\frac{\varphi_n - \varphi'_n}{2}\right) \cdot \left\{ \cos\left(\omega_n \cdot t + \frac{\varphi_n + \varphi'_n}{2}\right) \right\} \\ \bar{a}_n &= 2a_n \cdot \cos\left(\frac{\varphi_n - \varphi'_n}{2}\right) = 0\end{aligned}\tag{2.4}$$

If phase angle of the transmission wave pulse and reflection wave pulse are the same, the magnitude ( $\bar{a}_n$ ) of motion becomes  $2a_n$  and Eq. (2.3) is obtained to describe the resonance state. If phase angle of the transmission wave pulse and reflection wave pulse are different, it is the random case including Anti-resonance state when difference of two phase angle is  $\pi/2$  in the magnitude ( $\bar{a}_n$ ) of motion.

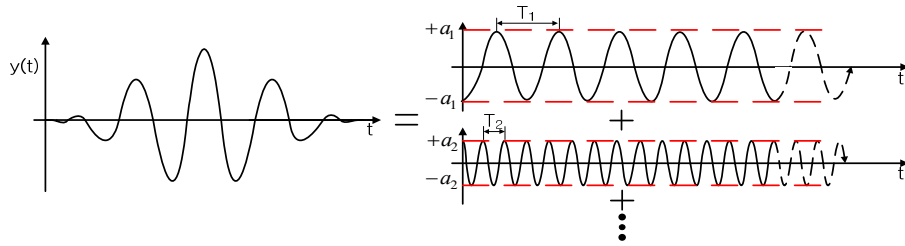
A motion of the type described by Eq. (2.3) and (2.4), simple harmonic motion, is represented by an magnitude of pulse(y)–time(t) graph such as that shown in Fig. 2.3.



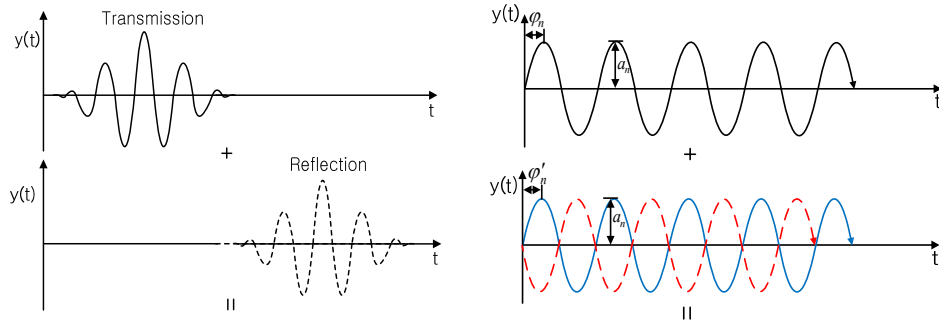
(a) Harmonic input of period ( $T$ ) and amplitude ( $a_n$ ) (b) Two kinds of representative wave pulse of harmonic motion.

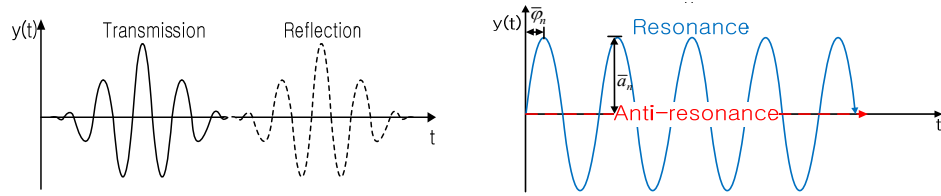
Fig 2.3 Principle of wave pulses through signal superposition when harmonic input excited.

In a similar fashion, wave pulse is generated as shown Fig 2.4 when the tone burst signal applies to the PZT wafer. Note that, tone burst signal consists of linear superposition of the simple harmonic motion.



(a) Linear superposition of tone burst input signal.





(b) Initial Propagation process of tone burst signal.

(c) Extracted  $n^{\text{th}}$  wave pulse to explain the superposition of tone burst signal.

Fig 2.4 Propagation characteristic of tone burst input signal through the pulse wave superposition.

## 2.2 Analysis of the Temporal Spectrum of Lamb Wave Signals in the Intact Case

As time passes by, you can observe a change of these LW signals from transient state to steady-state in Fig. 2.2. Both transient and steady-state dynamic responses of the structure can be easily generated and measured through the EM coupling between the PZT wafers and the structure. Fig. 2.5 schematically illustrates how the LW signals induced by PZT wafers converge to the steady-state dynamic responses of the beam. In Figs. 2.5(a), a cantilever beam with collocated PZT wafers is presented for the simplicity of explanation. As harmonic excitations of the 11<sup>th</sup> natural mode shape ( $f=15.4\text{kHz}$ ) are applied to the PZT wafers, LW signals begin to propagate from the actuating PZT wafers as shown in Fig. 2.5(b) [Ros99]. Then, incident LW and reflected signals from the boundaries of the beam are superimposed, producing transient dynamic states in Fig. 2.5(c).

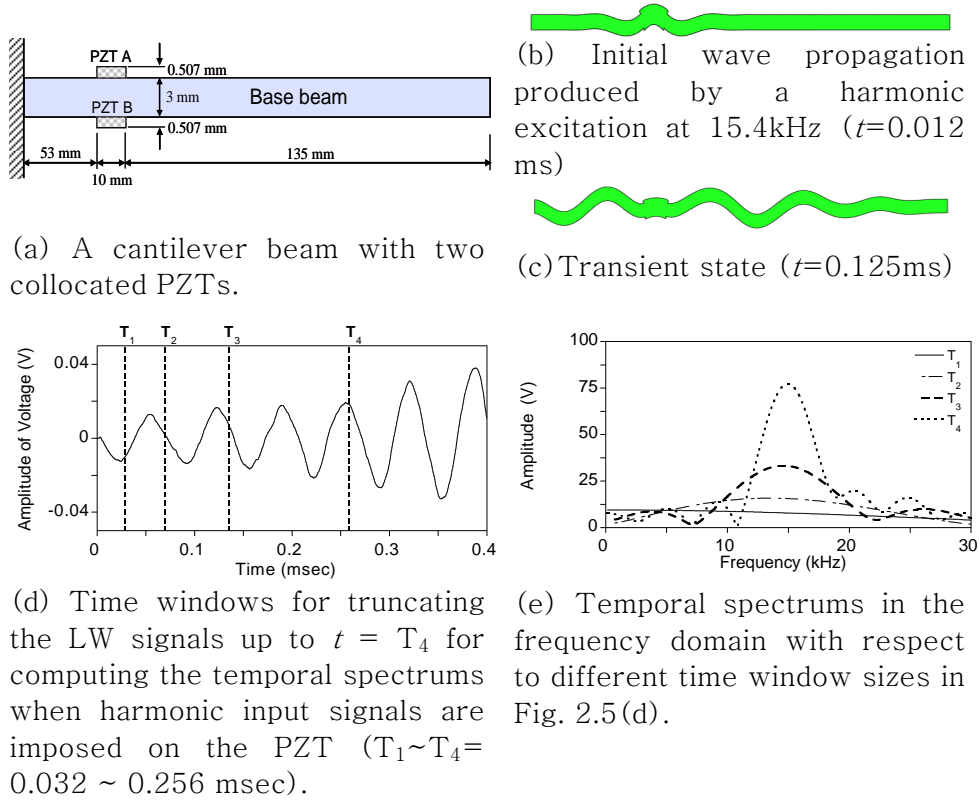
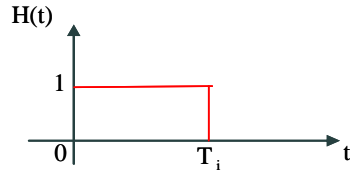


Fig. 2.5 Temporal Spectrum analysis of LW signals truncated by different time windows when the harmonic input is imposed.

For a more accurate understanding of correlation between transient and steady-state signal in the time domain, the effect of the time window size on the temporal spectrum has been investigated through numerical simulation in Figs 2.5(d), 2.5(e) and 2.6. The temporal spectrum described by Eq.(2.5).

$$X(\omega) = \int_{-\infty}^{\infty} y(t)H(t - T_i)e^{-i\omega t} dt \quad (2.5)$$



$y(t)$ : wave pulse function  $f$

$H(t - T_i)$ :  $t > T_i \Rightarrow 0$

$t \leq T_i \Rightarrow 1$

$H$ : heaviside function

Here, the Newmark- $\beta$  method in ABAQUS 6.7-4 is used to accurately solve LW propagation problem in the time domain [Kis10, Aba10]. The LW signals induced by the harmonic input are truncated through a series of time windows with increasing size. Since Fast Fourier transform (FFT) is used to compute the temporal spectrum, the time window size ( $T_n$ ) is determined by multiplying the sampling number ( $N$ ) and time interval ( $\Delta t$ ). In our study, the sampling number ( $N$ ) is set to be  $n$  power of 2 and the sampling interval  $\Delta t = 0.25\mu\text{sec}$ . The  $n^{\text{th}}$  time window size ( $T_n$ ) is defined as  $2^{(n+6)} \cdot \Delta t$ . Four temporal spectrums are compared in Fig. 2.5(e). As the time window size increases, the peaks of the temporal spectrums in Fig. 2.5(e) become dominant near the resonance frequency (11<sup>th</sup> mode,  $f = 15.4\text{ kHz}$ ).

At  $t = 5.0\text{ms}$ , the cantilever beam becomes resonant as shown in Fig. 2.6(a) and the vibrating shape is identical to the 11<sup>th</sup> natural mode shape in Fig. 2.6(b) [Fre71]. Also, the truncated LW signals induced by the harmonic input are calculated as shown Fig 2.6(c). When the temporal spectrums are compared to the temporal spectrums in Fig. 2.5(e), those in Fig 2.6(d) show a sharper peaks at the resonance frequency. Here, it is known that the peak size in the frequency domain is proportional to the response signal length in the time domain when the harmonic signal (11<sup>th</sup>,  $f = 15.4\text{kHz}$ ) is excited on the PZT. Note that,

the steady-state signal, such as impedance, could be obtained when sufficient time has been passed in the time domain analysis using the transient LW signals as shown the mode shape in Fig. 2.5. Compared to the temporal spectrums in Fig. 2.5(e), those in Fig. 2.6(d) show sharper peaks at the resonance frequency and converge to the frequency response function. Usually, LW-based damage detection schemes utilize a narrow-band tone burst signals considering the dispersion characteristics of a structure instead of harmonic input signal in Figs. 2.5 and 2.6.

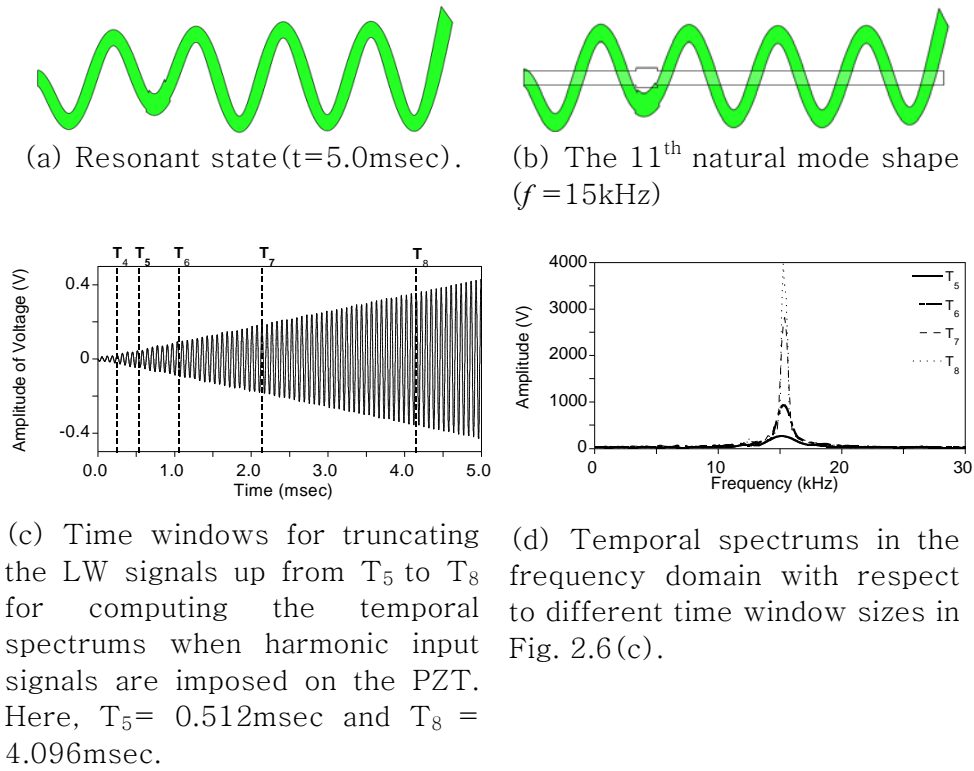
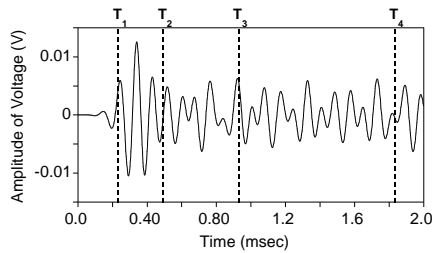
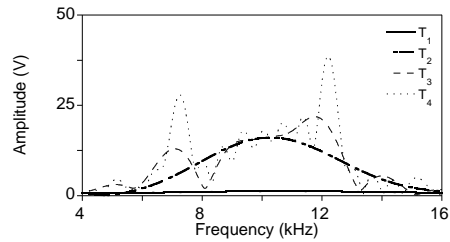


Fig. 2.6 Convergence of transient LW signals to resonant standing wave signals with a harmonic excitation.

The Fig. 2.7 presents the LW signals in the time domain [Figs. 2.7(a) and 2.7(c)] and the corresponding EM spectrum signal [Fig. 2.7(b) and 2.7(d)] in the frequency domain, respectively. Similar to Figs. 2.5 and 2.6, the LW signals up to 2.0msec are truncated by time windows with increasing sizes as shown Fig. 2.7(a) and the corresponding temporal spectrums are computed through fast Fourier transform in Fig. 2.7(b). Here, the time interval ( $\Delta t$ ) is 1.8  $\mu$ sec and the size of the  $n^{\text{th}}$  time window ( $T_n$ ) is set to be  $2^{(n+6)} \Delta t$ . In Fig. 2.7(b), several peaks begin to appear within the driving frequency band from 4kHz to 16kHz for relatively small time window sizes. As the time window size increases as shown Fig. 2.7(c), the several peaks in the temporal spectrums in Fig. 2.7(d) converge to the resonance frequencies of the cantilever beam within the driving frequency band. When the time window size is large enough (e.g.  $T_8=29.491\text{msec}$ ), the associated temporal spectrum converges to the frequency response function. At this stage, the temporal spectrum also can represent the well-known EM impedance or admittance.

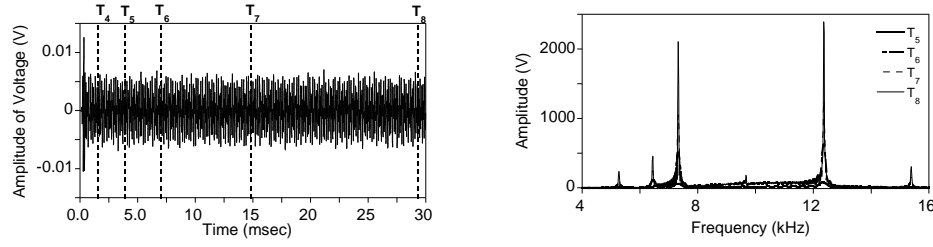


(a) The response signal to  $T_4$  when tone burst type input is excited on the PZT. ( $T_1 \sim T_4 = 0.230 \sim 1.843$  msec;  $N = 2^7 \sim 2^{10}$ ).



(b) The converted response signal into frequency domain according to the signal lengths ( $0 \sim T_n$ ,  $n = 1 \sim 4$ ) in fig. 2.7(a).





(c) The signal Division on the total response signal from  $T_4$  to  $T_8$  by the sampling points ( $N=2^n$ ,  $n=11\sim14$ ). Here,  $T_8=29.49\text{msec}$ ,  $N=2^{14}$ .

(d) Comparison of conversion signal according to response signal lengths ( $0\sim T_n$ ,  $n=5\sim8$ ) in fig. 2.7 (c).

Fig. 2.7 Temporal spectrum when the tone burst type input excited on the PZT.

Although the complex behavior between transient LW and steady-state LW signals is difficult to derive a numerical formula, the results from Fig 2.5 to Fig 2.7 are very important meaning to understand EM signals. The temporal spectrum is to convert the transient LW signals into steady-state signals through fast Fourier transform (FFT) according to input excitation, such as the harmonic and ton burst types. When the electric characteristic of the PZT and the mechanical characteristic of the host structure are coupled, the EM signal, such as impedance and admittance, can be obtained in the steady-state of frequency domain. Note that, if the damping of the host structure is zero, the time will be assumed infinite to make the resonance of the host structure.

Therefore, we can understand that the LW signals and EM signals are not a separate signal. Also, the additional analysis of the LW signals

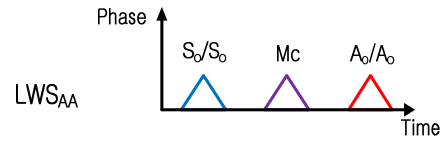
will be needed for more detailed relation between LW and EM signals. In the next subsection, the variations of the LW signals in the transient state are discussed by the influence of the damage, such as notch.

### 2.3 Decomposition of Lamb Wave Mode Signals Using the Poling Directionality of Collocated PZT Wafers

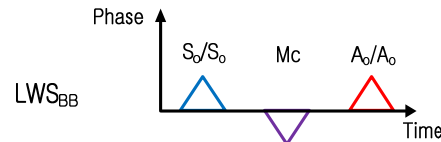
As described above, the conversion of transient LW signals into resonance standing LW signals is important principle to understand characteristics of the LW signals and is an important concept to understand the dynamics characteristics of the EM signals, at the same time. Therefore, a more accurate understanding of LW signals will get an accurate understanding of EM signals.

In the previous study [Kim07], PZT wafers were placed considering their polarization characteristics so that the mode conversion due to crack formation can be isolated. The formation of a crack in a plate induces a sudden thickness variation and becomes a source of mode conversion. If the LW signals propagating along a thin plate encounter a discontinuity point such as crack, then some portion of the transmitted LW modes will be converted into other modes. For example, when the first symmetric LW mode ( $S_0$ ) arrives at the discontinuity, the transmitted wave is separated into fundamental symmetric ( $S_0$ ) and anti-symmetric ( $A_0$ ) LW modes (denoted as  $S_0/S_0$  and  $A_0/S_0$ , respectively). In a similar fashion, an  $A_0$  mode is also transformed into  $S_0$  and  $A_0$  modes ( $S_0/A_0$  and  $A_0/A_0$ ).

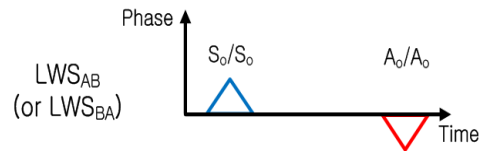
Fig. 2.8(a) shows two identical PZT wafers collocated on both sides of a plate and a source of mode conversion. Here, the source of mode conversion is assumed to be a notch. The arrows placed over and under PZT wafers denote the poling directionality of the PZT wafers [Kim07]. Each PZT wafer can be used to create and detect LW modes. Because both actuating and sensing PZT wafers are collocated on the plate, the generation and reception of LW modes take place in the pulse-echo mode [Rose07]. For the brevity of description, only  $S_0$  and  $A_0$  LW modes are considered, and  $S_0$  mode is assumed to travel faster than  $A_0$  mode. In Fig. 2.8(a), LW signals are excited and measured by PZT A while PZT B plays a role of simultaneous actuation and sensing in Fig. 2.8 (c). In Fig. 2.8 (e), LW signals are generated by one of PZTs A and B and measured by the other PZT. The first arrivals of the converted modes ( $S_0/A_0$  and  $A_0/S_0$ ) appear between the first arrivals of the  $S_0$  and  $A_0$  modes reflected from the notch. It should be noted that the arrival times and the waveforms of  $S_0/A_0$  and  $A_0/S_0$  are exactly same because the traveling distance for  $S_0$  mode and  $A_0$  mode are identical in the pulse-echo method. The only difference between  $A_0/S_0$  and  $S_0/A_0$  is their relative phases which depend on the polarization orientations of the actuating and sensing PZT wafers. Figs. 2.8(b), (d) and (f) schematically present the relative arrival times and phases of various LW mode signals created and received through the illustrated setup in Figs. 2.8(a), (c) and (e), respectively. Here, LWS stands for LW mode signal, and the first and second subscripts of LWS indicate the actuating and sensing PZT, respectively.



(b) Relative phases in the extracted LWS<sub>AA</sub> from (a). Here, the first and the second subscript indicate the actuator and the sensor, respectively.



(d) Relative phases in the extracted LWS<sub>BB</sub> from (c).



(f) Relative phases in the extracted  $\text{LWS}_{\text{AB}}(\text{LWS}_{\text{BA}})$  from (e).

At the absence of the notch,  $\text{LWS}_{\text{AA}}$  and  $\text{LWS}_{\text{BB}}$  should be identical because the mode-converted (MC) LW mode signals (the sum of  $S_0/A_0$  and  $A_0/S_0$ ) will not appear [Kim07]. However,  $\text{LWS}_{\text{AA}}$  and  $\text{LWS}_{\text{BB}}$  are

no longer identical when the notch is formed because the relative phases of the mode-converted LW mode signals become different. Due to the opposite polarization directions of PZTs A and B, the relative phases of  $S_0/S_0$  and  $A_0/A_0$  are in-phase while those of mode-converted LW mode signals (the sum of  $A_0/S_0$  and  $S_0/A_0$ ) are out-phase in  $LWS_{AA}$  and  $LWS_{BB}$  as shown in Fig. 2.8(b) and (d), respectively [Kim07]. In  $LWS_{AB}$  and  $LWS_{BA}$ , the relative phases of  $A_0/S_0$  and  $S_0/A_0$  are out-of-phase and cancel out completely. Therefore, no mode-converted LW mode signals appear in  $LWS_{AB}$  (or  $LWS_{BA}$ ) as shown in Fig. 2.8(f). Also,  $LWS_{AB}$  is always identical to  $LWS_{BA}$  due to the reciprocity of the linear elasto-dynamics [Fun65].

Based on this finding, Eq. (2.6) can be derived to decompose the measured LW mode signals in terms of individual LW modes, that is,  $S_0$ , MC and  $A_0$  modes:

$$\begin{Bmatrix} LWS_{AA}(t) \\ LWS_{BB}(t) \\ LWS_{AB}(t) \end{Bmatrix} = \begin{bmatrix} 1 & 1 & 1 \\ 1 & -1 & 1 \\ 1 & 0 & -1 \end{bmatrix} \begin{Bmatrix} LWS_{S_0}(t) \\ LWS_{MC}(t) \\ LWS_{A_0}(t) \end{Bmatrix} \quad (2.6)$$

By monitoring the appearance of mode-converted LW signal ( $LWS_{MC}$ ), the presence of damage can be identified without referring to any prior baseline LW signals.

In the following subsection, the decomposed LW due to the damage in the time domain will be transformed into EM spectrum by the fast Fourier transform (FFT). The characteristic of the decomposed LW in time domain is analyzed in the frequency domain and the change of frequency domain is analyzed according to the length of time domain

data. Specially, the correlation analysis of the decomposed  $LWS_{MC}$  and converted  $LWS_{MC}$  is a subject of major concern because the signal represents the damage.

## 2.4 Decomposition of Lamb Wave Mode Signals converging to the Steady-State Dynamic Response

In this subsection, the signal-decomposition technique of using EM signal is suggested. The following algebraic equation can be derived from the signal-decomposition technique as mentioned in section 2.3 and the temporal spectrum which shows the correlation between transient LW and steady-state signal such as impedance in section 2.2

It is well known that the modal dynamic responses of a structure are reflected on the EM signals measured by a PZT wafer [Par03]. More specifically,  $EMS_{ij}$  represents an EM signal being a frequency response function at the  $i$ 'th sensing PZT when an input driving voltage  $I$  is applied to the  $j$ 'th PZT wafer as follows:

$$EMS_{ij}(\omega) = \mathfrak{F}[LWS_{ij}(t)] / \mathfrak{F}[I(t)] \quad (2.7)$$

where  $\mathfrak{F}[\cdot]$  stands for Fourier transform operator,  $LWS_{ij}$  is the LW mode signal at the  $i$ 'th PZT corresponding to an input at the  $j$ 'th PZT, and  $\omega$  is the angular frequency.

From Eq. (2.6) and Eq. (2.7), the decomposed EM signals corresponding to each LW mode can be obtained:

$$\begin{Bmatrix} \text{EMS}_{S_0}(\omega) \\ \text{EMS}_{MC}(\omega) \\ \text{EMS}_{A_0}(\omega) \end{Bmatrix} = \begin{bmatrix} 1 & 1 & 1 \\ 1 & -1 & 1 \\ 1 & 0 & -1 \end{bmatrix}^{-1} \begin{Bmatrix} \text{EMS}_{AA}(\omega) \\ \text{EMS}_{BB}(\omega) \\ \text{EMS}_{AB}(\omega) \end{Bmatrix} \quad (2.8)$$

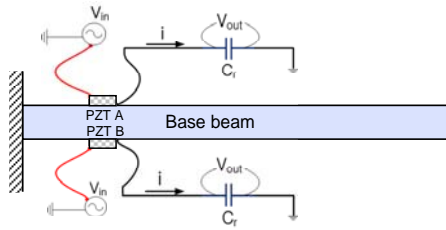
Both signal-decomposition techniques through the Eq.(2.6) algebraic using transient LW in time domain and the Eq.(2.8) algebraic using steady-state signal such as impedance are very useful method to diagnosis damage without the need for baseline signal. Especially, both  $\text{LWS}_{MC}$  and  $\text{EMS}_{MC}$  are the one of most notable in decomposed signals.

Therefore, additional signal analysis for mode-converted signal is conducted to investigate the characteristics of mode-converted signal and effectiveness of signal decomposition using the EMS. The signal analysis for mode-converted signal is divided into two cases which are excited as a harmonic and tone burst input on the PZT. Detailed process is provided in the following subsection.

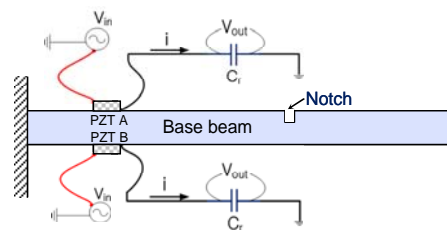
#### 2.4.1 Temporal spectrum of Mode-converted Signal by the Harmonic Input on the PZT.

In this subsection, temporal spectrum is conducted to investigate the characteristics of mode-converted signal when the harmonic input is applied to the collocated PZT wafers. Detailed dimension and geometry for the signal analysis are provided in Figs. 2.5. The implicit analysis of ABAQUS 6.7-4 on IBM p595 at KISTI Supercomputing Center [Kis10] was used as an analytical tool to analyze the transient LW signal. The Fig. 2.9(a) and (b) show intact and damaged cantilever beams which

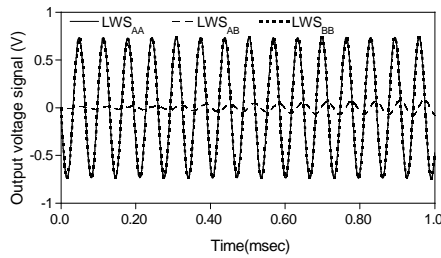
are excited by the collocated PZTs. Because the attached PZT wafers on the two beams can act as an actuator, the free surface of each collocated PZT wafer gets connected to a harmonic voltage source ( $V_{in}$ ) with an unit amplitude and their 11<sup>th</sup> natural frequencies, 15.4 kHz and 15.1 kHz, respectively. The other surface of each PZT wafer is tied to a sensing circuit consisting of a single capacitor ( $C_r = 3\text{nF}$ ) at the same time and the output voltage ( $V_{out}$ ) is measured at the sensing circuit as shown in Fig 2.9(a) and 2.9(b).



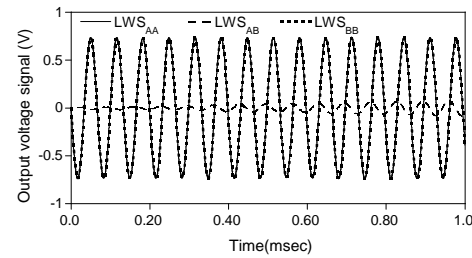
(a) An intact cantilever beam with collocated PZT wafers



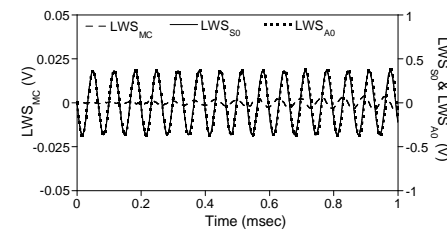
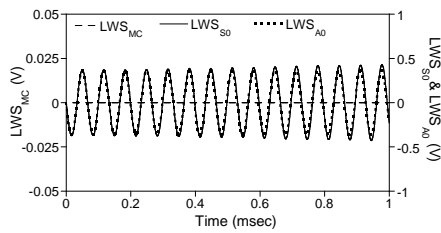
(b) A damaged cantilever beam with collocated PZT wafers



(c) LW mode signals measured from the intact cantilever beam



(d) LW mode signals measured from the damaged cantilever beam





(e) Decomposed LW mode signals of the intact cantilever beam (f) Decomposed LW mode signals of the damaged cantilever beam

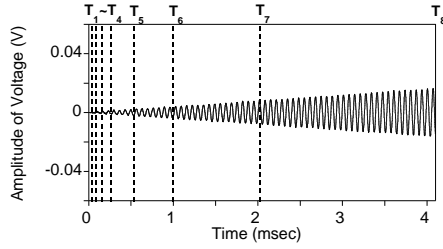
Fig. 2.9. Decomposition of the LW mode signals measured from the intact and damaged conditions when harmonic inputs are applied.

The LW mode signals measured from the intact and damaged beam conditions are presented in Fig. 2.9(c) and 2.9(d), respectively. The LW mode signals obtained by the collocated PZT wafers may be composed of either one or two components whether a single or two PZTs are used for LW excitation and sensing. The piezoelectric component induced by the coupling between the PZT wafers represents the dynamic response of the cantilever beam, and this component is always present. The second dielectric component induced by the driving input voltage source directly flowing into the actuating PZT wafer appears only when a single PZT is used for simultaneous excitation and sensing. In this regard,  $LWS_{AA}$  and  $LWS_{BB}$  contain both piezoelectric and dielectric components while  $LWS_{AB}$  contains the piezoelectric component only. The piezoelectric component in  $LWS_{AA}$  and  $LWS_{BB}$  is often masked by the large magnitude of the dielectric component and thus is not clearly observed in Figs 2.9(c) and (d). On the other hand, the piezoelectric component is clearly observed in  $LWS_{AB}$  displaying the resonant characteristics of the beam.

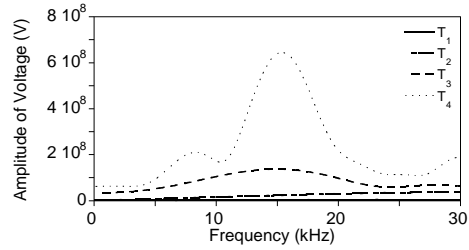
$LWS_{S_0}$ ,  $LWS_{A_0}$  and  $LWS_{MC}$  decomposed from  $LWS_{AA}$ ,  $LWS_{BB}$  and  $LWS_{AB}$  by using Eq.(2.6) are shown in Fig. 2.9(e) and 2.9(f), respectively. Here,  $LWS_{S_0}$  (or  $LWS_{A_0}$ ) contains the piezoelectric component associated with  $S_0$  (or  $A_0$ ) as well as the half of the

dielectric component in  $LWS_{AA}$  (or  $LWS_{BB}$ ). On the other hand, only the piezoelectric response exists within  $LWS_{MC}$ . Note that  $LWS_{MC}$  in Fig. 2.9(e) is a null signal because no mode conversion occurs in the intact cantilever beam. On the other hand,  $LWS_{MC}$  in Fig. 2.9(f) is observed clearly due to the mode conversion in the damaged beam.

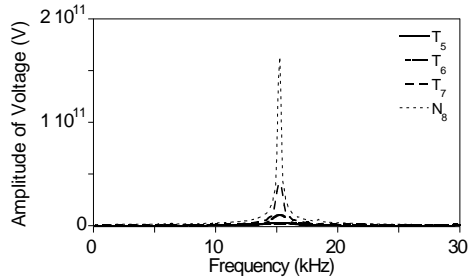
As shown in section 2.2, decomposed  $LWS_{MC}$  in Fig. 2.9(f) is only extracted for temporal spectrum between transient and steady state and the results are presented in Fig. 2.10.



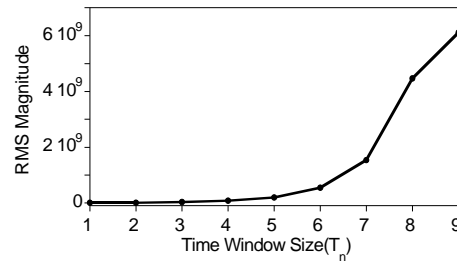
(a) Time windows for truncating the  $LWS_{MC}$  up to  $t = T_8$  for computing the temporal spectrums when harmonic input signals are imposed on the PZT. ( $T_1 \sim T_8 = 0.032 \sim 4.096$  msec).



(b) Time windows for truncating the  $LWS_{MC}$  up to  $T_4$  for computing the temporal spectrums when harmonic input signals are imposed on the PZT. Here,  $T_1 = 0.032$  msec and  $T_4 = 0.256$  msec.



(c) Time windows for truncating the  $LWS_{MC}$  up from  $T_5$  to  $T_8$  for computing the temporal spectrums when harmonic input



(d) The RMS values of the temporal spectrums in Figs. 7(b) and (c).

signals are imposed on the PZT.  
Here,  $T_5 = 0.512\text{msec}$  and  $T_8 = 4.096\text{msec}$ .

Fig. 2.10 Temporal spectrums of  $LWS_{MC}$  truncated by different time windows and RMS values when harmonic input signal is imposed.

In Fig. 2.10(a),  $LWS_{MC}$  up to 4.096 msec is truncated by time windows with increasing sizes. Here, the time intervals and the sizes of the time windows are identical to those in Subsection 2.2. The temporal spectrums of  $LWS_{MC}$  truncated by the time windows are calculated through FFT and presented in Fig. 2.10(b) and (c). Not that, the peaks of the temporal spectrums begin to appear in Fig. 2.10(b) and then one peak surges up near the resonance frequency ( $f = 15.1\text{kHz}$ ) in Fig. 2.10(c) as the time window size increases. The peak amplitude of the temporal spectrum is proportional to the size of the time window in Fig. 2.10(c). This implies that the mode-converted LW signals due to damage become resonant at the natural frequency of the cantilever beam. Fig. 2.10(d) demonstrates the root mean square (RMS) values of the temporal spectrums with respect to the time window size. The corresponding formula for a continuous function to calculate the RMS is defined as follows Fig. (2.11) and Eq. (2.9)

$$\begin{aligned}
 RMS &= \sqrt{\frac{1}{f_{\max} - f_{\min}} \int_{f_{\min}}^{f_{\max}} |X(f)|^2 df} \\
 X(f) &= \frac{(h_{i+1} - h_i)}{\Delta f} (f - f_i) + h_i = \sum_{i=0}^{N-1} \int_{f_i}^{f_{i+1}} \left[ \frac{h_{i+1} - h_i}{\Delta f} (f - f_i) + h_i \right] df \\
 [h_{i+1} &= h(f_{i+1}), \quad f_{i+1} = i \cdot \Delta f + f_{\min}, \quad 0 \leq i \leq N-1]
 \end{aligned} \tag{2.9}$$

Where,  $X(f)$  and  $f_i$  represent a continuous function and frequency.

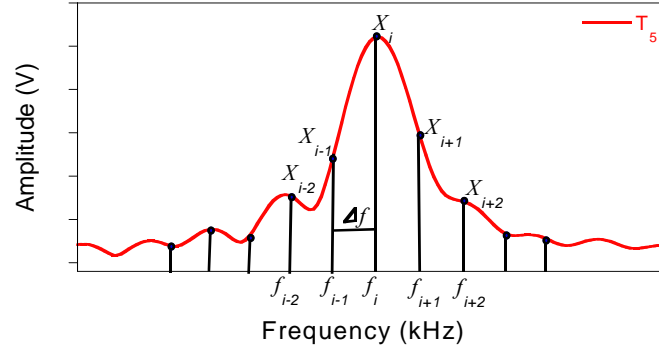
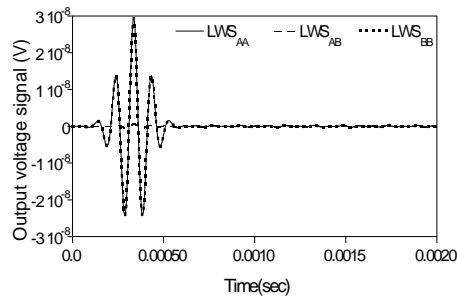


Fig 2.11 Calculation of the RMS from a continuous function.

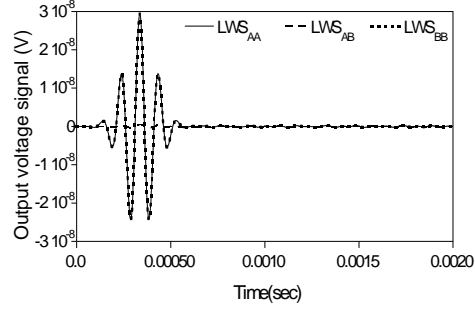
The RMS values are computed by numerically integrating the temporal spectrums from 6kHz to 24kHz (60% bandwidth of the driving frequency 15.1kHz). Beginning from  $T_5$  ( $=0.512\text{msec}$ ) the RMS values of the temporal spectrums begin to increase rapidly. The signal to noise ratio (S/N ratio) associated with the mode-converted LW signal is improved through the resonance behavior of a structure.

#### 2.4.2 Temporal Spectrum of Mode-Converted Signal by the Tone Burst Input on the PZT.

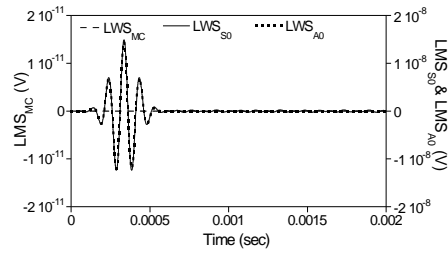
As in Subsection 2.2, 10kHz tone burst input signal is applied and then LW signals are generated and received by a pair of PZT wafers on an intact and damaged cantilever beams in Figs. 2.12(a) and (b). LW signals for the three combinations of sensing and actuating PZTs are shown in Figs. 2.12(a) and (b).



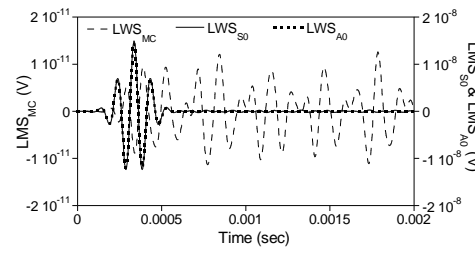
(a) LW mode signals measured from the intact cantilever beam



(b) LW mode signals measured from the damaged cantilever beam



(c) Decomposed LW mode signals of the intact cantilever beam



(d) Decomposed LW mode signals of the damaged cantilever beam

Fig. 2.12. Decomposition of the LW mode signals when tone burst input with 10kHz center frequency are applied.

Then these LW signals are decomposed into S0, A0 and MC modes through signal-decomposition in Eq.(2.6) as shown in Figs. 2.12(c) and 2.12(d), respectively. For the intact cantilever beam, the mode-converted LW signal is null because there is no source of mode conversion. In case of the damaged beam, it appears clearly because damage on the beam causes the mode conversion. Thus, the existence of damage can be confirmed without referring to prior baseline information.

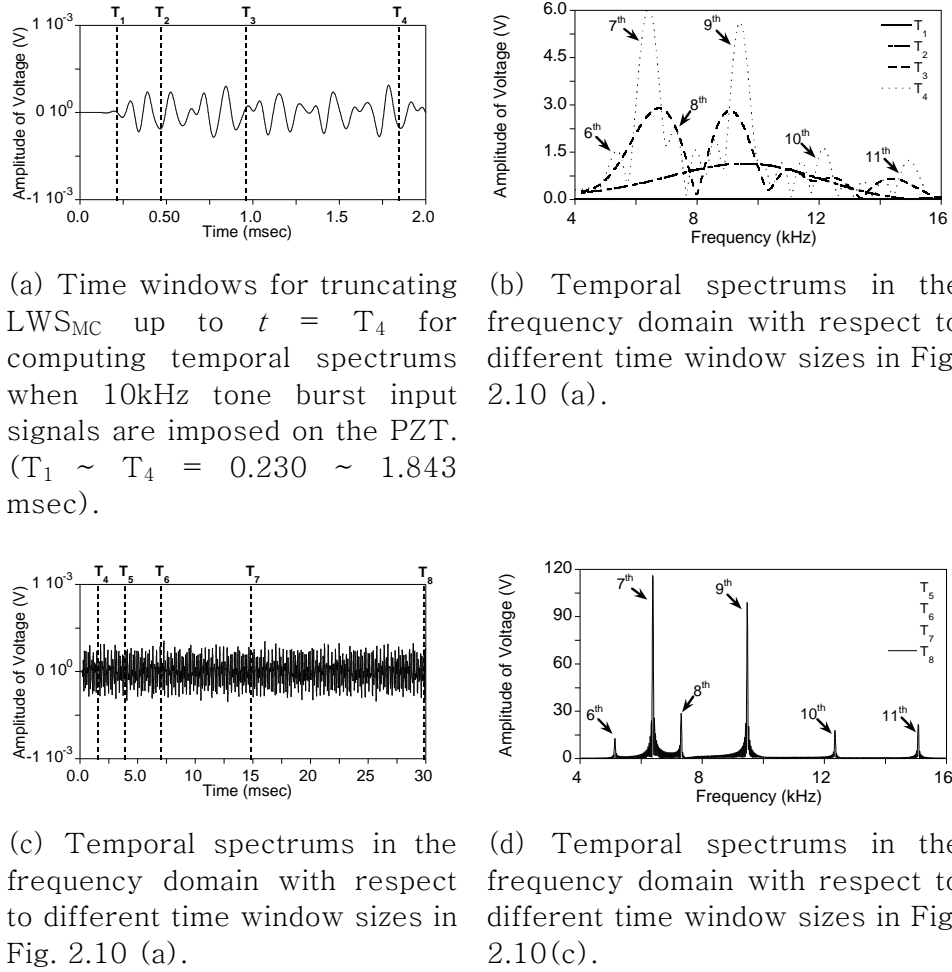
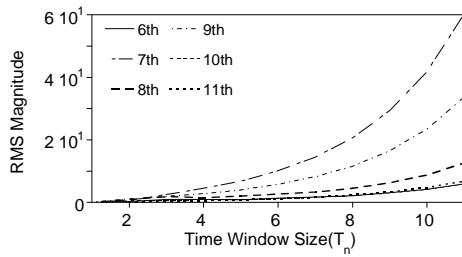


Fig. 2.13 Temporal spectrums of  $LWS_{MC}$  when 10kHz tone burst input signal is imposed.

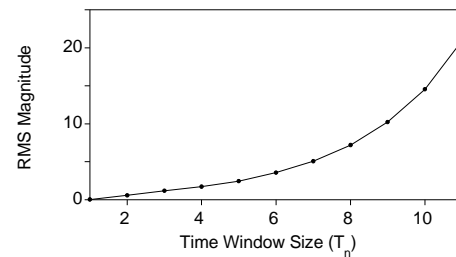
In Fig. 2.13(a) and 2.13(c),  $LWS_{MC}$  up to 2.0 msec and 30msec are truncated by time windows with increasing sizes. Here, the time intervals and sizes of time windows are identical to those in Subsection 2.2. The temporal spectrums of  $LWS_{MC}$  truncated by the time windows are computed through FFT and presented in Figs. 2.13(b) and 2.13(d).

When the time window size is very small, e.g.  $T_2(=0.461 \text{ msec})$ , the peak of the temporal spectrum appears at the input driving frequency ( $=10\text{kHz}$ ). As the time window sizes increase, several peaks begin to appear at different frequencies and their amplitudes increase in Fig. 2.13(b). When the time windows size become large enough, the peaks surge up and converge to the natural frequencies from the 6<sup>th</sup> to 11<sup>th</sup> mode of the cantilever beam in Fig. 2.13(d). Similar to the harmonic input excitation in Subsection 2.3.1, the mode-converted LW signals due to damage become resonant when a tone burst input excitation takes place.

The RMS values of the temporal spectrums with respect to time window size are demonstrated in Fig. 2.14. As the time window sizes increase, individual and total RMS values increase monotonically increase in Fig. 2.14(a) and 2.14(b). This implies that the S/N ratio associated with the mode-converted LW signal due to damage is improved through the resonance behavior of a structure regardless of the modal characteristics of the structure



(a) The RMS values of the temporal spectrums associated with individual modes.



(b) The total RMS values of the temporal spectrums associated with overall mode.

Fig. 2.14 RMS values when tone burst input signal is imposed on the top PZT of a cantilever beam.

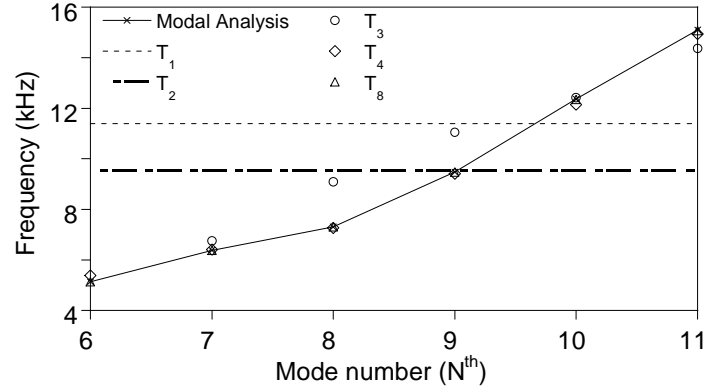
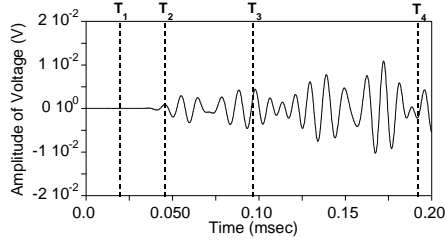


Fig. 2.15 Determination of time window size through the comparing mode in the modal and temporal spectrum analysis.

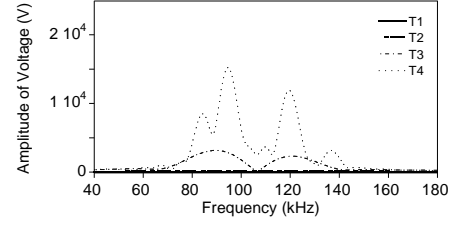
When the 10kHz Tone burst input is excited on the PZT wafer, Fig. 2.15 shows the comparing modes from 6<sup>th</sup> to 11<sup>th</sup> through temporal spectrum and modal analysis. In the initial time window size  $T_1$  and  $T_2$ , the temporal spectrum have a single mode related on 10kHz input frequency range and each modes does not appear. As time window size is increased from  $T_3$  to  $T_8$ , each modes of temporal spectrum is going to close the modes by modal analysis as shown Fig. 2.13(b) and 2.13(d) because modal characteristic of the horst structure is considered. Therefore, it is possible that we determine a proper time window size for effective damage detection.

Similarly, the temporal spectrum will be shown on the following Fig. 2.16 when the input voltage signal is excited as tone burst type with 100kHz center frequency. The analysis model to get the  $LWS_{MC}$  is equal to the Fig 2.9(a) and (b).

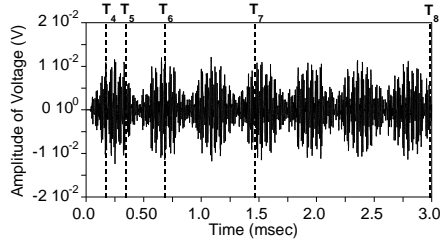




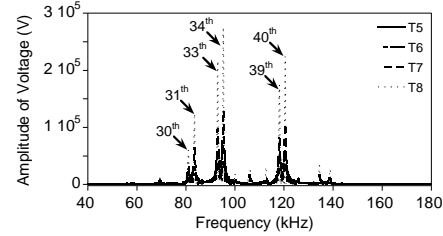
(a) Time windows for truncating  $LWS_{MC}$  up to  $t = T_4$  for computing temporal spectrums when 100 kHz tone burst input signals are imposed on the PZT. ( $T_1 \sim T_4 = 0.230 \sim 1.843$  msec).



(b) Temporal spectrums in the frequency domain with respect to different time window sizes in Fig. 2.16 (a).



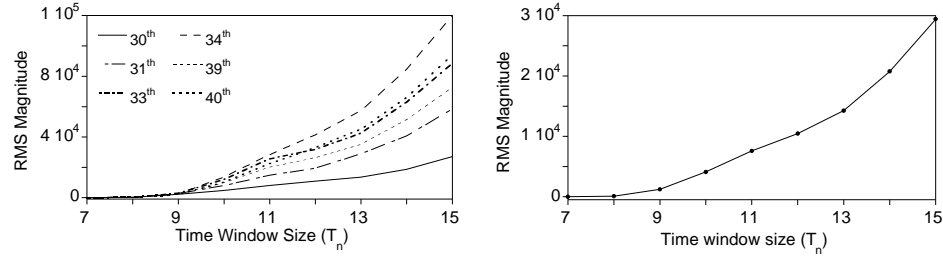
(c) Time windows for truncating  $LWS_{MC}$  up to  $t = T_8$  for computing temporal spectrums when 100kHz tone burst input signals are imposed. ( $T_5 \sim T_8 = 3.686 \sim 29.491$  msec).



(d) Temporal spectrums in the frequency domain with respect to different time window sizes in Fig. 2.16(c).

Fig. 2.16 Temporal spectrums of  $LWS_{MC}$  truncated by different time windows when 100kHz tone burst input signal is imposed.

Because the excitation input is applied to tone burst type with 100kHz center frequency, Time scale of the  $LWS_{MC}$  in the Fig. 2.16 (a) and (c) and the frequency scale of temporal spectrum in Fig. 2.16(b) and (d) are different as Fig. 2.13. But, the other conditions and results are the same.



(a) The RMS values of the temporal spectrums associated with individual modes  
 (b) The total RMS values of the temporal spectrums associated with overall mode.

Fig. 2.17 RMS values when 100kHz tone burst input signal is imposed.

The RMS values by the 100kHz tone burst input will be shown in the Fig. 2.17. In the Fig. 2.16(d), the many resonance frequency is generated when the 100kHz tone burst is excited. The RMS values of some selected mode are presented in the Fig 2.17(a) and the total RMS value as shown Fig. 2.17(b) is calculated by numerically integrating the temporal spectrums from 40kHz  $\sim$  160kHz (60% bandwidth of the driving frequency 100kHz).

To the authors' best knowledge, this is the first study that decomposes the mode-converted LWS( $LWS_{MC}$ ) from the modal harmonic motions of the structure and explicitly investigates its resonance characteristics. The steady-state signal such as impedance signal could be obtained through the superposition that sufficient time has been passed in the time domain analysis using the transient LW as the mode shape in Fig. 2.5.

### 2.4.3 Summary.

So far, some important implications drawn from these observations are summarized as follows: (i) We know that the LW and EM signals are not a separate signal through the temporal spectrum which is very important meaning to understand EM signal. The EM signal can be obtained from LW signal with enough time length to make the resonance of host structure. (ii) The presence of damage can be identified without referring to any baseline signals through Eq. (2.8) even after LW signals have converted to the steady-state response of a structure. (iii) The one of important view in signal-decomposition by harmonic and tone burst input is increasing the mode-converted (MC) signal according to the time. Of course, it is not important that the signal can have a periodic or may not have. (iv) The damage detection using temporal spectrum or EM signal can be improved particularly in case of an incipient damage because the magnitude of mode-converted LWS ( $LWS_{MC}$ ) shall be amplified through the resonance of the structure. (v) As the temporal spectrum is close to the EM signal, the RMS values are a gradual increase. Therefore, temporal spectrum or EM signal in the frequency domain is much better effect than the LW signal in damage detection when damage is identified to the damage signal such as mode-converted signal.

In the following section 3, the numerical modeling and analysis techniques for damage detection using EM signal will be proposed.

## Chapter 3

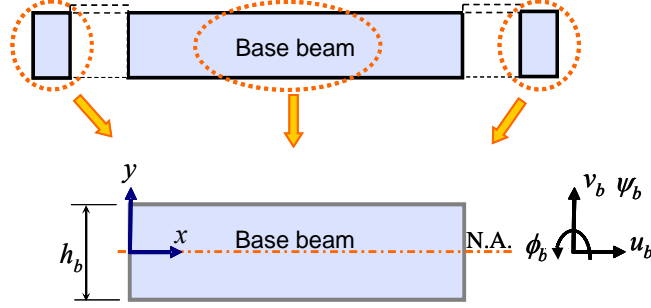
### Spectral Element Formulation for EM Interaction between PZT and Structure

#### 3.1 Equation of Motion

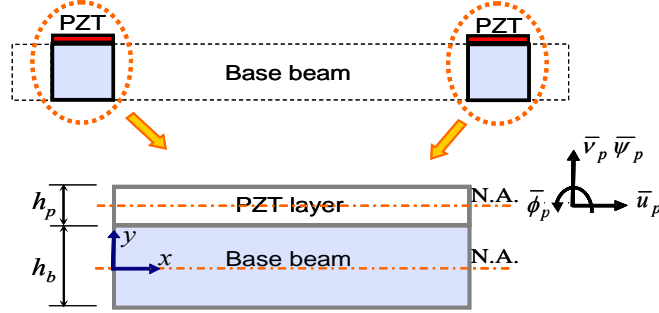
In the previous chapter, we show that the  $EMS_{MC}$  is very useful signal to identify a notch like damage. This chapter will propose a numerical full modeling technique using spectral element for more effective calculation of the  $EMS_{MC}$ .

Before the proposed spectral element formulation to compute the EM signal, the equations of motion need to formulate about a spectral element models. Fig. 3.1 shows the schematic application range and shape of each spectral element models in arbitrary analysis model like as plate. Fig. 3.1(a) is simply base beam element. Fig 3.1(b) and 3.1(c) illustrate a coupled PZT wafer and beam system (CPBS) in which PZT wafers are rigidly bonded on a base beam. The PZT wafers on the base beam can alternate the functionality of being an actuator and a sensor. Two types of a CPBS widely adopted in structural health monitoring applications are considered [Rag07, Par03, Kim07]. One is a CPBS with a single PZT wafer in Fig. 3.1(b) and the other with collocated PZT wafers in Fig. 3.1(c). Two dimensional plane stress or strain condition is assumed for the CPBS in Fig. 3.1. The longitudinal and flexural behaviors of the base beam are approximated through the Mindlin–Herrmann theory and the Timoshenko beam theory,

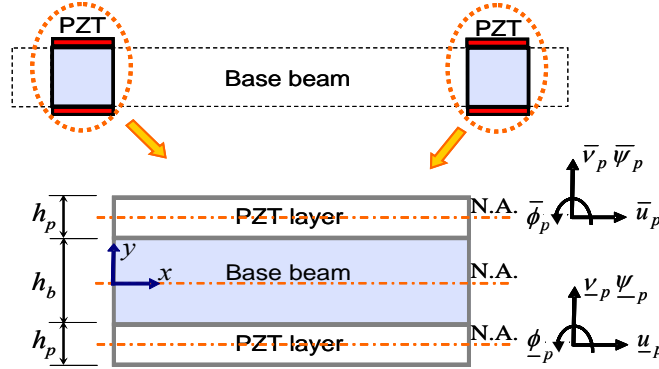
respectively. The axial deformation and lateral contraction occurring normal to the neural axis of the base beam are considered in the Mindlin–Herrmann theory while the rotational inertia effect and shear deformation are represented in the Timoshenko beam theory [Fun65].



(a) a single beam model



(b) a CPBS with a single PZT wafer.



(c) a CPBS with collocated PZT wafers.

Fig. 3.1. Schematic illustration of a coupled PZT and beam system (CPBS)

The PZT wafers bonded on the base beam in Fig. 3.1 are relatively thin compared to the base beam and the higher-order mechanical behaviors in the base beam are assumed to be negligible in the PZT wafer. In this regard, the longitudinal and flexural behaviors in the PZT wafer are represented by the elementary rod theory and the Euler–Bernoulli beam theory, respectively [Lee00]. The EM behaviors of the PZT wafer are assumed to follow one dimensional linear piezoelectricity [Ike90]. Because the equations of motion for a single base beam have been previously formulated [Kra06, Kra03], this section focuses on deriving the equations of motion for the CPBS in Fig. 3.1. The corresponding spectral element formulation for the CPBS will be presented in Section 3.2

### 3.1.1 Kinematic and Constitutive Assumptions of a CPBS

The displacement field  $u$  and  $v$  in the domain of the base beam in Fig. 3.1 is defined by the following equations based upon the Timoshenko beam theory and the Mindlin–Herrmann theory [Roy03]:

$$\begin{aligned} u(x, y, t) &= u_b(x, t) - y\phi_b(x, t) & (-\frac{h_b}{2} \leq y \leq \frac{h_b}{2}) \\ v(x, y, t) &= v_b(x, t) + y\psi_b(x, t) \end{aligned} \quad (3.1)$$

where  $u_b$ ,  $\psi_b$ ,  $v_b$ ,  $\phi_b$  and  $h_b$  represent horizontal displacement, lateral contraction rate, vertical displacement, rotational angle on the neutral

axis of the base beam, and the thickness of the base beam, respectively.

The displacement field in the domain of the PZT wafer in Fig. 3.1(b) and (c) is defined as follows using the Euler–Bernoulli beam theory and the elementary rod theory:

$$\bar{u}(x, y, t) = \bar{u}_p(x, t) - (y - H)\bar{\phi}_p(x, t) \quad \left(\frac{h_b}{2} \leq y \leq \frac{h_b}{2} + h_p\right) \quad (3.2a)$$

$$\bar{v}(x, y, t) = \bar{v}_p(x, t)$$

$$\underline{u}(x, y, t) = \underline{u}_p(x, t) - (y + H)\underline{\phi}_p(x, t) \quad \left(-\frac{h_b}{2} - h_p \leq y \leq -\frac{h_b}{2}\right) \quad (3.2b)$$

$$\underline{v}(x, y, t) = \underline{v}_p(x, t)$$

where  $u_p$ ,  $v_p$ ,  $\phi_p$  and  $h_p$  denote horizontal displacement, vertical displacement, rotational angle on the neutral axis of the PZT wafer and the thickness of the PZT wafer, respectively while  $H = (H_b + H_p)/2$ . Furthermore, the over- and under- bars of each variable indicate the PZT wafers mounted on the top and bottom of the base beam, respectively. Note that  $\bar{\phi}_p = d\bar{v}_p/dx$  and  $\underline{\phi}_p = d\underline{v}_p/dx$  based upon the Euler–Bernoulli beam theory. For simplicity,  $t$  in field variables will be omitted unless otherwise mentioned.

Assuming that the PZT wafers are perfectly bonded on the base beam in Fig. 3.1(b) and (c), the compatibility condition is imposed on interfaces between the base beam and the PZT wafers as follows:

$$\bar{u}\left(x, \frac{h_b}{2}\right) = u\left(x, \frac{h_b}{2}\right) \quad (3.3a)$$

$$\begin{aligned}
\bar{v}(x, \frac{h_b}{2}) &= v(x, \frac{h_b}{2}) \\
\bar{u}(x, -\frac{h_b}{2}) &= u(x, -\frac{h_b}{2}) \\
\bar{v}(x, -\frac{h_b}{2}) &= v(x, -\frac{h_b}{2})
\end{aligned} \tag{3.3b}$$

Substituting Eqs. (3.1) and (3.2) into Eq. (3.3), it can be shown that the response variables on the neutral axis of the PZT wafers can be represented with those of the base beam [Lim08]:

$$\begin{aligned}
\bar{u}_p(x) &= u_b(x) - \frac{h_b}{2} \left[ \frac{h_p}{2} \cdot \psi'_b(x) + \phi_b(x) \right] - \frac{h_p}{2} \cdot v'_b(x) \\
\bar{v}_p(x) &= v_b(x) + \frac{h_b}{2} \psi'_b(x)
\end{aligned} \tag{3.4a}$$

$$\begin{aligned}
\bar{\phi}_p(x) &= v'_b(x) + \frac{h_b}{2} \cdot \psi'_b(x) \\
\bar{u}_p(x) &= u_b(x) - \frac{h_b}{2} \left[ \frac{h_p}{2} \cdot \psi'_b(x) - \phi_b(x) \right] + \frac{h_p}{2} \cdot v'_b(x) \\
\bar{v}_p(x) &= v_b(x) - \frac{h_b}{2} \psi'_b(x) \\
\bar{\phi}_p(x) &= v'_b(x) - \frac{h_b}{2} \cdot \psi'_b(x)
\end{aligned} \tag{3.4b}$$

where (') denotes a derivative operator with respect to  $x$ .

Because the 3-1 type single sheet PZT wafer is employed in this study, the EM behavior of the PZT wafer is defined based upon one-dimensional linear piezoelectricity [Lee00]:



$$\begin{Bmatrix} \sigma(x) \\ E(x) \end{Bmatrix} = \begin{bmatrix} C_{11}^D & -h_{31} \\ -h_{31} & B_{33}^S \end{bmatrix} \begin{Bmatrix} \varepsilon(x) \\ D(x) \end{Bmatrix} \quad (3.5)$$

where  $\sigma, \varepsilon, C_{11}^D, E, B_{33}^S, h_{31}$ , and  $D$  denote the normal stress, the normal strain, the elastic modulus, the electric field, the dielectric constant, the piezoelectric constant and the electric displacement of the PZT wafer, respectively [Ike90]. The superscript  $D$  and  $S$  on  $C_{11}^D$  and  $B_{33}^S$  indicate that the corresponding constants are measured under zero electric displacement and zero strain, respectively. For simplicity,  $x$  will be omitted unless otherwise mentioned hereafter.

Note that the EM properties of the collocated PZT wafers in Fig. 3.1(c) are identical if the polarization directions of the collocated wafers are same. If the polarization directions of the PZT wafers are opposite, then the piezoelectric constants will have same absolute values with opposite signs [Kim07].

$$\begin{aligned} \bar{C}_{11}^D &= \underline{C}_{11}^D = C_{11}^D \\ \bar{B}_{33}^S &= \underline{B}_{33}^S = B_{33}^S \\ \bar{h}_{31} &= \underline{h}_{31} & (\text{same polarization directions}) \\ \bar{h}_{31} &= -\underline{h}_{31} & (\text{opposite polarization directions}) \end{aligned} \quad (3.6)$$

### 3.1.2 Deriving the Equations of Motion of a CPBS through the Hamilton's Principle

In this subsection, the equations of motion are derived for the CPBS with the collocated PZT wafers in Fig. 3.1(c). Note that the

equations of motion in this case can be reduced back to the CPBS with a single PZT wafer in Fig. 3.1(b) by simply eliminating the terms associated with the bottom PZT wafer of the CPBS in Fig. 3.1(c).

Using Eqs. (3.1), (3.2) and (3.5), the linear strain-displacement relations and the Hooke's law of an elastic continuum [Fun65], the strain energy ( $U$ ) of the CPBS is formulated as follows [Lee00].

$$\begin{aligned}
 U = & \frac{1}{2} \int_0^L [E_b I_b \phi_b'^2 + \mu_b A_b K_1 (v_b' - \phi_b)^2] dx \\
 & + \frac{1}{2} \int_0^L [(2\mu_b + \lambda_b) A_b (u_b'^2 + \psi_b'^2) + 2\lambda_b A_b u_b' \psi_b' + \mu_b I_b \kappa_1 \psi_b'^2] dx \\
 & + \frac{1}{2} \int_0^L [C_{11}^D A_p (\bar{u}_p'^2 + \underline{u}_p'^2) + C_{11}^D I_p (\bar{\phi}_p'^2 + \underline{\phi}_p'^2) - 2A_p (\bar{h}_{31} \bar{D} \bar{u}_p' + \underline{h}_{31} \underline{D} \underline{u}_p') \\
 & + A_p B_{33}^S (\bar{D}^2 + \underline{D}^2)] dx
 \end{aligned} \tag{3.7}$$

where  $L$ ,  $E_b$ ,  $I_b$  and  $A_b$  represent the length of the CPBS, the elastic modulus, the second moment of the inertia and the area of the base beam, respectively. Furthermore,  $I_p$  and  $A_p$  denote the second moment of the inertia and the area of the PZT wafer, respectively, while  $\mu_b$  and  $\lambda_b$  are Lamé constants of the base beam.  $K_1$  and  $\kappa_1$  are control parameters employed in the Timoshenko beam theory and the Mindlin-Herrmann rod theory, respectively [Doy97, Fun65]. It is noted that the elastic module  $E_b$ ,  $\lambda_b$  and  $C_{11}^D$  in Eq. (3.7) should be appropriately modified depending on whether a given problem is under the plane stress or plane strain condition.

Similar to Eq. (3.7), the kinetic energy ( $T$ ) of the CPBS is derived

as:

$$\begin{aligned}
 T = & \frac{1}{2} \int_0^L \rho_b (I_b K_2 \dot{\phi}_b^2 + A_b \dot{v}_b^2) dx + \frac{1}{2} \int_0^L \rho_b (A_b \dot{u}_b^2 + I_b \kappa_2 \dot{\psi}_b^2) dx \\
 & + \frac{1}{2} \int_0^L \rho_p A_p (\dot{\bar{u}}_p^2 + \dot{\bar{v}}_p^2 + \dot{\underline{u}}_p^2 + \dot{\underline{v}}_p^2) dx
 \end{aligned} \tag{3.8}$$

where  $\rho_b$  and  $\rho_p$  denote the density of the base beam and the PZT wafer, respectively while  $K_2$  and  $\kappa_2$  are control parameters used in the Timoshenko beam theory and the Mindlin–Herrmann rod theory, respectively [Doy97, Fun65]. The dot on field variables denotes a derivative operator with respect to time.

The potential energy ( $\Omega$ ) of the CPBS is obtained as follows:

$$\begin{aligned}
 \Omega = & - \int_0^L [q_u u_b + q_\psi \psi_b + q_v v_b + q_\phi \phi_b + w_p (\bar{v} \bar{D} + \underline{v} \underline{D})] dx \\
 & - (F u_b + Q \psi_b + V v_b + M \phi_b) \Big|_0^L
 \end{aligned} \tag{3.9}$$

where  $q_u$ ,  $q_\psi$ ,  $q_v$  and  $q_\phi$  are the axial force, the contraction force, the shear force and the rotational moment per unit length imposed on the neutral axis of the base beam, respectively.  $w_p$ ,  $\bar{v}$ ,  $F$ ,  $Q$ ,  $V$  and  $M$  denote the width of the PZT wafer, the voltage applied to the PZT wafer, the axial force, the contraction force, the shear force and the rotational moment at the both ends of the base beam on the neutral axis.

Once the strain, kinetic and strain energies of the CPBS are formulated, the Hamilton's principle is used to derive the equations of

motion [Fun65]:

$$\delta \int_{t_1}^{t_2} [-U + T - \Omega] dt = 0 \quad (3.10)$$

Substituting Eqs. (3.7)–(3.9) into Eq. (3.10), the governing equations and the force boundary conditions are represented in terms of the variations of the response variables. Due to the space limitation, detailed mathematical manipulation is omitted.

– Governing equations ( $0 < x < L$  and  $t > 0$ )

$$\begin{aligned} & \rho_b A_b \ddot{u}_b + \rho_p A_p (\ddot{\underline{u}}_p + \ddot{\underline{u}}_p) - (2\mu_b + \lambda_b) A_b u_b'' - \lambda A_b \psi_b' - C_{11}^D A_p (\bar{u}_p'' + \underline{u}_p'') \\ & + A_p (\bar{h}_{31} \bar{D}' + \underline{h}_{31} \underline{D}') = q_u \end{aligned} \quad (3.11a)$$

$$\begin{aligned} & \kappa_2 \rho_b I_b \ddot{\psi}_b + \frac{\rho_p A_p h_b}{2} [(\ddot{\bar{v}}_p - \ddot{\underline{v}}_p) + \frac{h_p}{2} (\ddot{\bar{u}}_p' + \ddot{\underline{u}}_p')] + \lambda_b A_b u_b' + (2\mu_b + \lambda_b) A_b \psi_b \\ & - \kappa_1 \mu_b I_b \psi_b'' - \frac{C_{11}^D A_p h_b h_p}{4} (\bar{u}_p''' + \underline{u}_p''') + \frac{A_p h_b h_p}{4} (\bar{h}_{31} \bar{D}'' + \underline{h}_{31} \underline{D}'') \\ & + \frac{C_{11}^D I_p h_b}{2} (\bar{\phi}_p''' - \phi_p''') = q_\psi \end{aligned} \quad (3.11b)$$

$$\begin{aligned} & \rho_b A_b \ddot{v}_b + \rho_p A_p \left[ \frac{h_p}{2} (\ddot{\bar{u}}_p' - \ddot{\underline{u}}_p') + (\ddot{\bar{v}}_p + \ddot{\underline{v}}_p) \right] - K_1 \mu_b A_b (v_b'' - \phi_b') \\ & - \frac{C_{11}^D A_p h_p}{2} (\bar{u}_p''' - \underline{u}_p''') + \frac{A_p h_p}{2} (\bar{h}_{31} \bar{D}'' - \underline{h}_{31} \underline{D}'') + C_{11}^D I_p (\bar{\phi}_p''' + \phi_p''') = q_v \end{aligned} \quad (3.11c)$$

$$K_2 \rho_b I_b \ddot{\phi}_b - \frac{\rho_p A_p h_b}{2} (\ddot{u}_p - \ddot{u}_p) - E_b I_b \phi_b'' - K_1 \mu_b A_b (v_b' - \phi_b) + \frac{C_{11}^D A_p h_b}{2} (\bar{u}_p'' - \underline{u}_p'') - \frac{A_p h_b}{2} (\bar{h}_{31} \bar{D}' - \underline{h}_{31} \underline{D}') = q_\phi \quad (3.11d)$$

$$A_p \bar{h}_{31} \bar{u}_p' - A_p B_{33}^S \bar{D} + w_p \bar{v} = 0 \quad (3.11e)$$

$$A_p \underline{h}_{31} \underline{u}_p' - A_p B_{33}^S \underline{D} + w_p \underline{v} = 0 \quad (3.11f)$$

where Eqs. (3.11a)–(3.11f) are associated with the variations of field variables  $\delta u_b$ ,  $\delta \psi_b$ ,  $\delta v_b$ ,  $\delta \phi_b$ ,  $\delta \bar{D}$  and  $\delta \underline{D}$ .

– Force boundary conditions ( $x = [0 \text{ or } L]$  and  $t > 0$ )

$$(2\mu_b + \lambda_b) A_b u_b' + \lambda_b A_b \psi_b + C_{11}^D A_p (\bar{u}_p' + \underline{u}_p') - A_p (\bar{h}_{31} \bar{D} + \underline{h}_{31} \underline{D}) = F \quad (3.12a)$$

$$\kappa_1 \mu_b I_b \psi_b' - \frac{\rho_p A_p h_b h_p}{4} (\ddot{u}_p + \ddot{u}_p) + \frac{C_{11}^D A_p h_b h_p}{4} (\bar{u}_p'' + \underline{u}_p'') - \frac{A_p h_{31} h_b h_p}{4} (\bar{D}' + \underline{D}') - \frac{C_{11}^D I_p h_b}{2} (\bar{\phi}_p'' - \underline{\phi}_p'') = Q \quad (3.12b)$$

$$K_1 \mu_b A_b (v_b' - \phi_b) - \frac{\rho_p A_p h_p}{2} (\ddot{u}_p - \ddot{u}_p) + \frac{C_{11}^D A_p h_p}{2} (\bar{u}_p'' - \underline{u}_p'') - \frac{A_p h_p}{2} (\bar{h}_{31} \bar{D}' - \underline{h}_{31} \underline{D}') - C_{11}^D I_p (\bar{\phi}_p'' + \underline{\phi}_p'') = V \quad (3.12c)$$

$$E_b I_b \phi_b' - \frac{C_{11}^D A_p h_b}{2} (\bar{u}_p' - \underline{u}_p') + \frac{A_p h_b}{2} (\bar{h}_{31} \bar{D} - \underline{h}_{31} \underline{D}) = M \quad (3.12d)$$

$$\frac{C_{11}^D A_p h_b h_p}{4} (\bar{u}_p' + \underline{u}_p') - \frac{A_p h_b h_p}{4} (\bar{h}_{31} \bar{D} + \underline{h}_{31} \underline{D}) - \frac{C_{11}^D I_p h_b}{2} (\bar{\phi}_p' - \underline{\phi}_p') = 0 \quad (3.12e)$$

$$\frac{C_{11}^D A_p h_p}{2} (\bar{u}_p' - \underline{u}_p') - \frac{A_p h_p}{2} (\bar{h}_{31} \bar{D} - \underline{h}_{31} \underline{D}) - C_{11}^D I_p (\bar{\phi}_p' + \underline{\phi}_p') = 0 \quad (3.12f)$$

where Eqs. (3.12a)–(3.12e) are associated with the variations of field variables  $\delta u_b$ ,  $\delta \psi_b$ ,  $\delta v_b$ ,  $\delta \phi_b$ ,  $\delta \psi'_b$  and  $\delta v'_b$ .

Substituting  $\varepsilon = u'_p$  and  $E = v/h_p$  into Eq. (3.5), the electric displacement  $D$  and its derivatives are represented with respect to the axial displacement ( $u_p$ ) on the neutral axis and the voltage ( $v$ ) of the PZT wafer:

$$\bar{D} = \frac{\bar{h}_{31}}{B_{33}^S} \bar{u}'_p + \frac{w_p \bar{v}}{A_p B_{33}^S}, \quad \bar{D}' = \frac{\bar{h}_{31}}{B_{33}^S} \bar{u}''_p, \quad \bar{D}'' = \frac{\bar{h}_{31}}{B_{33}^S} \bar{u}'''_p \quad (3.13a)$$

$$\underline{D} = \frac{h_{31}}{B_{33}^S} \underline{u}'_p + \frac{w_p v}{A_p B_{33}^S}, \quad \underline{D}' = \frac{h_{31}}{B_{33}^S} \underline{u}''_p, \quad \underline{D}'' = \frac{h_{31}}{B_{33}^S} \underline{u}'''_p \quad (3.13b)$$

Note that the distribution of voltage across each PZT wafer is assumed to be uniform, and its spatial derivatives become zero in Eq. (3.13).

Substituting Eq. (3.13) into Eq. (3.11), six governing equations in Eq. (3.11) can be reduced to four equations with respect to  $\delta u_b$ ,  $\delta \psi_b$ ,  $\delta v_b$  and  $\delta \phi_b$  because Eqs. (3.11e) and (3.11f) are equivalent to Eq. (3.13a) and (3.13b), respectively.

– Governing equations ( $0 < x < L$  and  $t > 0$ )

$$\rho_b A_b \ddot{u}_b + \rho_p A_p (\ddot{\bar{u}}_p + \ddot{\underline{u}}_p) - (2\mu_b + \lambda_b) A_b u''_b - \lambda_b A_b \psi'_b - E_p A_p (\bar{u}''_p + \underline{u}''_p) = q_u \quad (3.14a)$$

$$\kappa_2 \rho_b I_b \ddot{\psi}_b + \frac{\rho_p A_p h_b}{2} [(\ddot{\bar{v}}_p - \ddot{\underline{v}}_p) + \frac{h_p}{2} (\ddot{\bar{u}}'_p + \ddot{\underline{u}}'_p)] + \lambda A_b u'_b + (2\mu_b + \lambda_b) A_b \psi_b$$

$$- \kappa_1 \mu I_b \psi''_b - \frac{E_p A_p h_b h_p}{4} (\bar{u}'''_p + \underline{u}'''_p) + \frac{C_{11}^D I_p h_b}{2} (\bar{\phi}'''_p - \underline{\phi}'''_p) = q_\psi \quad (3.14b)$$

$$\rho_b A_b \ddot{v}_b + \rho_p A_p \left[ \frac{h_p}{2} (\ddot{\bar{u}}'_p - \ddot{\underline{u}}'_p) + (\ddot{\bar{v}}_p + \ddot{\underline{v}}_p) \right] - K_1 \mu_b A_b (v''_b - \phi'_b)$$

$$- \frac{E_p A_p h_p}{2} (\bar{u}'''_p - \underline{u}'''_p) + C_{11}^D I_p (\bar{\phi}'''_p + \underline{\phi}'''_p) = q_v \quad (3.14c)$$

$$\begin{aligned}
& K_2 \rho_b I_b \ddot{\phi}_b - \frac{\rho_p A_p h_b}{2} (\ddot{u}_p - \ddot{u}_p) - E_b I_b \phi_b'' - K_1 \mu_b A_b (v_b' - \phi_b) \\
& + \frac{E_p A_p h_b}{2} (\bar{u}_p'' - \underline{u}_p'') = q_\phi
\end{aligned} \tag{3.14d}$$

Where,  $E_p = C_{11}^D - \bar{h}_{31}^2 / B_{33}^S = C_{11}^D - \underline{h}_{31}^2 / B_{33}^S$ .

In a similar fashion, substituting Eq. (3.12) into Eq. (3.11) yields the following force boundary conditions:

– Force boundary conditions ( $x = [0 \text{ or } L]$  and  $t > 0$ )

$$(2\mu_b + \lambda_b) A_b u_b' + \lambda_b A_b \psi_b + E_p A_p (\bar{u}_p' + \underline{u}_p') - E_p w_p (\bar{d}_{31} \bar{v} + \underline{d}_{31} \underline{v}) = F \tag{3.15a}$$

$$\begin{aligned}
& \kappa_1 \mu_b I_b \psi_b' - \frac{\rho_p A_p h_b h_p}{4} (\ddot{u}_p + \ddot{u}_p) + \frac{E_p A_p h_b h_p}{4} (\bar{u}_p'' + \underline{u}_p'') \\
& - \frac{C_{11}^D I_p h_b}{2} (\bar{\phi}_p'' - \phi_p'') = Q
\end{aligned} \tag{3.15b}$$

$$\begin{aligned}
& K_1 \mu_b A_b (v_b' - \phi_b) - \frac{\rho_p A_p h_p}{2} (\ddot{u}_p - \ddot{u}_p) + \frac{E_p A_p h_p}{2} (\bar{u}_p'' - \underline{u}_p'') \\
& - C_{11}^D I_p (\bar{\phi}_p'' + \phi_p'') = V
\end{aligned} \tag{3.15c}$$

$$E_b I_b \phi_b' - \frac{E_p A_p h_b}{2} (\bar{u}_p' - \underline{u}_p') + \frac{E_p w_p h_b}{2} (\bar{d}_{31} \bar{v} - \underline{d}_{31} \underline{v}) = M \tag{3.15d}$$

$$\frac{E_p A_p h_b h_p}{4} (\bar{u}_p' + \underline{u}_p') - \frac{C_{11}^D I_p h_b}{2} (\bar{\phi}_p' - \phi_p') - \frac{E_p w_p h_b h_p}{4} (\bar{d}_{31} \bar{v} + \underline{d}_{31} \underline{v}) = 0 \tag{3.15e}$$

$$\frac{E_p A_p h_p}{2} (\bar{u}_p' - \underline{u}_p') - C_{11}^D I_p (\bar{\phi}_p' + \phi_p') - \frac{E_p w_p h_p}{2} (\bar{d}_{31} \bar{v} - \underline{d}_{31} \underline{v}) = 0 \tag{3.15f}$$

Where,  $\bar{d}_{31} = \bar{h}_{31} / (E_p B_{33}^S)$  and  $\underline{d}_{31} = \underline{h}_{31} / (E_p B_{33}^S)$ .

The voltage terms in Eq. (3.15a), (3.15d), (3.15e) and (3.15f) can be either known or unknown depending on whether each PZT wafer

plays a role of an actuator or a sensor. When the PZT wafer acts as an actuator, voltage  $v$  becomes known *a priori* because the driving voltage is prescribed on the PZT wafer by an external voltage source. Then, the terms associated with voltage in Eq. (3.15) are shifted to the right hand side and become fixed end forces and moment accordingly.

On the other hand, when the PZT wafer acts as a sensor, the voltage is unknown and an additional constraint is needed to solve the equations of motion. In general, the amount of current passing through the sensing PZT wafer is negligible because a data acquisition circuit connected to the PZT wafer has very large electric impedance. In this case, the total amount of free charge on the PZT wafer can be assumed to be zero [Ike90, Lim08]:

$$w_p h_p \int_0^L D dx = 0 \quad (3.16)$$

Substituting Eq. (3.13) into Eq. (3.16), voltages become a function of the axial displacements at both ends of the PZT wafers along the neutral axis:

$$\bar{v} = -\frac{h_p \bar{h}_{31}}{L} [\bar{u}_p(L) - \bar{u}_p(0)] \quad (3.17a)$$

$$\underline{v} = -\frac{h_p \underline{h}_{31}}{L} [\underline{u}_p(L) - \underline{u}_p(0)] \quad (3.17b)$$

Substituting Eq. (3.17) into Eq. (3.15), the force boundary conditions can be formulated when the PZT wafers act as sensors.



### 3.2 Spectral Element Formulation

After the equations of motion are obtained through Hamilton's principle, governing equations and force boundary conditions are represented with respect to the response variables of the base beam in the time domain as the Eq(3.14) and Eq(3.15). Next, the overall procedures for spectral element formulation of the CPBS are illustrated as Fig. 3.2. The stiffness element matrix and nodal force vector are obtained through the procedures in Fig. 3.2, and the nodal displacement vectors of the CPBS are calculated in the frequency domain [Par10].

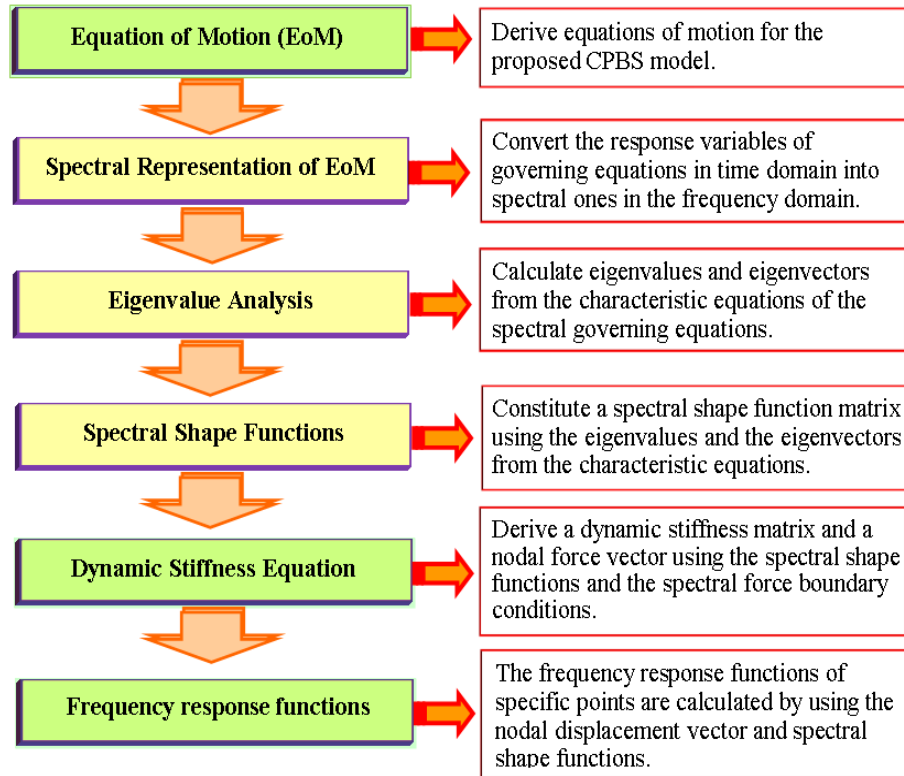


Fig. 3.2 Procedures for spectral element formulation [Lee00].

### 3.2.1. Spectral Representation of Response Variables

In Section 3.1, the governing equations in Eq. (3.14) and the force boundary conditions in Eq. (3.15) are represented as a function of the response variables of the base beam on the neutral axis. For spectral element formation of the CPBS, these governing equations and force boundary conditions should be transformed into the frequency domain. As the first step, the response variables defined on the neutral axis of the base beam are represented in spectral forms:

$$u_b(x, t) = \sum_n \hat{u}_n(x, \omega_n) e^{i\omega_n t} \quad (3.18a)$$

$$\psi_b(x, t) = \sum_n \hat{\psi}_n(x, \omega_n) e^{i\omega_n t} \quad (3.18b)$$

$$v_b(x, t) = \sum_n \hat{v}_n(x, \omega_n) e^{i\omega_n t} \quad (3.18c)$$

$$\phi_b(x, t) = \sum_n \hat{\phi}_n(x, \omega_n) e^{i\omega_n t} \quad (3.18d)$$

where  $\hat{u}$ ,  $\hat{\psi}$ ,  $\hat{v}$  and  $\hat{\phi}$  are the Fourier coefficients associated with response variables  $u_b$ ,  $\psi_b$ ,  $v_b$  and  $\phi_b$ , in the time domain at the  $n^{\text{th}}$  angular frequency  $\omega_n$ . The general solution forms of the Fourier coefficients in Eq. (3.18) are represented as follows:

$$\begin{aligned} \hat{u}_n &= u_0 e^{-ik(\omega_n)x}, & \hat{\psi}_n &= \psi_0 e^{-ik(\omega_n)x} \\ \hat{v}_n &= v_0 e^{-ik(\omega_n)x}, & \hat{\phi}_n &= \phi_0 e^{-ik(\omega_n)x} \end{aligned} \quad (3.19)$$

where  $k$  denotes a wave number corresponding to  $\omega_n$ , and  $u_0$ ,  $\psi_0$ ,  $v_0$  and  $\phi_0$  are the amplitudes of the Fourier coefficients in the spatial domain.

### 3.2.2 Characteristic Equations and a Shape Function Matrix for a Spectral Element

Substituting Eq. (3.4) and (3.18) into Eq. (3.14), The governing equations in Eq. (3.14) are expressed with respect to  $u_0$ ,  $\psi_0$ ,  $v_0$  and  $\phi_0$ :

$$\mathbf{C}\mathbf{u}_0 = \mathbf{0} \quad (3.20)$$

where  $\mathbf{u}_0 = (u_0, \psi_0, v_0, \phi_0)^T$  and each component in matrix  $\mathbf{C}$  is presented in Appendix (A1). Note that all components coupled between  $u_0$ ,  $\psi_0$  and  $v_0$ ,  $\phi_0$  in  $\mathbf{C}$  are zeros for the CPBS with collocated PZT wafers in Appendix (A1). From a mechanical point of view, this is because the neutral axis of the CPBS is identical to that of the base beam. For the CPBS with a single PZT wafer, the neutral axis of the CPBS does not coincide with that of the base beam and the aforementioned coupled components in  $\mathbf{C}$  have non-zero values.

For the CPBS with a single PZT wafer, the characteristic equation of Eq. (3.20) is  $\det[c_{ij}] = 0$  ( $1 \leq i, j \leq 4$ ) so that  $u_0$ ,  $\psi_0$ ,  $v_0$  and  $\phi_0$  are non-zeros. In case of the CPBS with collocated PZT wafers, two independent characteristic equations are derived using the partitioned sub-matrices of  $\mathbf{C}$  in Appendix (A1) because  $u_0$  and  $\psi_0$  are independent of  $v_0$  and  $\phi_0$  in Eq. (3.20). One is  $\det[c_{ij}] = 0$  ( $1 \leq i, j \leq 2$ ) so that  $u_0$ ,  $\psi_0$  have non-zero values in Eq. (3.20). The other is  $\det[c_{ij}] = 0$  ( $3 \leq i, j \leq 4$ ) so that  $v_0$ ,  $\phi_0$  are non-trivial solutions.

The above characteristic equations result in high-order polynomial equations with respect to  $k$ , and they consist of only even order terms of  $k$ . Because no closed form solution exists for these high-order

polynomial equations, the companion matrix method is employed to numerically calculate the roots of the characteristic equations [Cha05]. Once all roots of the characteristic equation are obtained, the corresponding eigenvectors in Eq. (3.20) are calculated for each root  $k$ .

Substituting the roots  $k$ 's and the corresponding eigenvectors into Eq. (3.19), the Fourier coefficients in Eq. (3.18) are expressed as:

$$\begin{aligned}\hat{u}_n &= \Phi_{\hat{u}}(x)\mathbf{A} \\ \hat{\psi}_n &= \Phi_{\hat{\psi}}(x)\mathbf{A} \\ \hat{v}_n &= \Phi_{\hat{v}}(x)\mathbf{A} \\ \hat{\phi}_n &= \Phi_{\hat{\phi}}(x)\mathbf{A}\end{aligned}\tag{3.21}$$

where  $\Phi_{\hat{u}}(x)$ ,  $\Phi_{\hat{\psi}}(x)$ ,  $\Phi_{\hat{v}}(x)$ ,  $\Phi_{\hat{\phi}}(x)$  and  $\mathbf{A}$  denote spatial shape function vectors for  $\hat{u}_n$ ,  $\hat{\psi}_n$ ,  $\hat{v}_n$ ,  $\hat{\phi}_n$  and an unknown coefficient vector, respectively. The components of the unknown coefficient vector  $\mathbf{A}$  are determined by force boundary conditions.

Fig. 3.1 illustrates a two node spectral element for the CPBS. The displacement vector and the force vector consist of the nodal response variables and the nodal forces, respectively, in the frequency domain. By applying Eq. (3.21) to the both ends of the beam, the following equation, which relates the nodal displacements into the unknown coefficient vector  $\mathbf{A}$  in Eq. (3.21), is obtained:

$$\mathbf{d} \equiv \{\hat{u}(0), \hat{\psi}(0), \hat{v}(0), \hat{\phi}(0), \hat{u}(L), \hat{\psi}(L), \hat{v}(L), \hat{\phi}(L)\}^T = \mathbf{H}(\omega)\mathbf{A}\tag{3.22}$$

where  $\mathbf{d}$ ,  $\mathbf{H}(\omega)$  and  $\mathbf{A}$  are the displacement vector, the shape function matrix and the coefficient vector of the two node spectral element. Each component in  $\mathbf{H}(\omega)$  and  $\mathbf{A}$  is expressed in Appendix (A2).

Substituting Eq. (3.22) into Eq. (3.15), the nodal forces of the two node spectral element in Fig. 3.1 are obtained by applying Eq. (3.15) at the both ends of the beam:

$$\mathbf{F} = \mathbf{G}(\omega)\mathbf{A} - \mathbf{F}_0 \quad (3.23)$$

Where,  $\mathbf{F}$ ,  $\mathbf{F}_0$  and  $\mathbf{G}(\omega)$  are the nodal force vector, the fixed force vector induced by electric voltages on PZT wafers and the force boundary condition matrix. Each component of  $\mathbf{F}$  and  $\mathbf{F}_0$  is expressed in Appendix (A3). Note that the fixed force vector  $\mathbf{F}_0$  changes depending on the functionality of the PZT wafer [Lim08]. By the same token, the constraint matrix  $\mathbf{G}(\omega)$  in Eq. (3.23) varies depending on the role of the PZT wafer, and each component of  $\mathbf{G}(\omega)$  is provided in Appendix (A4). If one of the PZT wafers act as a sensor and the other act as an actuator, each individual components of  $\mathbf{F}_0$  and  $\mathbf{G}(\omega)$  in Eq. (3.23) can be obtained similar to those in Appendix (A4) but is not presented here due to space limitation.

### 3.2.3. Dynamic Stiffness Matrix and Admittance

Because  $\mathbf{H}(\omega)$  in Eq. (3.22) is not a square matrix with the size of  $8 \times m$  ( $m > 8$ ), a stiffness matrix relating the nodal displacement vector to the nodal force vector cannot be derived by directly substituting Eq. (3.22) into Eq. (3.23). To tackle this issue, a condensation technique is

employed. First,  $\mathbf{F}_v$  is moved to the left hand side of Eq. (3.23), and the vector in the left hand side is simply divided into two subvectors as follows:

$$[\boldsymbol{\phi}_1 \ \boldsymbol{\phi}_2]^T \equiv \mathbf{F} + \mathbf{F}_v = \mathbf{G}(\omega)\mathbf{A} \quad (3.24)$$

where  $\boldsymbol{\phi}_1$  and  $\boldsymbol{\phi}_2$  are  $8 \times 1$  and  $(m-8) \times 1$  column vectors, respectively. Similarly, the coefficient vector  $\mathbf{A}$  is divided into two subvectors:

$$\mathbf{A} = [\boldsymbol{\alpha}_1 \ \boldsymbol{\alpha}_2]^T \quad (3.25)$$

where  $\boldsymbol{\alpha}_1 \equiv (a_1, a_2, \dots, a_8)^T$ ,  $\boldsymbol{\alpha}_2 \equiv (a_9, \dots, a_m)^T$ .

Using Eqs. (3.22) and (3.25), the following equation is derived as:

$$\begin{pmatrix} \mathbf{d} \\ \boldsymbol{\alpha}_2 \end{pmatrix} = \tilde{\mathbf{H}}(\omega)\mathbf{A} \quad (3.26)$$

where

$$\tilde{\mathbf{H}}(\omega) = \begin{bmatrix} \mathbf{H}(\omega) \\ \mathbf{0}_{(m-8) \times 8} \ \mathbf{I}_{(m-8) \times (m-8)} \end{bmatrix} \quad (3.27)$$

where  $\mathbf{0}$  and  $\mathbf{I}$  denote  $(m-8) \times 8$  zero matrix and  $(m-8) \times (m-8)$  identity matrix, respectively.

Substituting Eq. (3.26) into Eq. (3.24), Eq. (3.24) is expressed as the following equation:

$$\begin{pmatrix} \boldsymbol{\phi}_1 \\ \boldsymbol{\phi}_2 \end{pmatrix} = \tilde{\mathbf{K}}(\omega) \begin{pmatrix} \mathbf{d} \\ \boldsymbol{\alpha}_2 \end{pmatrix} \quad (3.28)$$

Where,  $\tilde{\mathbf{K}}(\omega) \equiv \mathbf{G}(\omega)\tilde{\mathbf{H}}^{-1}(\omega)$ , and it can be further divided in to four sub-matrices depending on their correspondence to  $\mathbf{d}$  and  $\boldsymbol{\alpha}_2$ :

$$\begin{pmatrix} \phi_1 \\ \phi_2 \end{pmatrix} = \begin{bmatrix} \tilde{\mathbf{K}}_{dd}(\omega) & \tilde{\mathbf{K}}_{d\alpha}(\omega) \\ \tilde{\mathbf{K}}_{\alpha d}(\omega) & \tilde{\mathbf{K}}_{\alpha\alpha}(\omega) \end{bmatrix} \begin{pmatrix} \mathbf{d} \\ \boldsymbol{\alpha}_2 \end{pmatrix} \quad (3.29)$$

Sorting out Eq. (3.29) with respect to  $\mathbf{d}$ , the direct stiffness matrix  $\mathbf{S}(\omega)$  of the CPBS for spectral analysis is derived as:

$$\mathbf{S}(\omega)\mathbf{d} = \mathbf{f} \quad (3.30)$$

Where,  $\mathbf{S}(\omega) \equiv \tilde{\mathbf{K}}_{dd} - \tilde{\mathbf{K}}_{d\alpha} \tilde{\mathbf{K}}_{\alpha\alpha}^{-1} \tilde{\mathbf{K}}_{\alpha d}$  and  $\mathbf{f} \equiv \phi_1 - \tilde{\mathbf{K}}_{d\alpha} \tilde{\mathbf{K}}_{\alpha\alpha}^{-1} \phi_2$ .

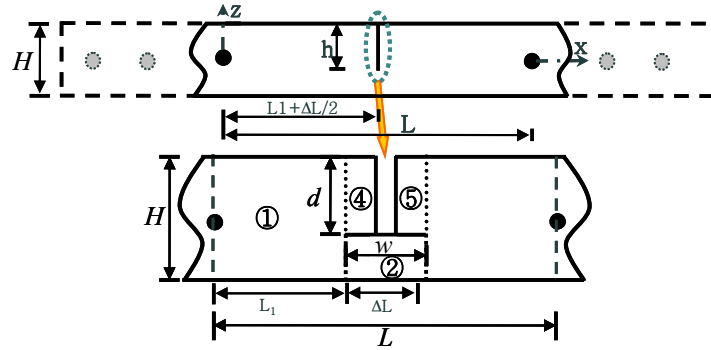
Using the result of Eq. (3.30), the EM admittance ( $Y$ ) on the PZT wafer is derived as :

$$Y(\omega) = I(\omega) / V(\omega) = i\omega \{ h_{31} [u_p(l) - u_p(0)] + l / h_p \} / B_{33}^S \quad (3.31)$$

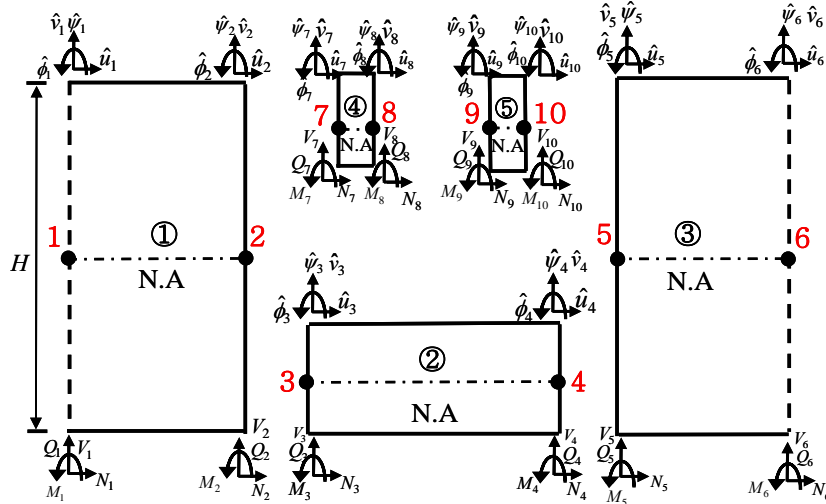
where  $\omega$ ,  $I$ ,  $V$ ,  $h_{31}$ ,  $u_p$ ,  $l$ ,  $h_p$  and  $B_{33}^S$  denote the angular frequency, current, voltage, the piezoelectric constant of the PZT wafer, horizontal displacement on the neutral axis, the length of the PZT, the thickness of the PZT wafer and the dielectric constant the superscript  $S$  on  $B_{33}^S$  indicate that the corresponding constants are measured under zero strain.

### 3.3 Damage Spectral Element

Configuration of the spectral element with transverse crack and the element-internal discretization are shown in Fig. 3.3



(a) The configuration of spectral element with transverse crack



(b) Internal discretization of notch element through the five-sublaminae.

Fig. 3.3 Schematic model of the transverse crack configuration.

If the damage such as crack does not occurs in the plate-like structure, the arbitrary spectral element (2-node element) as shown Fig. 3.3(a) is the same as the single beam element (the Fig. 3.1(a)) that is able to capture the exact dynamics of the flexure and shear. When the transverse crack is considered as Fig. 3.3(a), it requires explicit



definition by three additional parameters. These three parameters are (1) the half element length of the transverse crack ( $x = L/2$  as shown in Fig. 3.3(a) and  $L$  is imposed in terms of the smallest group wavelength), (2) the depth of the crack ( $d$ ), (3) the thickness of the bottom crack-tip ( $z = H - d$ ,  $H$  is total element depth). We assume that the transverse crack is a through-width crack (along the  $y$  direction) which allows the modeling to be accomplished using one-dimensional waveguides. The element-internal discretization as shown in Fig. 3.3(b) produces five-internal waveguides numbered ① to ⑤. For all these elements, a point nodes of total ten will appear in the formulation, and the dofs associated with them will be condensed out systematically. As a result, a simple two-node notch element can be used to model the transverse crack, where faster and repeated analysis with acceptable accuracy will be of prime importance for damage identification studies and various SHM applications in conjunction with a wave-based diagnostic signal. Since the main objective behind using such a model is to improve upon the various available approximate models based on equivalent flexibility, empirical crack-functions etc., it is essential to use the element-internal discretization technique [Gop07].

### 3. 4 Experimental and Numerical Analysis Studies

In this subsection, verification of proposed spectral element analysis with a coupled PZT and beam system (CPBS) is investigated through

two case studies about admittance and displacement. The PZT wafers of PSI-5A4E type [Pie09] are rigidly bonded on a base beam. Also, their length and thickness are 10mm and 0.507mm, respectively. The PZT wafers are assumed to be short-circuited. The base beam (198mm  $\times$  3mm) is made of aluminum that the elastic modulus and Poisson ratio are 70GPa and 0.33, respectively. The length between fix end and PZT is using the 53mm because the actual length is considered a reduced length of 2mm by welding at the fix end. Also, the sensing circuit as shown in Fig. 2.7 is used to measure the output Voltage for computing admittance or impedance signal. The structural damping of base beam is assumed to be 0.5%.

Because the analytic solution of this example is unavailable, the a two dimensional finite element method (2-D FEM) or a three dimensional finite element method (3-D FEM) will be performed to obtain an asymptotical reference solution through the Steady-state Dynamic Analysis, Direct of ABAQUS 6.7-4 on IBM p595 at KISTI Supercomputing Center [KIS03].

#### **3.4.1 Case I : Admittance Comparison of Intact Model with Single PZT**

In this example, the EM admittance of a PZT wafer bonded on a cantilever beam is computed a frequency range of up to 30kHz. As shown in Fig. 3.4, the cantilever beam with a surface-bonded PZT wafer is forced to be in steady-state motion by exerting the harmonic driving voltage signal with amplitude of  $\pm 1$  volt on the PZT wafer.

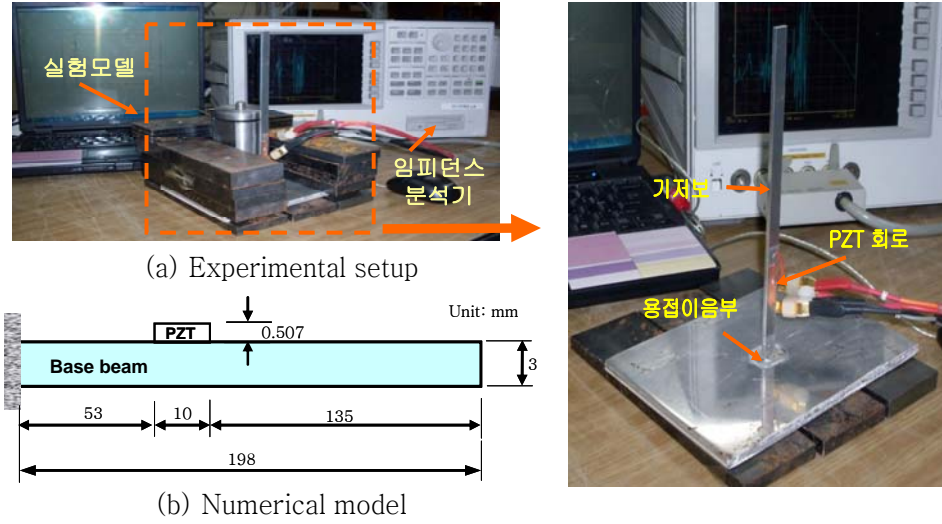


Fig. 3.4 Experimental and numerical models for the EM admittance of a PZT wafer bonded on a cantilever beam

For discretizing the model in Fig. 3.4, two single beam spectral elements and one CPBS spectral element with a single PZT wafer are used in the proposed method. In the 2D FE analysis, 10 8-node quadratic plane stress PZT elements (size:  $0.5\text{mm} \times 0.508\text{mm}$  per each element) and 594 8-node quadratic plane stress solid elements (size:  $1.0\text{mm} \times 1.0\text{mm}$  per each element) are employed for discretizing the PZT wafer and the base beam, respectively. 100 8-node quadratic plane stress PZT elements (size:  $0.5\text{mm} \times 0.508\text{mm}$  per each element) and 5940 8-node quadratic plane stress solid elements (size:  $1.0\text{mm} \times 1.0\text{mm}$  per each element) are used in the 3D FE analysis.

In the experiment for EM admittance of PZT, impedance analyzer (HP 4294A) is measured a frequency range of 1kHz to 30kHz by 32Hz frequency resolution.

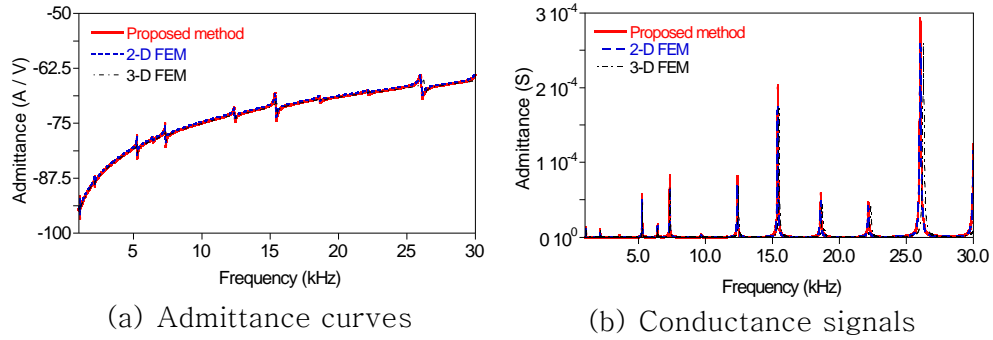


Fig. 3.5 Comparison of resonance frequencies between proposed method and FEM

Fig. 3.5 represents the comparison of resonance frequencies in the EM admittance through the numerical analysis. In Fig. 3.5(a), EM admittance curves from proposed method, 2-D FEM and 3-D FEM could be obtained when a harmonic voltage input with the amplitude of  $\pm 1$  volt is exerted on the top of PZT in Fig 3.4(b). The conductance of Fig. 3.5(b) is the real part without the effect of the free current in Fig. 3.5(a) in order to more detailed comparison like as the location and size of the resonance peaks. The proposed method compared with the FEM show that the location of resonance frequency is well predicted in the 0kHz to 30kHz.

The axis on the right hand side of the Fig. 3.6 indicates the resonance frequency obtained from 3-D FEM, and the one on the left represents the relative errors between the resonance frequencies computed from the proposed method and 3-D FEM, 2-D and 3-D FEM. The proposed method produces very accurate resonance frequencies within  $\pm 2.0\%$  Maximum error level compared to those from 3-D FEM. The first 25 lowest resonance frequencies in the 0kHz to 60kHz are extracted by picking up the peaks of the admittance.

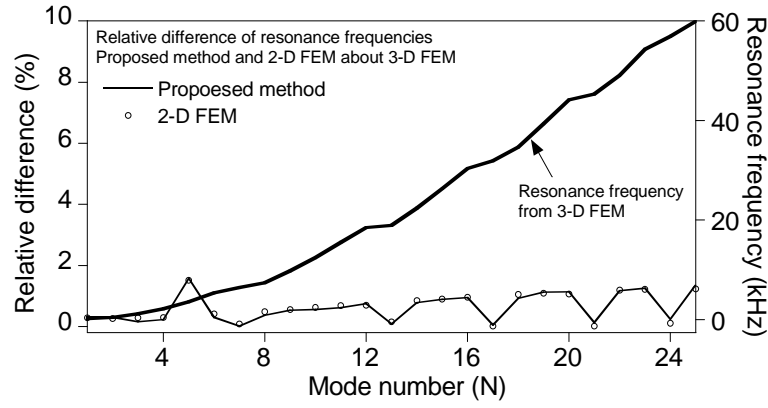


Fig. 3.6 Relative difference of resonance frequencies between Proposed method and FEM up to the 25<sup>th</sup> mode

On the other hand, the resonance frequencies from 2-D FEM are similar to proposed method. Therefore, the trend of relative errors between the resonance frequencies computed from the 2-D FEM and 3-D FEM is almost the same.

Similar to Fig. 3.5, the comparison of resonance frequencies in the EM admittance through experiment and proposed method is shown in Fig. 3.7

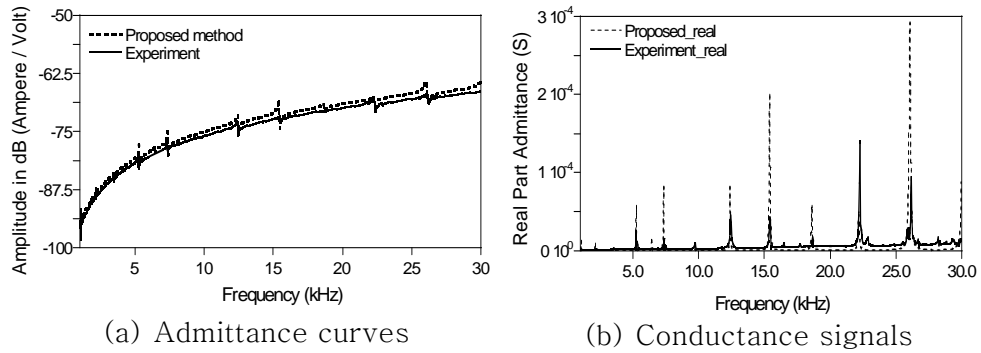


Fig. 3.7 Comparison of the EM admittance from proposed method and experiment

When a harmonic voltage input with the amplitude of  $\pm 1$  volt is exerted on the PZT of the experimental model, impedance analyzer is measuring a current signal on the bottom of PZT and the EM admittance of the PZT wafer from measured current can be calculated. Because the damping of the base beam element is not given correctly and the frequency resolution used for data acquisition is relatively low in the case of experiment, the difference peak value of the each resonance modes has occurred. It is noticeable that the resonance frequency of representative dynamic characteristic is well predicted.

### 3.4.2 Case II: Comparison of Mode Shape and Displacement FRF of Intact Model with Single PZT

In this section, the three numerical methods and a laser scanning vibrometer are used to obtain the overall dynamic responses of the structure such as resonance frequencies, mode shapes, and frequency response functions (FRF). These dynamic responses from the laser scanning vibrometer are compared to those computed by the spectral element (SE) analysis which is proposed method using the CPBS.

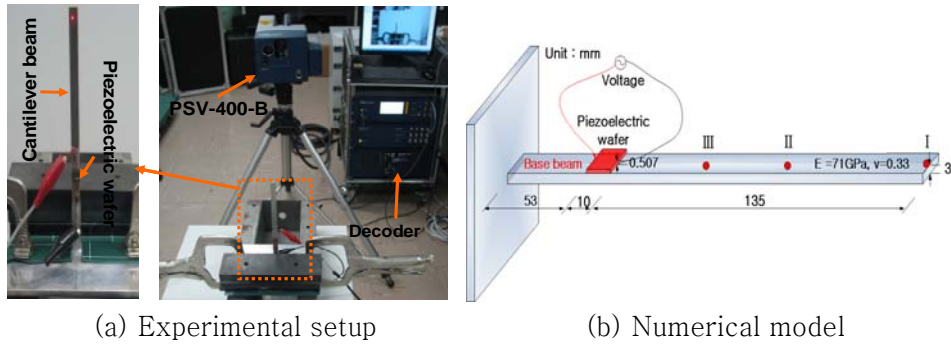


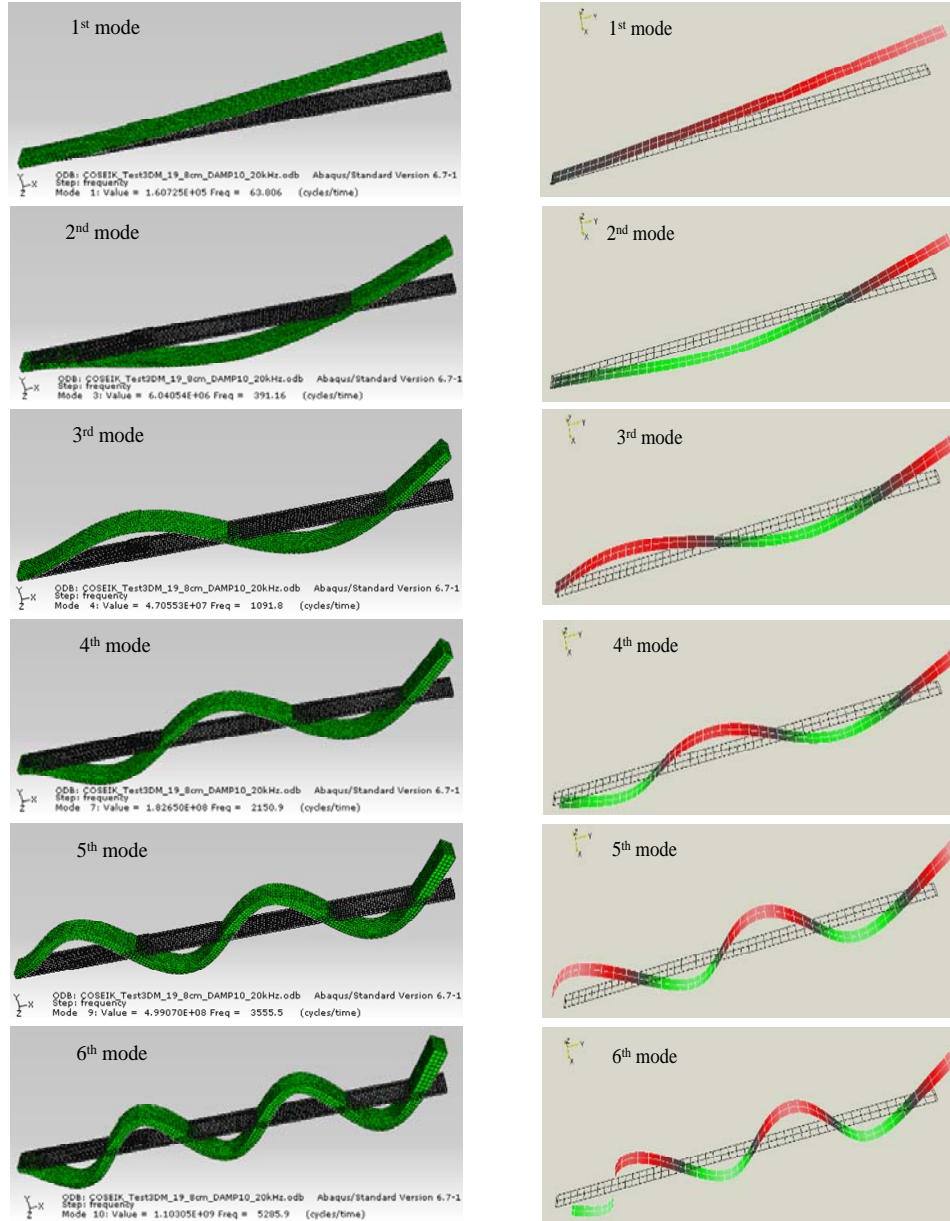
Fig. 3.8 An experimental setup and a numerical model for FRF.

Also, 2-D and 3-D FEM are conducted to obtain the asymptotic solutions for the comparison purpose.

Fig. 3.8 presents a numerical and experimental model to verify the proposed method. The plane stress condition is employed for discretizing the PZT wafer and the base beam in the proposed method and 2-D FEM. Note that, the plane stress solid element of the 3-D FEM is used for the comparison of the mode shape. The laser scanning vibrometer (PSV-400-B or PSV) of Polytec GMBH Co. in Germany in order to measure the dynamic response in high frequency range is a non-contact equipment as shown Fig. 3.8(a). PSV is able to measure the velocity and location of specific vibration points until the precision of nanometer resolution. In this study, frequency resolution of the PSV is 3.125Hz in the range up to 20kHs. Behavior of the entire mode was identified as the mode shape and frequency response function of the vertical displacement induced by harmonic excitation with the amplitude of 1V are obtained at the three points ( I , II , III point) in Fig. 3.8(b).

In Fig. 3.10, the mode shape corresponding to resonance frequency is shown through the 3-D FEM and experiment. The left side means that 11-mode shapes of bending deformation dominant are computed from 3-D FEM. The mode shape of the right side can be obtained by PSV. It seems that Little difference between the mode shape by the 3-D FEM and PSV exists as increasing high-order mode at the fixed end of the base beam because the scanning of the PSV begin with 1.3cm spot depart from fix end. However, if each mode compares the only

scanned region, they can be found the overall good agreement. More detail analysis of the mode shape deals in Fig. 3.11.





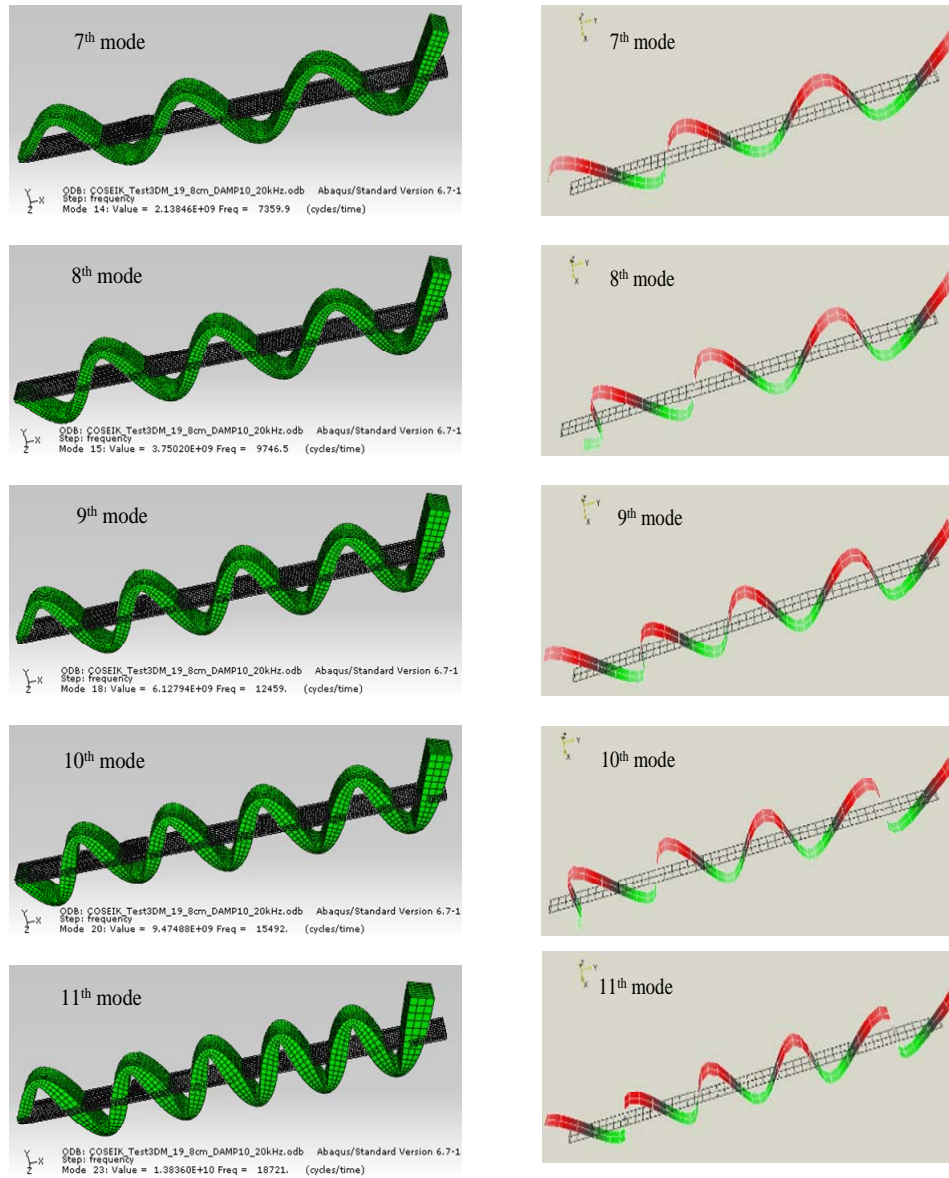


Fig. 3.9 Perspective view of mode shapes from 3-D FEM (left side) and PSV (right side).

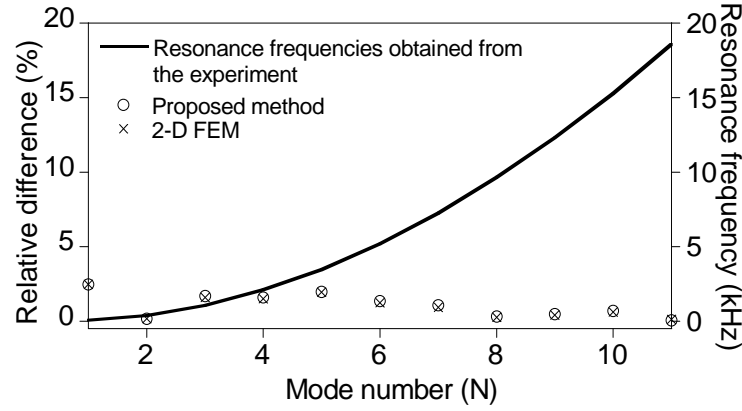
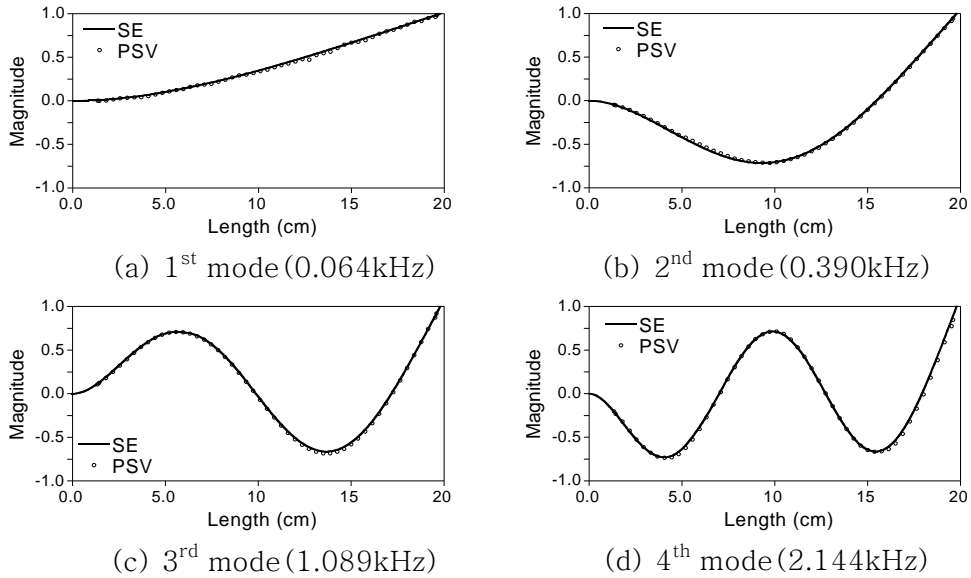


Fig. 3.10 Relative difference of the resonance frequencies between the numerical analyses [Proposed method, 2-D FEM] and experiment test [PSV] up to the 11<sup>th</sup> bending-dominant mode.

Fig. 3.10 shows the relative difference between the resonance frequencies obtained from the numerical methods and experiment. Here, the numerical methods include the proposed method and 2-D FEM. Through three methods, the FRFs of the vertical displacements at the free end of the base beam are computed. Then, the 1<sup>th</sup> to 11<sup>th</sup> resonance frequencies are extracted by picking up the peaks of the FRFs. The axis on the right hand side of Fig. 3.10 indicates the resonance frequency obtained from experiment, and the one on the left represents the relative errors between the resonance frequencies computed from the proposed method and experiment, 2-D FEM and experiment. The proposed method produces very accurate resonance frequencies within  $\pm 2.5\%$  error level compared to those from experiment through the PSV.

For the quantitative comparison of resonant mode shapes more than Fig. 3.9, the Fig. 3.11 illustrates that the resonance mode shapes

are extracted along the neutral axis of the top surface on the base beam. In the proposed method using spectral element (SE), the displacement for the mode shape is extracted by discretized 198-points of 1mm interval on the base beam. Mode shape of arbitrary mode can be obtained after each displacement values of the 198-points are normalized by the maximum value of the steady-state displacement. In the case of PSV, the 51-points along the centerline is used to measure a displacement in the middle of 153-points which measure the mode shapes as shown Fig. 3.9 on the top surface of the base beam. These displacements at the location of 51-points are equal to normalize as like the proposed method. As a consequence, the 6-mode shapes of the lowest mode are practically identical. Although A little difference between mode shape through the proposed method and experiment is shown at the fixed end area toward a higher mode than the 7<sup>th</sup>, the proposed method predicts the overall mode shape of the higher-order.



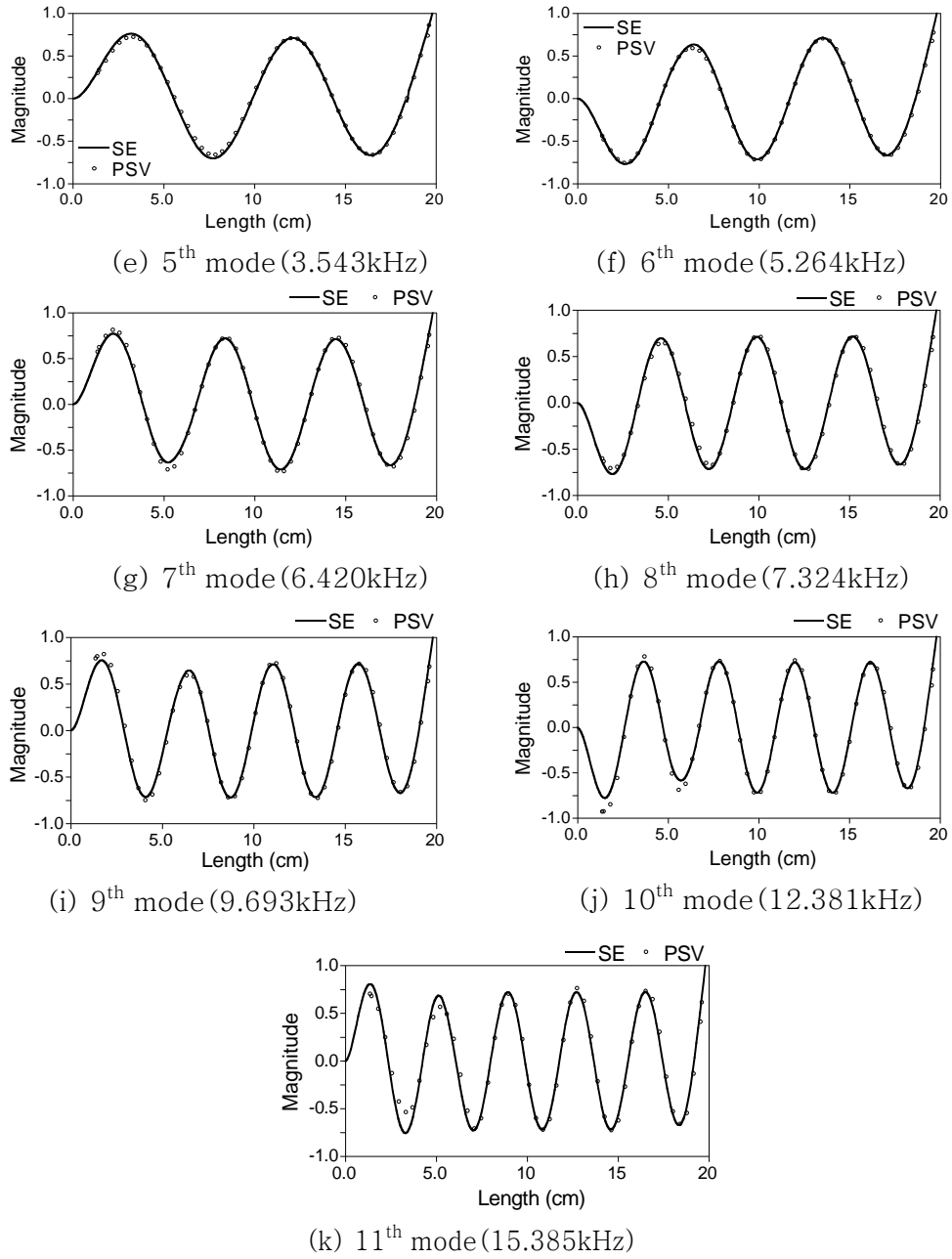
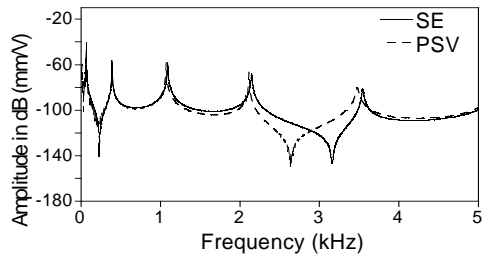


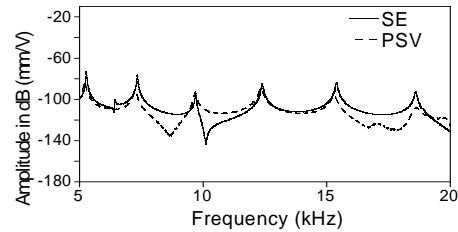
Fig. 3.11 Quantitative comparison of resonant mode shapes from Proposed method (or SE) and PSV.

Fig. 3.12 compares the FRFs obtained from the proposed method and PSV at the marked points (I, II, III point) in Fig. 3.8(b). As described above, the FRFs in Fig. 3.12 are the displacements response associated with only vertical displacement induced by harmonic excitation. The marked points as I, II, III point mean the right free end spot, 1/3 spot, middle spot of the base beam. For the increase the readability of the figure, the FRFs of three spots divided by 0~5kHz band and 5~20kHz band as illustrated in Fig. 3.12.

In the low frequency range of less than 4<sup>th</sup> resonance mode, the FRFs obtained from the proposed method using spectral element (SE) and PSV produce relatively identical as shown Figs. 3.12(a), (c), (e). Especially, note that the FRFs of the proposed method are the result of using only 3-spectral elements. In the high frequency range of more than 5<sup>th</sup> resonance mode, the compared FRF shape is very similar at the vicinity of the resonance points on the FRFs in Figs. 3.12(b), (d), (f). On the other hand, little difference of shapes between the FRFs obtained from the proposed method and PSV exist at the near anti-resonance points.



(a) 0–5kHz (point I)



(b) 5–20kHz (point I)

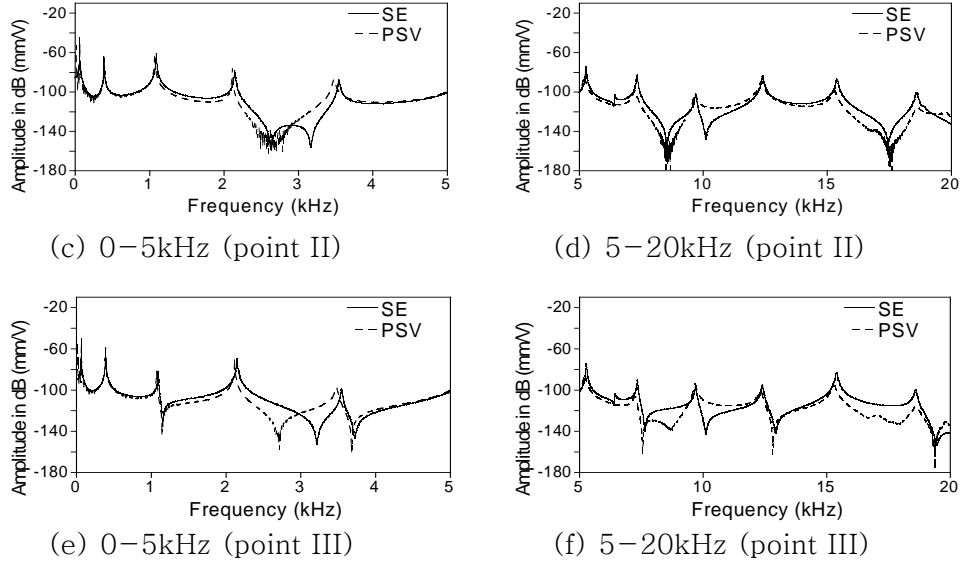


Fig. 3.12 Comparison of frequency response functions corresponding to vertical displacement from Proposed method (or SE) and PSV at three points depicted as I, II, and III in Fig. 3.8.

Fig. 3.13(a) illustrates the correlation between FRF and mode shape in the lightly damped system just as experimental model. After maximum FRF peak values are obtained through proposed method and PSV at the points I, II, III on the base beam in Fig. 3.8(b), the maximum FRF peak values at the points II, III are normalized with respect to point I just as Fig. 3.13. Although the difference of response function value occurs in the high frequency range of more than 5<sup>th</sup> resonance mode as shown in Fig. 3.13, the mode shape ratio on the same mode which is extracted from the result of the proposed method and PSV is nearly equal as illustrated the Fig. 3.13(b).

In the view of the mode analysis, the FRF results of the proposed method shows consistent results compared with experiment in the interesting frequency range.

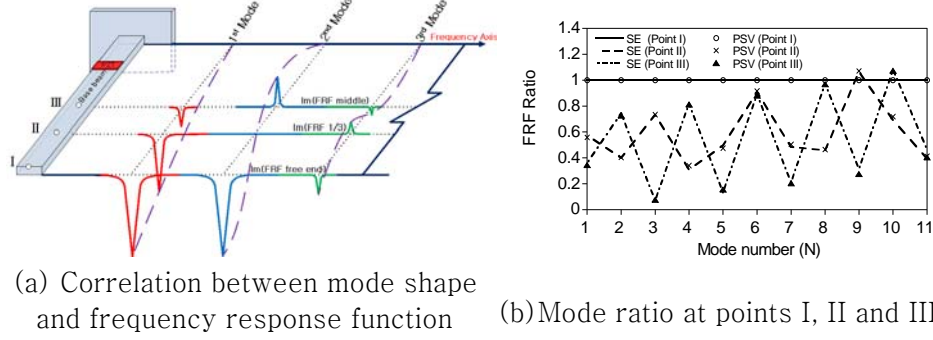


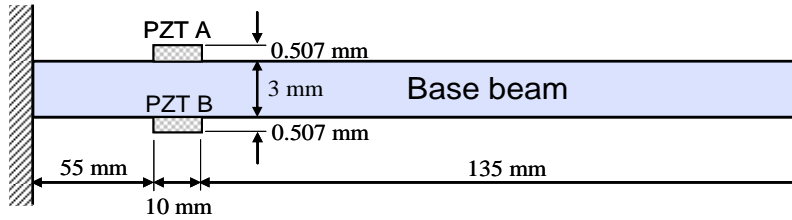
Fig. 3.13 Comparison of mode ratio and frequency response functions ratio from SE and PSV at points I, II and III in Fig. 3.8.

### 3.4.3 Case III: Electro-Mechanical (EM) Signal Comparison of Intact Model with Collocated PZT

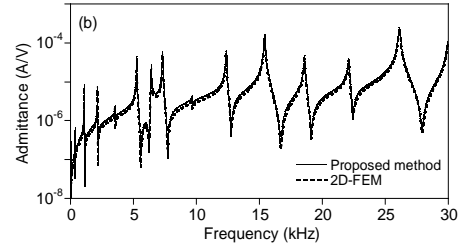
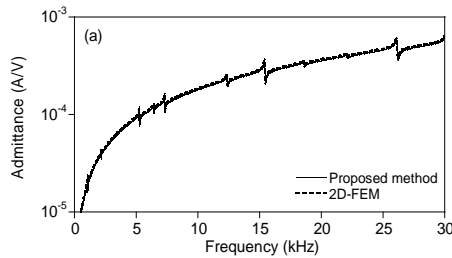
In the third example, additional verification analysis for the proposed method was performed. The EM admittance of collocated PZT wafers bonded on a cantilever beam is computed in a frequency range of up to 30kHz. As shown in Fig. 3.14, the collocated PZT wafers bonded on the top and bottom of a base beam are denoted as PZTs A and B, respectively.

2-D FEM with a refined mesh size is used to obtain a reference solution for the comparison purpose. Two single beam spectral elements and one spectral element for the CPBS with collocated PZT wafers are used for this example. Fig. 3.14 illustrates the EM admittance curves of the collocated PZT wafers when a harmonic

voltage input with the amplitude of  $\pm 1$  volt is exerted on the top of PZT A while PZT B is short-circuited in Fig. 3.14(a). In this case, the current obtained at the bottom of each PZT wafer becomes the EM admittance of the PZT wafer. The structural damping of the base beam is assumed to be 0.5% and the frequency resolution is 1Hz. In Fig. 3.14(b), the free current, which is induced by input voltages on PZT A, is dominant in the EM admittance of PZT A. The EM admittance of PZT B clearly represents the modal characteristics of the CPBS without the effect of the free current in Fig. 3.14(c). In both figures, the peaks in the EM admittance curves indicate the resonance frequencies of the cantilever beam with collocated PZT wafers. The EM admittance curves from the proposed method are practically identical to those from 2-D FEM.



(a) A cantilever beam with collocated PZT wafers



(b) EM admittance of collocated PZT wafers in test model: (a) PZT A (c) EM admittance of collocated PZT wafers in test model: (b) PZT B  
Fig. 3.14 Comparison of admittance corresponding to the location of sensing PZT from proposed method (SE) and 2-D FE.



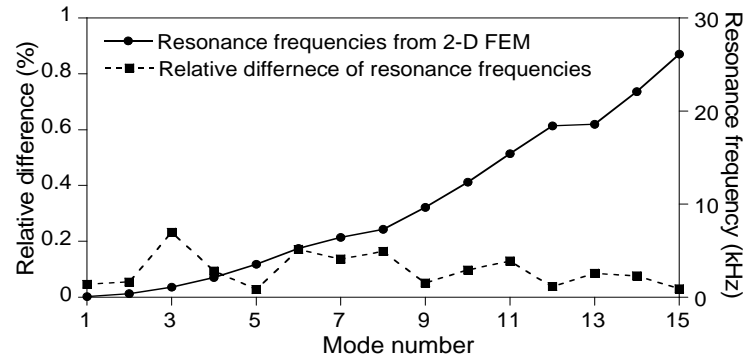


Fig. 3.15 Relative differences between the resonance frequencies computed from proposed method and 2-D FEM up to the 15<sup>th</sup> mode.

Fig. 3.15 shows the relative differences between the resonance frequencies obtained from the proposed method and 2-D FEM up to the 15<sup>th</sup> mode. The proposed method yields very accurate resonance frequencies within  $\pm 0.23\%$  error level compared to those from 2-D FEM. Fig. 3.16 presents the frequency change which is calculated by subtracting the frequency of the cantilever beam with a single PZT wafer from that with collocated PZT wafers at each resonance mode. The frequency change is normalized with respect to the frequency for the cantilever beam with a single PZT wafer at each resonance mode.

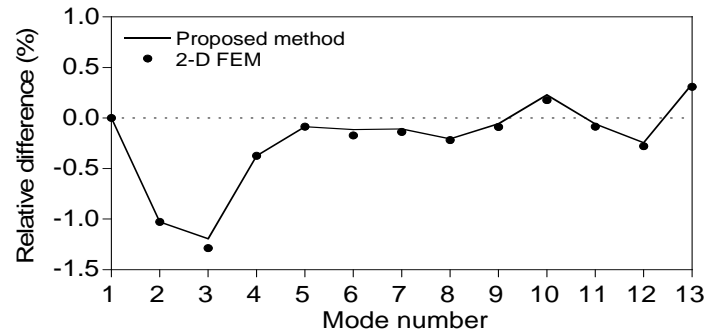


Fig. 3.16 Relative difference between the cantilever beam with a single

and collocated PZT wafers at each resonance mode. Note that the frequency change values are negative except the 10<sup>th</sup> and 13<sup>th</sup> modes though the base beam is stiffened by mounting another PZT wafer. This phenomenon implies that the increase in modal mass is larger than modal stiffness increase except the 10<sup>th</sup> and 13<sup>th</sup> modes when the CPBS with a single PZT becomes that with collocated ones. The proposed method predicts the trend in resonance frequency changes satisfactorily compared to 2-D FEM.

#### 3.4.4 Case IV: Electro-Mechanical (EM) Signal Comparison of Notch Model with Collocated PZT

In this example, the EM signals are computed from the cantilever beam with a CPBS and notch spectral element which is formulated in subsection 3.3. The accuracy and the effectiveness of Proposed method with notch element are compared with those of 2-D FEM.

Two identical PZT wafers are collocated on the top and bottom surfaces of a damaged base beam, denoted by PZTs A and B, respectively. A notch (1mm×1mm) is introduced on the top surface of the base beam 34mm away from the collocated PZT wafers.

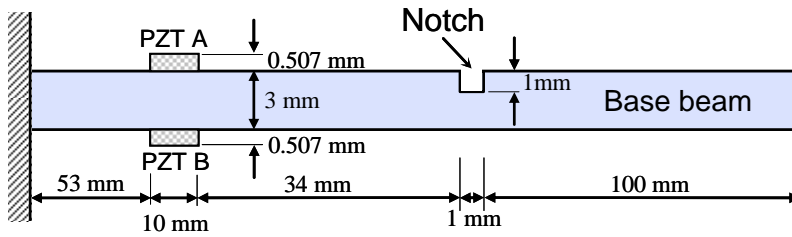


Fig. 3.17 A damaged model with collocated PZT wafers for measuring EM signals

A total of four elements (one notch, two single beam and one CPBS elements) in Fig. 3.17 are used for proposed method. Since the analytical solution is unavailable, an asymptotic reference solution is obtained by 2-D FEM with a sufficiently refined mesh layout. 20 8-node quadratic plane stress solid elements (1mm×0.507mm) and 593 8-node quadratic plane stress solid elements (1mm×1mm) are used for discretizing the PZT wafer and the base beam, respectively.

The harmonic input with the amplitude of  $\pm 1.0$  volt is applied on the top of PZTs A and B alternately, and the driving frequency is varied from 0 to 30 kHz. The frequency resolution is set to be 1Hz. Here, the EM signal represents the EM admittance which is defined as the ratio of the output current to the input voltage in the frequency domain. Figs. 3.18(a)–(c) compare the EM signals computed from proposed method to those from 2-D FEM. Several peaks in the EM signals indicate the resonance frequencies of the damaged cantilever beam. The EM signals calculated from proposed method are practically identical to those from 2-D FEM. Fig. 3.18(d) shows the relative differences between the resonance frequencies calculated from the proposed method and FE analyses up to the 57<sup>th</sup> mode. Proposed method yields very accurate resonance frequencies within  $\pm 0.5\%$  relative error compared to those from 2-D FEM. Proposed method is shown to produce satisfactory results with fewer elements comparable to 2-D FEM in which a huge number of elements are required. The computing

time per one frequency step taken in proposed method is 3.9 ms while that taken in 2-D FEM is 360 ms.

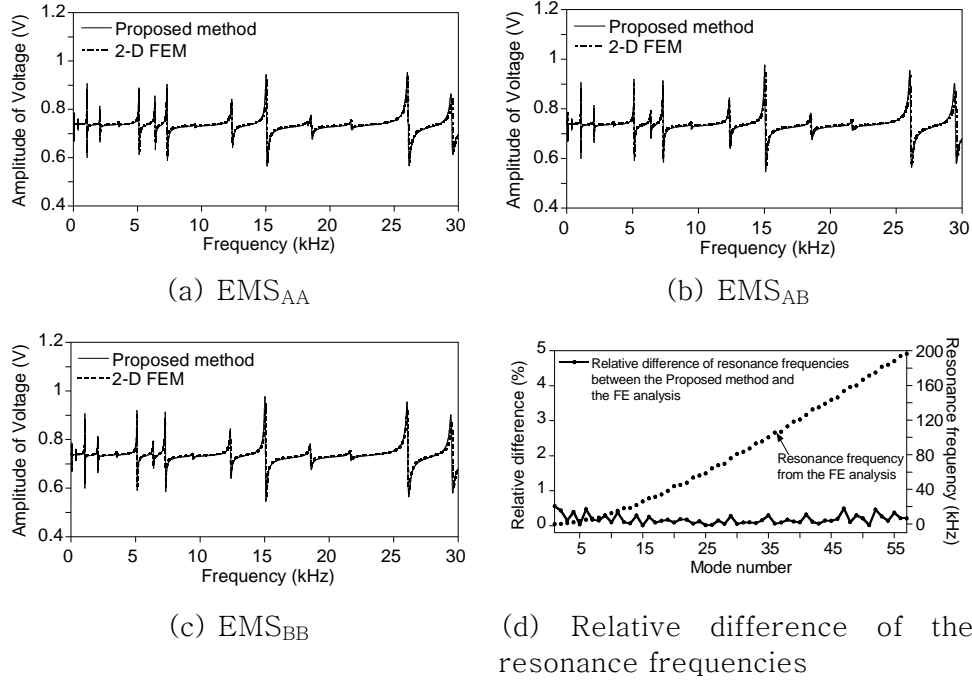
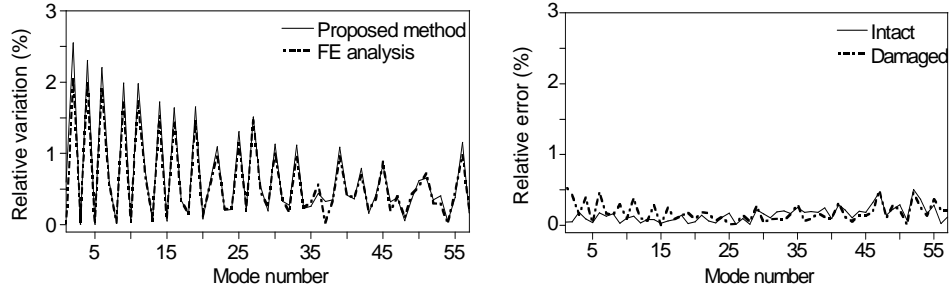


Fig. 3.18 Comparison of the EMS and the resonance frequencies computed from the proposed method and FE analyses of the damaged cantilever beam in Fig. 3.17.

Fig. 3.19(a) compares the relative difference between resonance frequencies of the damaged cantilever beam to those of the intact one. Although there is a slight deviation at the 37<sup>th</sup> mode, the proposed method successfully predicts the change of the resonance frequencies produced by the formation of the notch and validating the notch element employed in proposed method. Fig. 3.19(b) shows the relative errors between proposed method and FE analyses of the intact and

damaged conditions of the beam. The relative errors for the damaged case are slightly higher for several modes compared to the intact case.



(a) Relative differences between the resonance frequencies obtained from the damaged and intact conditions of the beam.

(b) Relative errors between the resonance frequencies obtained from proposed method and FE analyses

Fig. 3.19 Comparisons of the resonance frequencies obtained by proposed method and FE analyses of the intact and damaged conditions of the cantilever beam

However, the magnitude of the relative error remains below 0.5% up to 200kHz, which corresponds to the 57<sup>th</sup> mode.

Figs. 3.20(a)–(c) illustrate the EM signals corresponding to the LW mode signals in Figs. 2.7(c) and 2.7(d), respectively. Peaks in each EMS correspond to the resonant frequencies of the beam. Here,  $EMS_{AB}$  is always identical to  $EMS_{BA}$ , only  $EMS_{AB}$  is shown.

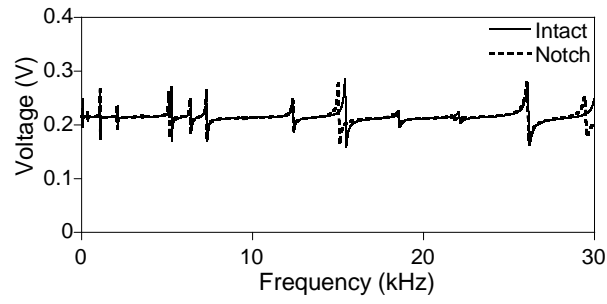
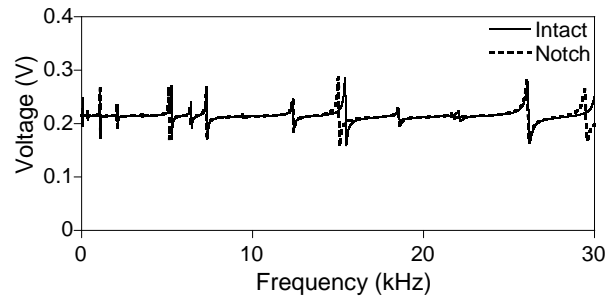
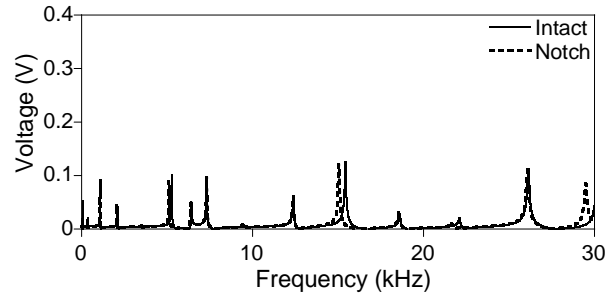
(a)  $EMS_{AA}$ (b)  $EMS_{BB}$ (c)  $EMS_{AB}$ 

Fig. 3.20. The EM signals obtained from collocated PZT wafers on the intact and the damaged cantilever beams in Fig 2.7. Here, the first and second subscripts of 'EMS' indicate the actuator and the sensor, respectively.

The decomposed EM signals corresponding to each LW mode are shown in Figs. 3.21(a)–(c). In case of the intact cantilever beam,

$EMS_{MC}$  is a null signal as shown in Fig. 3.21(c). On the contrary,  $EMS_{MC}$  clearly appear in Fig. 3.21(c) due to damage particularly in the vicinity of the resonant frequencies of the beam. Therefore, the existence of damage can be easily confirmed from  $EMS_{MC}$  without need for any prior baseline EM signal. Furthermore, because the appearance of  $EMS_{MC}$  is not affected by temperature variation, no cumbersome temperature compensation is necessary for damage identification.

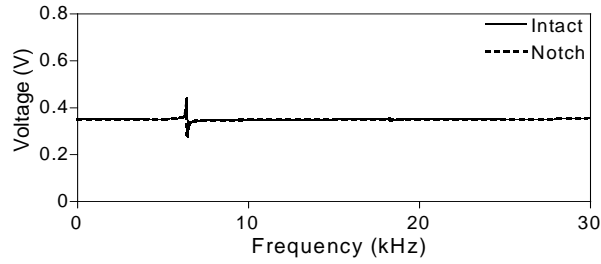
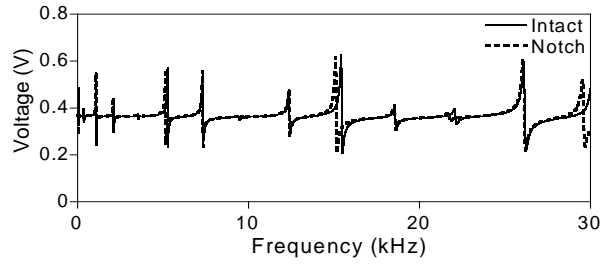
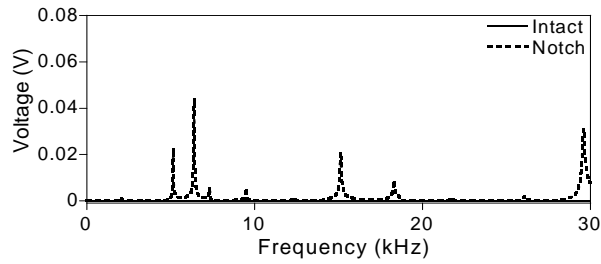
(a)  $EMS_{S0}$ (b)  $EMS_{A0}$ (c)  $EMS_{MC}$ 

Fig. 3.21. Decomposed EM signals through the application of Eq.

(2.8) to the EM signals from intact and damaged states in Fig 3.20.

### 3.4.5 Case V: Comparison of proposed SE and Lee' s SE Analysis.

In this final example, comparing the FRFs obtained from the proposed method and Lee' s method.

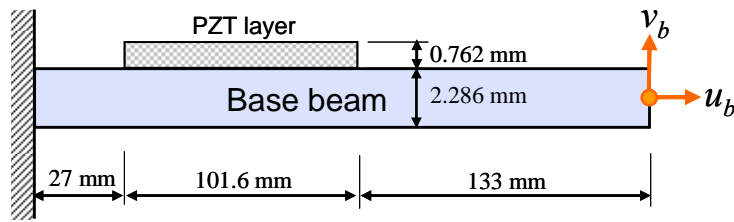
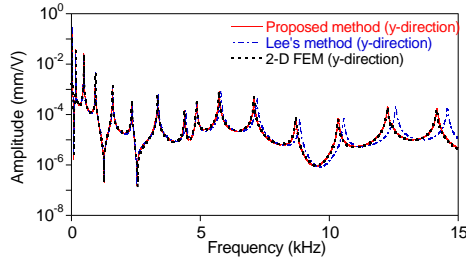


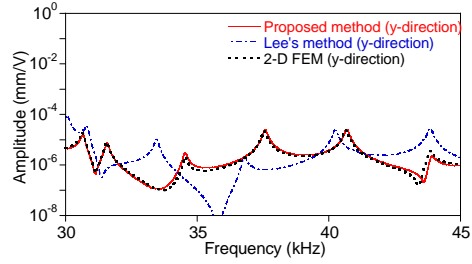
Fig. 3.22. A beam partially covered with a rigidly bonded PZT layer.

For discretizing the model in Fig. 3.22, two single beam spectral elements and one CPBS spectral element with a single PZT wafer are used in the proposed method and Lee's method. In the 2-D FE analysis, 406 8-node quadratic plane stress piezoelectric elements (size: 0.5mm× 0.38mm per each element) and 2615 8-node quadratic plane stress solid elements (size: 0.5mm×0.5mm per each element) are employed for discretizing the PZT wafer and the base beam, respectively. A 2-D FE analysis is performed using the Steady-State Dynamic Analysis, Direct of ABAQUS 6.7-4 on IBM p595 at KISTI Supercomputing Center.

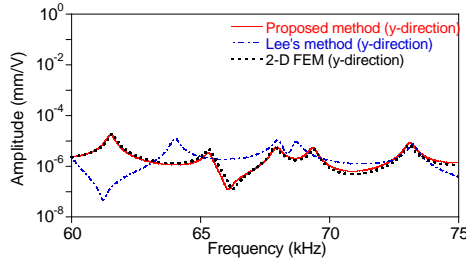




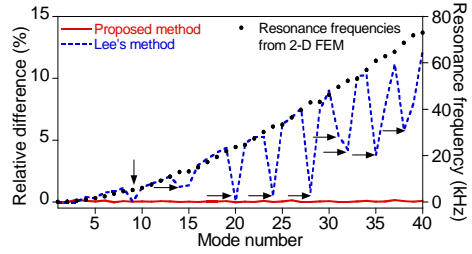
(a) FRFs of vertical displacements obtained at the right free end of the base beam. (0~15kHz)



(b) FRFs of vertical displacements obtained. (30~45kHz)



(c) FRFs of vertical displacements obtained. (60~75kHz)



(d) Relative difference of the resonance frequencies.

Fig. 3.23 Comparison of the FRFs and the Relative difference of the resonance frequencies from the proposed method, Lee' s method and 2-D FEM.

Fig. 3.23 compares the FRFs and Relative difference of the resonance frequencies obtained from the proposed method, Lee' s method and 2-D FEM, respectively. The frequency resolution is 1Hz for all the FRFs. In the low frequency range of less than 5 kHz shown in Figs. 3.23(a), all three methods produce almost identical FRFs. However, the frequency function from Lee' s method begins to deviate from those from the proposed method and 2-D FEM over 5kHz as shown Fig 3.23(b) and Fig 3.23(c). As the driving frequency increases, the higher

mode effects of the base beam start playing significant roles due to rotational inertia and shear deformation. However, these higher mode effects cannot be properly taken into account in Lee' s method.

Fig. 3.23(d) shows the relative difference between the resonance frequencies obtained from the spectral element methods and 2-D FEM. Here, the spectral element methods include the proposed method and Lee' s method. The first 40 lowest resonance frequencies are extracted by picking up the peaks of the FRFs. The proposed method produces very accurate resonance frequencies within  $\pm 0.2\%$  error level compared to those from 2-D FEM. On the other hand, the resonance frequencies from Lee' s method deviate from those from 2-D FEM as the driving frequency increases and the relative error at the 40<sup>th</sup> mode exceeds 10%.

## Chapter 4

### Parameter Study for Reference-free Damage Detection

In this section, numerical parameter study is conducted. The material properties and circuit scheme of the numerical model consist of base beam and PZT are adopted as the same in Subsection 3.4. Also, the identical geometries with collocated PZT wafers are used as shown Fig. 3.16. From the sensing circuit of each PZT wafer which allows the excitation and sensing, an output voltage across the reference capacitor is measured to obtain the EM admittance. Also, proposed method is conducted to compute the EM signals from the collocated PZT wafers under the 2-D plane stress condition. The mesh layout for SE discretization is identical to that used in Subsection 3.4.4

#### 4.1 The Varying Location and the Severity of Damage.

Proposed method using spectral element is performed by varying the location and depth of the notch as shown in Fig 4.1.

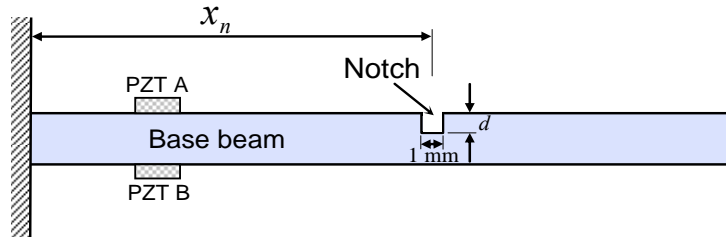
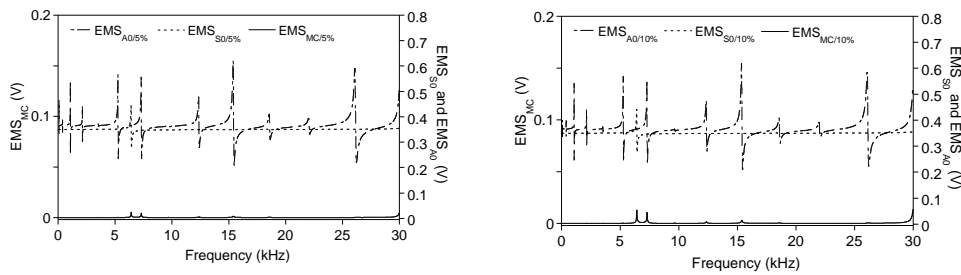


Fig. 4.1. Parameter study model for simulating different damage scenarios: The location ( $x_n$ ) of a notch is varied from 80, 100 and 150mm away from the fixed end, respectively. The depth ( $d$ ) of the notch is also varied from 0 to 2.1mm.

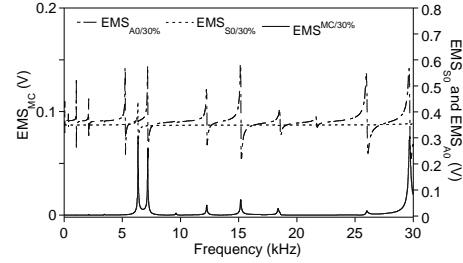
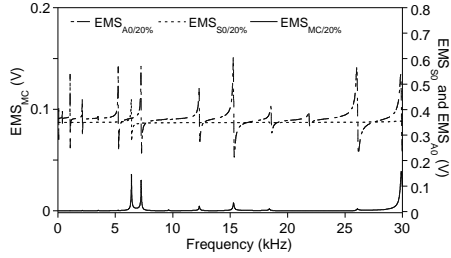
The notch location, denoted as  $x_n$  from the fixed end of the beam, is varied from 80mm to 100 and 150mm, respectively. The depth of the notch denoted as  $d$  is varied from 0.15 to 0.3, 0.6, 0.9, 1.5 and 2.1mm. The notch width is kept 1mm for all cases. The collocated PZTs are denoted as PZTs A and B, respectively. The EM signals from the collocated PZT wafers are computed up to 30 kHz.

For the aforementioned damage scenarios, a harmonic driving voltage with the amplitude of  $\pm 1$  volt is exerted on the top of PZTs A and B alternately. At the same time,  $EMS_{AA}$ ,  $EMS_{AB}$  and  $EMS_{BB}$  corresponding to the harmonic voltage input are calculated from the collocated PZT wafers. Substituting these computed  $EMS_{AA}$  and  $EMS_{BB}$  and  $EMS_{AB}$  into Eq. (2.3), decomposed EM signals associated with  $S_0$ ,  $A_0$  and mode-converted LW mode signals are obtained.

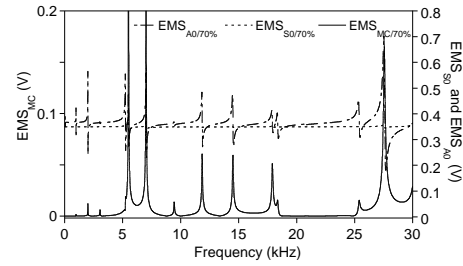
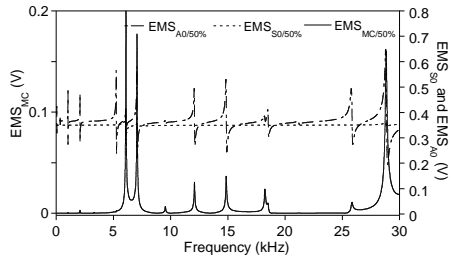
The typical examples of the decomposed EM signals already have been demonstrated in Figs. 3.19 and 3.20 for the intact and damaged cases. In a similar fashion, it will be presented the decomposed EM signals corresponding to the other damage cases due to varied notch depth when the notch depth is varied from 0.15 to 0.3, 0.6, 0.9, 1.5 and 2.1mm. First, Fig. 4.2 is the decomposed signals at the 80mm notch location from the fixed end of the beam.



(a) 5% damage case at the 80mm notch location. (b) 10% damage case at the 80mm notch location.



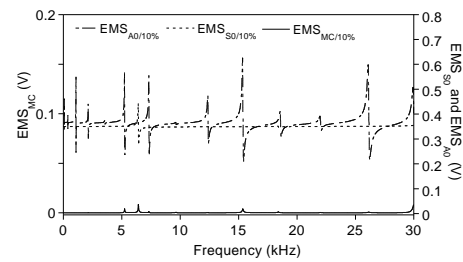
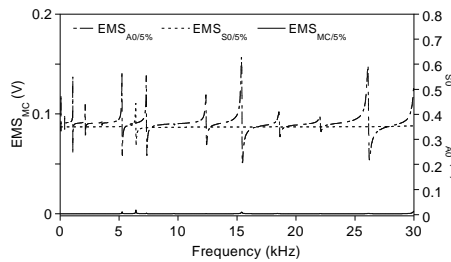
(c) 20% damage case at the 80mm notch location. (d) 30% damage case at the 80mm notch location.



(e) 50% damage case at the 80mm notch location. (f) 70% damage case at the 80mm notch location.

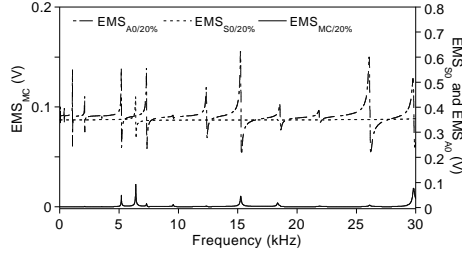
Fig. 4.2 Comparison of decomposed EMS signals corresponding to damage case at the 80mm notch location from the fixed end.

Next, Fig. 4.3 is the decomposed signals at the 100mm notch location from the fixed end of the beam.



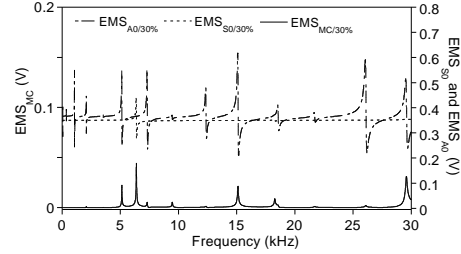
(a) 5% damage case at the 100mm (b) 10% damage case at the 100mm

notch location.

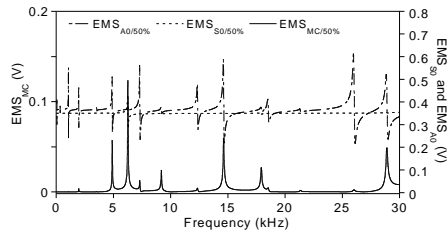


(c) 20% damage case at the 100mm notch location.

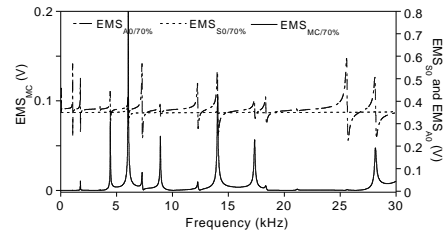
notch location.



(d) 30% damage case at the 100mm notch location.



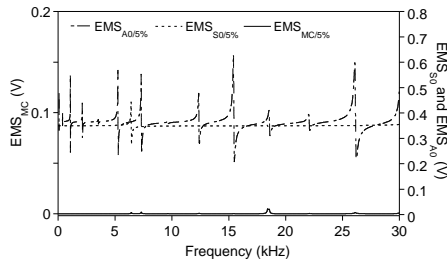
(e) 50% damage case at the 100mm notch location.



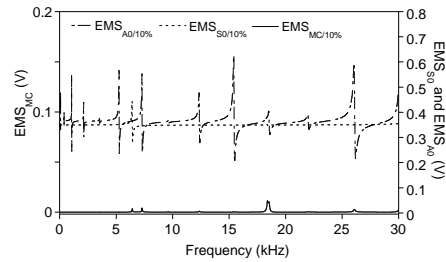
(f) 70% damage case at the 100mm notch location.

Fig. 4.3 Comparison of decomposed EMS signals corresponding to damage case at the 100mm notch location from the fixed end.

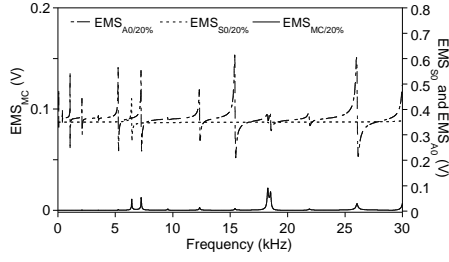
Finally, Fig. 4.4 is the decomposed signals at the 150mm notch location from the fixed end of the beam.



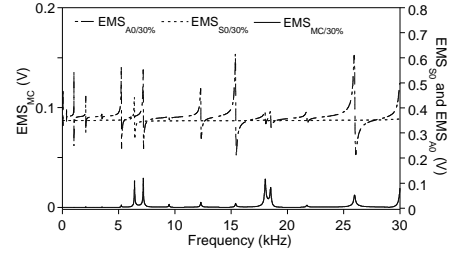
(a) 5% damage case at the 150mm notch location.



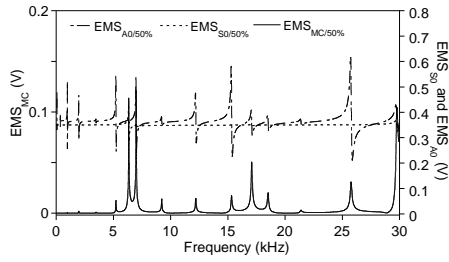
(b) 10% damage case at the 150mm notch location.



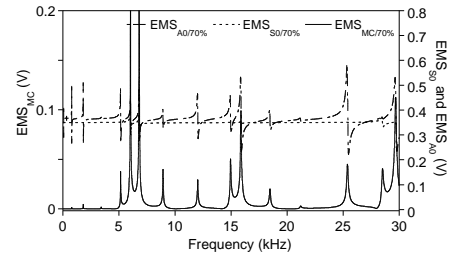
(c) 20% damage case at the 150mm notch location.



(d) 30% damage case at the 150mm notch location.



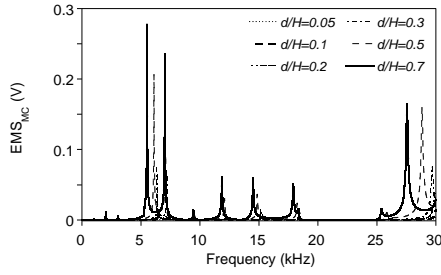
(e) 50% damage case at the 150mm notch location.



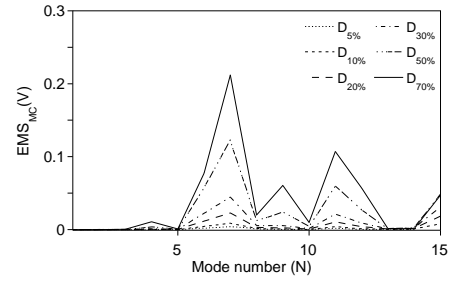
(f) 70% damage case at the 150mm notch location.

Fig. 4.4 Comparison of decomposed EMS signals corresponding to damage case at the 150mm notch location from the fixed end.

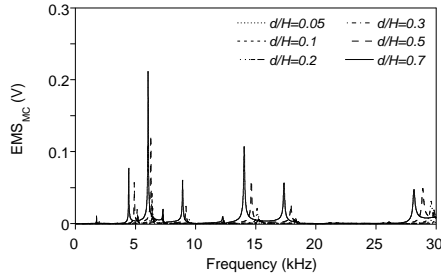
As mentioned in Subsection 3.4.4, the existence of a manifest notch itself is able to confirm through the mode-converted EM signals ( $EMS_{MC}$ ) in Fig. 4.5 without comparison to a prior baseline EMS. Especially, the  $EMS_{MC}$  variation due to the ratio of notch depth to the thickness of the base beam ( $d/H$ ) is well shown in Figs. 4.5(a), (c) and (e). Also, the peak values of these  $EMS_{MC}$  according to the mode number can be compared in Figs 4.5(b), (d) and (f).



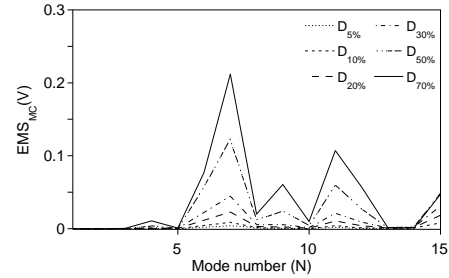
(a) The only extracted  $EMS_{MC}$  signals from the Fig. 4.2.



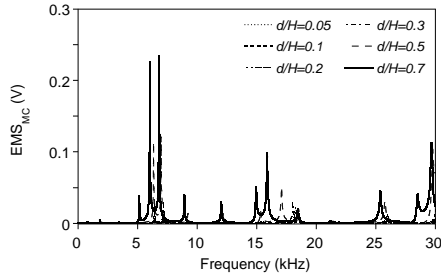
(b) The peak values of the  $EMS_{MC}$  according to the mode number from Fig. 4.5(a).



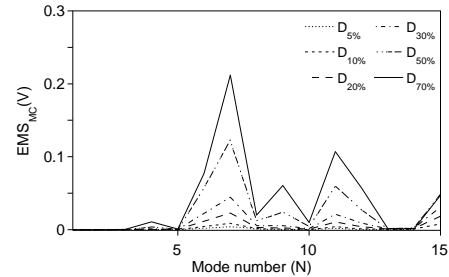
(c) The only extracted  $EMS_{MC}$  signals from the Fig. 4.3.



(d) The peak values of the  $EMS_{MC}$  according to the mode number from Fig. 4.5(c).



(e) The only extracted  $EMS_{MC}$  signals from the Fig. 4.4.



(f) The peak values of the  $EMS_{MC}$  according to the mode number from Fig. 4.5(e).

Fig. 4.5 Comparison of extracted  $EMS_{MC}$  signals and the peak values when the notch occurs at the 80, 100 and 150mm notch location from the fixed end.

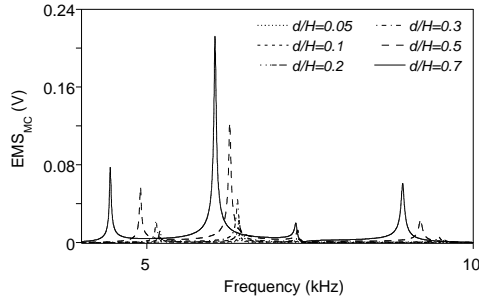


When the location of notch ( $x_n$ ) is 100mm away from the fixed end of the base beam, Figs. 4.6(a), (b) and (c) show the detailed  $EMS_{MC}$  in the frequency ranges 4–10kHz, 10–20kHz and 20–30kHz, respectively. First, the peak frequencies in  $EMS_{MC}$  corresponding to the resonant frequencies of the cantilever beam decrease as notch depth increases. The increasing depth of the notch makes the base beam less stiff while the loss of mass is negligible. Therefore, the resonant frequency values decrease in the frequency domain in Figs. 4.6(a), (b) and (c). Second, the peak values of  $EMS_{MC}$  increase as the notch gets deeper. It is commonly known that the total energy of the mode-converted LW mode increases as the incident LW modes encounter a deeper notch during wave propagation. This mode conversion phenomena result in the increasing peak values in  $EMS_{MC}$  with respect to the notch depth. Fig. 4.6(d) demonstrates the RMS values  $EMS_{MC}$  due to mode conversion in terms of the ratio of notch depth to the thickness of the base beam ( $d/H$ ). The RMS values are calculated through numerical integration of whole  $EMS_{MC}$  up to 30kHz in Fig. 4.5(c), and then normalized with respect to the frequency interval (30 kHz). Regardless of the location of the notch, the RMS values increase as  $d/H$  increases. The RMS values for all three locations increase in a similar fashion up to  $d/H=0.2$ . When  $d/H$  is greater than 0.3, the RMS values for  $x_n=80$ cm are larger than those for  $x_n=100$  cm and 150 cm.

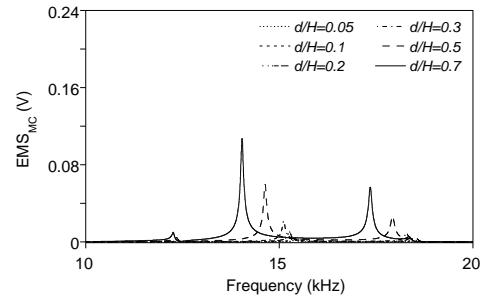
In conclusion, the possibility of advanced damage detection using  $EMS_{MC}$  has been demonstrated through the parameter study for

detecting a notch-shaped damage with varying locations and depths on a plate-like structure.

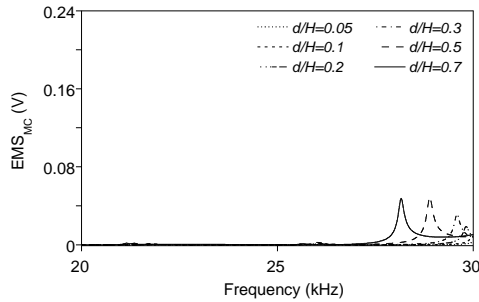
In Fig. 4.5, the peak values illustrate the difference size according to arbitrary mode. The authors believe that the surface strain mode shape in the vicinity of the notch play a crucial role in determining  $EMS_{MC}$  and their RMS values. The sensitivity analysis of RMS values in terms of the notch location is now under consideration through analyzing the modal surface strain of the base beam. A preliminary result on the relationship between the modal surface strain and  $EMS_{MC}$  is provided in the next subsection.



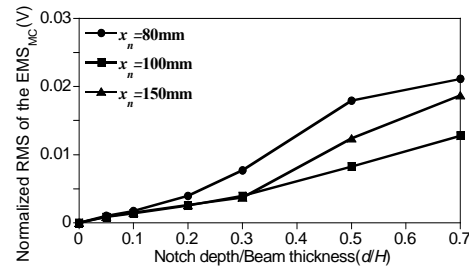
(a) A magnified version of  $EMS_{MC}$  in Fig. 4.5 (c) for 4–10 kHz.



(b) A magnified version of  $EMS_{MC}$  in Fig. 4.5 (c) for 10–20kHz.



(c) A magnified version of  $EMS_{MC}$  in



(d) The RMS amplitude of

Fig. 4.5 (c) for 20–30 kHz.  $EMS_{MC}$  as a function of  $(d/H)$ .

Fig. 4.6  $EMS_{MC}$  and their RMS amplitudes corresponding to a notch with varying depth and location in Fig. 4.1.

## 4.2 The Effects of the Model Surface Strain Shape (MSSS) on the Amplitude of $EMS_{MC}$ .

When the EMS is measured from a surface-mounted PZT wafer, the amplitude of EMS is proportional to the surface strain of a host structure. The dynamic surface strain becomes steady-state at the presence of harmonic excitation and can be represented by mode shape at each resonant frequency. For the brevity of description, this mode shape of the surface strain is referred to as modal surface strain shape (MSSS) hereafter. Note that the MSSS shares the common terms used in modal analysis such as node and anti-node.

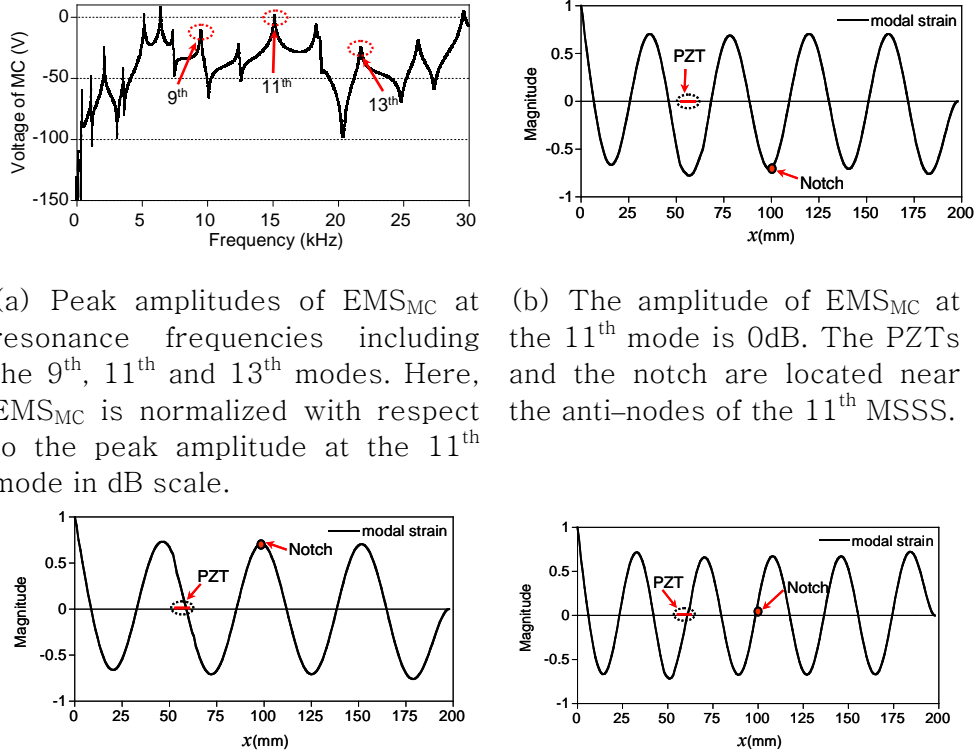
The effect of the MSSS on the amplitude of  $EMS_{MC}$  is investigated for the damaged cantilever beam in Fig. 4.1. Here, the MSSS is calculated through proposed method. Fig. 4.7(a) presents  $EMS_{MC}$  from 0 to 30kHz which is normalized with respect to the peak amplitude at the 11<sup>th</sup> mode in dB scale. Considering each peak amplitudes and the corresponding MSSS, 9<sup>th</sup>, 11<sup>th</sup> and 13<sup>th</sup> modes are selected for the investigation. Among the selected modes, the 11<sup>th</sup> mode shows the largest peak amplitude (0dB) in Fig. 4.7(a). Fig. 4.7(b) presents the MSSS at the 11<sup>th</sup> mode in which the PZT wafers as well as the notch are located at the antinodes of the MSSS. The peak amplitude of the 9<sup>th</sup> mode is -11.9dB being 4 times smaller than that of the 11<sup>th</sup> mode. Fig.

4.7(c) illustrates that the PZT wafers are located at the node of the 9<sup>th</sup> MSSS while the notch is at the anti-node. Finally, the peak amplitude of the 13<sup>th</sup> mode is  $-21.7\text{dB}$  being 5 times smaller than that of the 11<sup>th</sup> mode. The PZT wafers and the notch are located on the nodes of the 13<sup>th</sup> MSSS as shown in Fig. 4.7(d). From the numerical results in Fig. 4.7, the sweet spots for the PZTs and the notch producing the large peak amplitude of  $\text{EMS}_{\text{MC}}$  are found to be the antinodes in each MSSS. If either of the PZT or the notch falls on the node of the MSSS, the peak amplitude of the corresponding  $\text{EMS}_{\text{MC}}$  decreases significantly [Fig. 4.7(c)]. If both the PZT and the notch are on the node of the MSSS, the peak amplitude of the corresponding  $\text{EMS}_{\text{MC}}$  becomes significantly small [Fig. 4.7(d)].

Two important implications can be drawn for the damage diagnosis of a plate-like structure using  $\text{EMS}_{\text{MC}}$ . First, the PZT wafer should be placed carefully considering the MSSS involved within the chosen driving frequency range. The MSSS can be computed through either 2-D FEM or proposed method. Then, the sweet spots such as the antinodes of the MSSS can be selected. Installing the PZT wafer one of these sweet spots, the sensing and actuating capabilities of the PZT wafer can be greatly improved. Second, the usage of a broad band frequency range is recommended for capturing  $\text{EMS}_{\text{MC}}$ . Unlike the installation of the PZT wafer, no one can guarantee that damage should occur at the sweet spots. Fortunately, this uncertainty can be considerably reduced because the number of sweet spots increases

through multiple modal surface strain shapes existing within the broad band frequency range.

Finally, the sensitivity analysis of the MSSS on  $EMS_{MC}$  through proposed method will open the opportunity of selecting the optimal number and placement of the PZT wafers enhancing damage detectability for a plate-like structure.



(a) Peak amplitudes of  $EMS_{MC}$  at resonance frequencies including the 9<sup>th</sup>, 11<sup>th</sup> and 13<sup>th</sup> modes. Here,  $EMS_{MC}$  is normalized with respect to the peak amplitude at the 11<sup>th</sup> mode in dB scale.

(b) The amplitude of  $EMS_{MC}$  at the 11<sup>th</sup> mode is 0dB. The PZTs and the notch are located near the anti-nodes of the 11<sup>th</sup> MSSS.

(c) The amplitude of  $EMS_{MC}$  at the 9<sup>th</sup> mode is -11.9 dB. Both PZTs are located at the node of the 9<sup>th</sup> MSSS whereas the notch is placed near the anti-node.

(d) The amplitude of  $EMS_{MC}$  at the 13<sup>th</sup> mode is -21.7dB. Both PZTs and the notch are located near the nodes of the 13<sup>th</sup> MSSS.

Fig. 4.7 The effects of MSSS at the PZT and notch locations on the amplitude of  $EMS_{MC}$

### 4.3 Imperfection Problem of the PZT Wafer.

From now on, in our study, all simulation tests were performed in the perfect condition except for this one. The perfection condition means that the PZTs bonded on the top and bottom surface of the base beam consist in the symmetric. Therefore, imperfection is said to be asymmetric condition.

In the signal-decomposition using a pair of collocated PZTs for detecting damage and classification, the imperfection has to overcome the drawback because it requires much effort to make the symmetric structure system including the attached PZTs which enables more exact damage detecting.

Numerical analysis of the imperfection was carried out as the following model in Fig. 4.8. The SE analyses are performed by varying the location of the PZT.

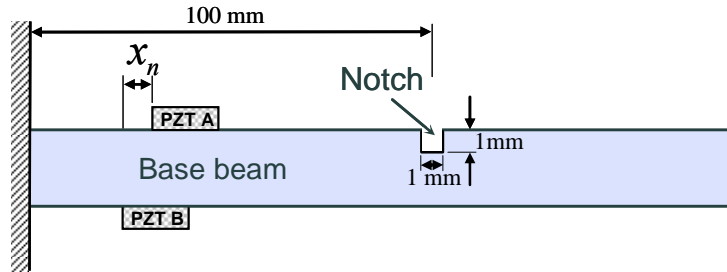
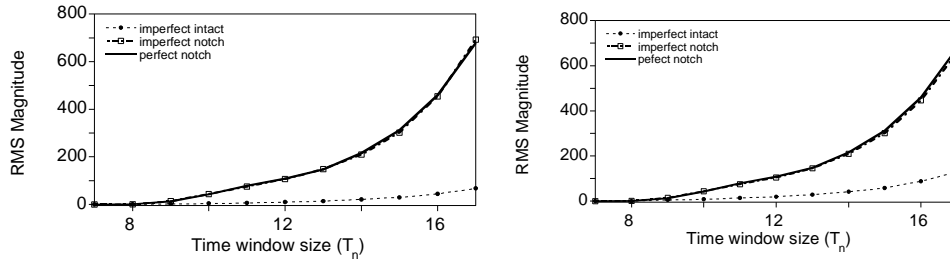
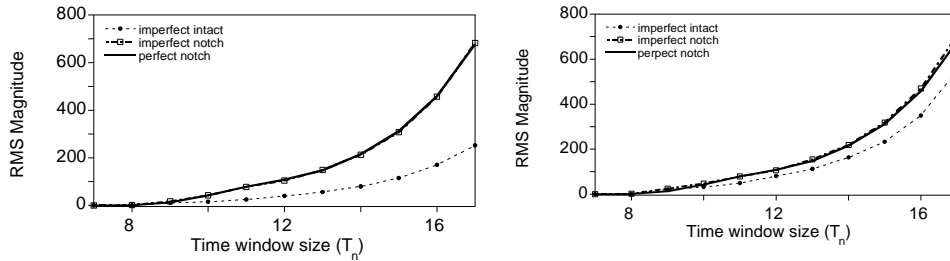


Fig. 4.8. Parameter study model for simulating PZT imperfection; The imperfection length ( $x_n$ ) of a PZT is 0.25mm, 0.5mm, 1.0mm and 2.0mm  $x_n$  from the end of the opposite PZT, respectively. The depth ( $d$ ) and width is constant ( $1 \times 1$ mm).

The imperfection length of PZT, denoted as  $x_n$  from the end of the opposite PZT, is varied from 0mm, 0.25mm, 0.5mm, 1.0mm and 2.0mm, respectively. The size of the notch is  $1 \times 1$ mm and the location is 100mm from the fixed end of the beam. The notch width is kept 1mm for all cases. The collocated PZTs are denoted as PZTs A and B, respectively. Also, input tone burst signals with central frequency 100 kHz is used to examine the effect of imperfect condition as shown Fig. 4.9.



(a) The RMS values associated with 0.25mm imperfection of collocated PZT wafer. (b) The RMS values associated with 0.50mm imperfection of collocated PZT wafer.



(c) The RMS values associated with 1.0mm imperfection of collocated PZT wafer. (d) The RMS values associated with 2.0mm imperfection of collocated PZT wafer.

Fig. 4.9 The variation of total RMS values according to the PZT bonding state when the 100kHz tone burst input excited and time window size increase.

In Fig. 4.9, the RMS values are calculated through the integration of temporal spectrum as similar to the subsection 2.3. The imperfection is not affected with intact case when the imperfection is small in the Fig. 4.9(a). As the imperfection is increased from 0.25mm to 2.0mm, the RMS values of intact case is closed to the notch case because the imperfection effect of intact case is considered to the like damage as shown Fig 4.9(d).



## Chapter 5

### Concluding Remarks

#### 5.1 Executive Summary

The objective of this research is to study the reference-free damage detection technique based on the EM signal through correlation analysis between LW signals and EM signals. This thesis proposes two technical developments to overcome the limitations of existing damage detection techniques using piezoelectric (PZT) wafer. The main achievements of this study are summarized as follows:

First, the temporal spectrum is proposed to understand the signal characteristic of EM signal in the frequency domain. The temporal spectrum analysis is a simple principle that converts the transient state signals of LW into the steady state signals, such as EM impedance and admittance, through fast Fourier transform (FFT). Deriving an analytic solution for the complex behavior between transient and steady state LW is difficult; therefore, temporal spectrum is a very important technique to understand the EM signals through the interaction between electric characteristic of the PZT and the mechanical characteristic of the host structure. The root mean squares (RMS) of the temporal spectrums indicate that the signal to noise ratio associated with damage is amplified as the time window size increases. In this regard, the possibility of the reference-free damage detection based on the EM signal is proposed.

Numerical simulations through temporal spectrum are performed to

demonstrate the validity of the mode-converted EM signal-decomposition technique for detecting damage on a plate. These characteristics are the same, even when the input signal changes from harmonic to tone burst excitation.

Second, we have developed a full modeling technique to interpret EM interaction between a host structure and PZT wafers. The full modeling technique presents spectral element formulation for a coupled PZT and Beam system (CPBS), in which PZT wafers are perfectly bonded on a base beam. Mindlin-Herrmann rod theory and Timoshenko beam theory are employed to approximate longitudinal and flexural behaviors, respectively, of the base beam in a high-frequency range. One-dimensional linear piezoelectricity is adopted for the PZT wafer. Considering the dual functions of the PZT wafer as an actuator and a sensor, appropriate electric boundary conditions are used in spectral element formulation. A dynamic stiffness matrix for the CPBS element is derived through condensation technique. Furthermore, spectral elements representing delamination and crack in the base beam can be incorporated into the proposed method for quantifying the effects of damage on the high-frequency dynamic responses.

The validity of the proposed method is demonstrated through three numerical examples. In the case of a cantilever beam with a partially bonded PZT wafer, the EM admittance curves of the single PZT wafer computed from the proposed method agree well with those from 2-D FE analysis and experiment. In the second numerical example, the frequency respons functions (FRFs) of displacement at the three

points are calculated when a harmonic input signal with unit voltage is applied to the PZT wafer. The proposed method produces FRFs very close to those obtained from two-dimensional (2-D), three-dimensional (3-D) FE analysis and experiment, even in a high-frequency range, because the secondary dynamic effects due to rotational inertia and shear deformation are properly taken into account.

In the third and fourth numerical example, the collocated PZT wafers are used for exciting and sensing of EM signal on a cantilever beam. The relative differences at the resonance frequency of admittance are properly predicted between proposed method and 2-D FE analysis in the frequency domain. Considering the huge computational cost needed by 2-D FE analysis, the proposed method can be an efficient alternative for EM signal simulation. Also, EM signal-based decomposition technique is verified.

In summary, EM signal-based reference-free damage diagnosis technique is first proposed. This approach is believed to be more sensitive to an incipient defect because the input excitation to the PZT creates the resonance of the mode-converted damage signal at its natural frequencies. Thus, it is more capable of achieving higher signal-to-noise ratio than the LW signal-based damage detection.

## 5.2 Further Study

It is very important that some signal will be used for damage detection. The research presented in this dissertation can be used in the basic motive for reference-free detecting damage. Most of our research is an approach results of theoretical and numerical through the simple cantilever model. Further studies are planned to apply the proposed techniques to more complicate or real structures. The final destination of SHM/NDT is the prediction of unexpected accidents in advance using some novelty damage detection techniques. To satisfy the goals of SHM / NDT, some possible improvements studies are proposed and listed as follow:

- 1) Further numerical modeling techniques to advanced understand the proposed technique and improve interaction between the plate and PZT wafers are necessary. For example, the effects of adhesive layer between a spectral element and a PZT wafer will be taken into account as well for improved dynamic analysis at a high frequency range. In the numerical model, the more complicate models consist of stiffener or several damages will make the reliability of proposed method.
- 2) From the fundamental finding that impedance method is quite associated with LW-based method, more robust damage detection techniques incorporating those two techniques will be developed and applied to lab and real structures. In reference-free damage detection technique, the technique will be extended to real structures such as

considering temperature and loading effect of plate, critical points of bridge and wing section of aircraft. Also, investigation of other damage types like bolts-loosen and corrosion cases will be studied for reliable on-line health monitoring.

3) Proposed method uses the contacted PZT wafer on the host structure to extract damage signal. Recently, the laser instrument which can excite and detect a damage signal without contact is used for detecting damage. If the symmetry of the structure is considered, the proposed technique can be applied equally. As well as, it is necessary to develop intelligent damage index methods that can effectively correlate the changes in the wave packet to the presence and changes of damages in the structure. Also, the effort to overcome the limitations of the proposed method is needed, such as the imperfection which is simulated in our study.

## APPENDIX

## 1) APPENDIX (A1)

$$\mathbf{C} = c_{ij} = c_{ji} \quad (1 \leq i, j \leq 4)$$

(a) In case of a CPBS with a single PZT wafer:

$$\begin{aligned} c_{11} &= \omega^2 \Theta - k^2 (2\mu_b + \lambda_b) A_b - k^2 E_p A_p, \quad c_{12} = \frac{ik}{2} h_p (\omega^2 \alpha_b - k^2 \beta_b) - ik \lambda_b A_b \\ c_{13} &= ik (\omega^2 \alpha_p - k^2 \beta_p), \quad c_{14} = -(\omega^2 \alpha_b - k^2 \beta_b) \\ c_{22} &= -\omega^2 \kappa_2 \rho_b I_b - \frac{k^2}{8} h_b h_p^2 (\omega^2 \alpha_b - k^2 \beta_b) - \frac{\omega^2}{2} h_b \alpha_b + (2\mu_b + \lambda_b) A_b + k^2 \kappa_1 \mu_b I_b + \frac{k^4}{4} h_b^2 C_{11}^D I_p \\ c_{23} &= -\omega^2 \alpha_b - \frac{k^2}{4} h_b h_p (\omega^2 \alpha_p - k^2 \beta_p) + \frac{k^4}{2} h_b C_{11}^D I_p \\ c_{24} &= -\frac{ik}{4} h_b h_p (\omega^2 \alpha_b - k^2 \beta_b), \quad c_{33} = -\omega^2 \Theta - \frac{k^2}{2} h_p (\omega^2 \alpha_p - k^2 \beta_p) + k^2 K_1 \mu_b A_b + k^4 C_{11}^D I_p \\ c_{34} &= -\frac{ik}{2} h_b (\omega^2 \alpha_p - k^2 \beta_p) - ik K_1 \mu_b A_b, \quad c_{44} = -k^2 E_b I_b + \omega^2 K_2 \rho_b I_b + \frac{h_b}{2} (\omega^2 \alpha_b - k^2 \beta_b) - K_1 \mu_b A_b \end{aligned}$$

where

$$\Theta = \rho_b A_b + \rho_p A_p; \alpha_b = \frac{1}{2} \rho_p A_p h_b; \alpha_p = \frac{1}{2} \rho_p A_p h_p; \beta_b = \frac{1}{2} E_p A_p h_b; \beta_p = \frac{1}{2} E_p A_p h_p$$

(b) In case of a CPBS with collocated PZT wafers:

$$\begin{aligned} c_{11} &= \omega^2 \tilde{\Theta} - k^2 (2\mu_b + \lambda_b) A_b - k^2 \tilde{E}_p A_p, \quad c_{12} = \frac{ik}{2} h_p (\omega^2 \tilde{\alpha}_b - k^2 \beta_b) - ik \lambda_b A_b \\ c_{22} &= -\omega^2 \kappa_2 \rho_b I_b - \frac{k^2}{8} h_b h_p^2 (\omega^2 \tilde{\alpha}_b - k^2 \beta_b) - \frac{\omega^2}{2} h_b \tilde{\alpha}_b + (2\mu_b + \lambda_b) A_b + k^2 \kappa_1 \mu_b I_b + \frac{k^4}{4} h_b^2 C_{11}^D I_p \\ c_{33} &= -\omega^2 \tilde{\Theta} - \frac{k^2}{2} h_p (\omega^2 \tilde{\alpha}_p - k^2 \beta_p) + k^2 K_1 \mu_b A_b + k^4 C_{11}^D I_p \\ c_{34} &= -\frac{ik}{2} h_p (\omega^2 \tilde{\alpha}_b - k^2 \beta_b) - ik K_1 \mu_b A_b \\ c_{44} &= -k^2 E_b I_b + \omega^2 K_2 \rho_b I_b + \frac{h_b}{2} (\omega^2 \tilde{\alpha}_b - k^2 \beta_b) - K_1 \mu_b A_b \\ c_{13} &= c_{14} = c_{23} = c_{24} = 0 \end{aligned}$$

where

$$\tilde{\Theta} = \rho_b A_b + 2\rho_p A_p; \tilde{\alpha}_b = \rho_p A_p h_b; \tilde{\alpha}_p = \rho_p A_p h_p; \tilde{E}_p = 2E_p$$

## 2) APPENDIX (A2)

(a) In case of a CPBS with a single PZT wafer:

$\mathbf{A} = a_i \quad (1 \leq i \leq 10)$

$$\mathbf{H}(\omega) \equiv \begin{Bmatrix} \Phi_{\hat{u}}(0) \\ \Phi_{\hat{\psi}}(0) \\ \Phi_{\hat{v}}(0) \\ \Phi_{\hat{\phi}}(0) \\ \Phi_{\hat{u}}(L) \\ \Phi_{\hat{\psi}}(L) \\ \Phi_{\hat{v}}(L) \\ \Phi_{\hat{\phi}}(L) \end{Bmatrix} = \begin{bmatrix} R_1 & R_2 & R_3 & R_4 & R_5 & R_1 P_1 & R_2 P_2 & R_3 P_3 & R_4 P_4 & R_5 P_5 \\ S_1 & S_2 & S_3 & S_4 & S_5 & -S_1 P_1 & -S_2 P_2 & -S_3 P_3 & -S_4 P_4 & -S_5 P_5 \\ T_1 & T_2 & T_3 & T_4 & T_5 & -T_1 P_1 & -T_2 P_2 & -T_3 P_3 & -T_4 P_4 & -T_5 P_5 \\ 1 & 1 & 1 & 1 & 1 & P_1 & P_2 & P_3 & P_4 & P_5 \\ R_1 P_1 & R_2 P_2 & R_3 P_3 & R_4 P_4 & R_5 P_5 & R_1 & R_2 & R_3 & R_4 & R_5 \\ S_1 P_1 & S_2 P_2 & S_3 P_3 & S_4 P_4 & S_5 P_5 & -S_1 & -S_2 & -S_3 & -S_4 & -S_5 \\ T_1 P_1 & T_2 P_2 & T_3 P_3 & T_4 P_4 & T_5 P_5 & -T_1 & -T_2 & -T_3 & -T_4 & -T_5 \\ P_1 & P_2 & P_3 & P_4 & P_5 & 1 & 1 & 1 & 1 & 1 \end{bmatrix}$$

Where,  $P_i = e^{-ik_i L}$  such that  $k_i \in \{k \mid \det[c_{ij}(k)] = 0 \quad (1 \leq i, j \leq 4) \text{ in Appendix (A1-a)}\}$ .

For each  $k_i$ , an eigenvector normalized with respect to  $\phi_0$  is calculated and its individual components corresponding to  $u_0$ ,  $\psi_0$  and  $v_0$  are  $R_i$ ,  $S_i$  and  $T_i$ , respectively.

(b) In case of a CPBS with collocated PZT wafers:

$\mathbf{A} = a_i \quad (1 \leq i \leq 12)$

$$\mathbf{H}(\omega) \equiv \begin{Bmatrix} \Phi_{\hat{u}}(0) \\ \Phi_{\hat{\psi}}(0) \\ \Phi_{\hat{v}}(0) \\ \Phi_{\hat{\phi}}(0) \\ \Phi_{\hat{u}}(L) \\ \Phi_{\hat{\psi}}(L) \\ \Phi_{\hat{v}}(L) \\ \Phi_{\hat{\phi}}(L) \end{Bmatrix} = \begin{bmatrix} 1 & 1 & 1 & P_1 & P_2 & P_3 & 0 & 0 & 0 & 0 & 0 & 0 \\ S_1 & S_2 & S_3 & -S_1 P_1 & -S_2 P_2 & -S_3 P_3 & 0 & 0 & 0 & 0 & 0 & 0 \\ 0 & 0 & 0 & 0 & 0 & 0 & 1 & 1 & 1 & \tilde{P}_1 & \tilde{P}_2 & \tilde{P}_3 \\ 0 & 0 & 0 & 0 & 0 & 0 & T_1 & T_2 & T_3 & -T_1 \tilde{P}_1 & -T_2 \tilde{P}_2 & -T_3 \tilde{P}_3 \\ P_1 & P_2 & P_3 & 1 & 1 & 1 & 0 & 0 & 0 & 0 & 0 & 0 \\ S_1 P_1 & S_2 P_2 & S_3 P_3 & -S_1 & -S_2 & -S_3 & 0 & 0 & 0 & 0 & 0 & 0 \\ 0 & 0 & 0 & 0 & 0 & 0 & \tilde{P}_1 & \tilde{P}_2 & \tilde{P}_3 & 1 & 1 & 1 \\ 0 & 0 & 0 & 0 & 0 & 0 & T_1 \tilde{P}_1 & T_2 \tilde{P}_2 & T_3 \tilde{P}_3 & -T_1 & -T_2 & -T_3 \end{bmatrix}$$

where  $P_i = e^{-ik_i L}$  such that  $k_i \in \{k \mid \det[c_{ij}(k)] = 0 \quad (1 \leq i, j \leq 2) \text{ in Appendix (A1-b)}\}$  and

$\tilde{P}_i = e^{-i\tilde{k}_i L}$  such that  $\tilde{k}_i \in \{k \mid \det[c_{ij}(k)] = 0 \quad (3 \leq i, j \leq 4) \text{ in Appendix (A1-b)}\}$ .

For each  $k_i$ , an eigenvector normalized with respect to  $u_0$  is calculated and its component corresponding to  $\psi_0$  is  $R_i$ . For each  $\tilde{k}_i$ , an eigenvector normalized with respect to  $v_0$  is calculated and its component associated with  $\phi_0$  is  $T_i$ .

## 3) APPENDIX (A3)

(a) In case of a CPBS with a single PZT wafer:

$$\mathbf{F} \equiv \{-F(0), -Q(0), -V(0), -M(0), F(L), Q(L), V(L), M(L), 0, 0\}^T$$

$$\mathbf{F}_v \equiv \frac{E_p w_p \bar{d}_{31} \bar{v}}{2} \times \{-2, 0, 0, h_b, 2, 0, 0, -h_b, -h_p, h_p\}^T \text{ for PZT excitation}$$

$$\mathbf{F}_v = \mathbf{0} \text{ for PZT sensing}$$

(b) In case of a CPBS with collocated PZT wafers:

$$\mathbf{F} \equiv [-F(0), -Q(0), -V(0), -M(0), F(L), Q(L), V(L), M(L), 0, 0, 0, 0]^T$$

$$\mathbf{F}_v \equiv \frac{E_p w_p}{4} \times \{-4\varphi_1, 0, 0, 2h_b\varphi_2, 4\varphi_1, 0, 0, -2h_b\varphi_2, -h_b h_p \varphi_1, -2h_p \varphi_2, h_b h_p \varphi_1, 2h_p \varphi_2\}^T$$

for PZT excitation

$$\text{where } \varphi_1 = \bar{d}_{31} \bar{v} + \underline{d}_{31} \underline{v} \text{ and } \varphi_2 = \bar{d}_{31} \bar{v} - \underline{d}_{31} \underline{v}$$

$$\mathbf{F}_v = \mathbf{0} \text{ for PZT sensing}$$



## 4) APPENDIX (A4)

(a) In case of a CPBS with a single PZT wafer:

$$\begin{aligned}
\text{Actuator } \mathbf{G}(\omega) = & \begin{bmatrix}
-(2\mu_b + \lambda_b)A_b\Phi'_u(0) - \lambda_b A_b\Phi'_\psi(0) - E_p A_p \tilde{\Phi}'_u(0) - \frac{E_p A_p \bar{d}_{31} \bar{h}_{31}}{L} \tilde{\Delta}'_u \\
-\kappa_1 \mu_b I_b \Phi'_\psi(0) - \omega^2 \frac{\rho_p A_p h_b h_p}{4} \tilde{\Phi}'_u(0) - \frac{E_p A_p h_b h_p}{4} \tilde{\Phi}''_u(0) + \frac{C_{11}^D I_p h_b}{2} \tilde{\Phi}'_\phi(0) \\
-K_1 \mu_b A_b [\Phi'_\psi(0) - \Phi'_\phi(0)] - \omega^2 \frac{\rho_p A_p h_p}{2} \tilde{\Phi}'_u(0) - \frac{E_p A_p h_p}{2} \tilde{\Phi}''_u(0) + C_{11}^D I_p \tilde{\Phi}'_\phi(0) \\
-E_b I_b \Phi'_\phi(0) + \frac{E_p A_p h_b}{2} \tilde{\Phi}'_u(0) + \frac{E_p A_p \bar{d}_{31} \bar{h}_{31} h_b}{2L} \tilde{\Delta}'_u \\
(2\mu_b + \lambda_b)A_b\Phi'_u(L) + \lambda_b A_b\Phi'_\psi(L) + E_p A_p \tilde{\Phi}'_u(L) + \frac{E_p A_p \bar{d}_{31} \bar{h}_{31}}{L} \tilde{\Delta}'_u \\
\kappa_1 \mu_b I_b \Phi'_\psi(L) + \omega^2 \frac{\rho_p A_p h_b h_p}{4} \tilde{\Phi}'_u(L) + \frac{E_p A_p h_b h_p}{4} \tilde{\Phi}''_u(L) - \frac{C_{11}^D I_p h_b}{2} \tilde{\Phi}'_\phi(L) \\
K_1 \mu_b A_b [\Phi'_\psi(L) - \Phi'_\phi(L)] + \omega^2 \frac{\rho_p A_p h_p}{2} \tilde{\Phi}'_u(L) + \frac{E_p A_p h_p}{2} \tilde{\Phi}''_u(L) - C_{11}^D I_p \tilde{\Phi}'_\phi(L) \\
E_b I_b \Phi'_\phi(L) - \frac{E_p A_p h_b}{2} \tilde{\Phi}'_u(0) - \frac{E_p A_p \bar{d}_{31} \bar{h}_{31} h_b}{2L} \tilde{\Delta}'_u \\
-\frac{E_p A_p h_p}{2} \tilde{\Phi}'_u(0) + C_{11}^D I_p \tilde{\Phi}'_\phi(0) - \frac{E_p A_p \bar{d}_{31} \bar{h}_{31} h_p}{2L} \tilde{\Delta}'_u \\
\frac{E_p A_p h_p}{2} \tilde{\Phi}'_u(L) - C_{11}^D I_p \tilde{\Phi}'_\phi(L) + \frac{E_p A_p \bar{d}_{31} \bar{h}_{31} h_p}{2L} \tilde{\Delta}'_u
\end{bmatrix} \\
\\
\text{Sensor } \mathbf{G}(\omega) = & \begin{bmatrix}
-(2\mu_b + \lambda_b)A_b\Phi'_u(0) - \lambda_b A_b\Phi'_\psi(0) - E_p A_p \tilde{\Phi}'_u(0) \\
-\kappa_1 \mu_b I_b \Phi'_\psi(0) - \omega^2 \frac{\rho_p A_p h_b h_p}{4} \tilde{\Phi}'_u(0) - \frac{E_p A_p h_b h_p}{4} \tilde{\Phi}''_u(0) + \frac{C_{11}^D I_p h_b}{2} \tilde{\Phi}'_\phi(0) \\
-K_1 \mu_b A_b [\Phi'_\psi(0) - \Phi'_\phi(0)] - \omega^2 \frac{\rho_p A_p h_p}{2} \tilde{\Phi}'_u(0) - \frac{E_p A_p h_p}{2} \tilde{\Phi}''_u(0) + C_{11}^D I_p \tilde{\Phi}'_\phi(0) \\
-E_b I_b \Phi'_\phi(0) + \frac{E_p A_p h_b}{2} \tilde{\Phi}'_u(0) \\
(2\mu_b + \lambda_b)A_b\Phi'_u(L) + \lambda_b A_b\Phi'_\psi(L) + E_p A_p \tilde{\Phi}'_u(L) \\
\kappa_1 \mu_b I_b \Phi'_\psi(L) + \omega^2 \frac{\rho_p A_p h_b h_p}{4} \tilde{\Phi}'_u(L) + \frac{E_p A_p h_b h_p}{4} \tilde{\Phi}''_u(L) - \frac{C_{11}^D I_p h_b}{2} \tilde{\Phi}'_\phi(L) \\
K_1 \mu_b A_b [\Phi'_\psi(L) - \Phi'_\phi(L)] + \omega^2 \frac{\rho_p A_p h_p}{2} \tilde{\Phi}'_u(L) + \frac{E_p A_p h_p}{2} \tilde{\Phi}''_u(L) - C_{11}^D I_p \tilde{\Phi}'_\phi(L) \\
E_b I_b \Phi'_\phi(L) - \frac{E_p A_p h_b}{2} \tilde{\Phi}'_u(0) \\
-\frac{E_p A_p h_p}{2} \tilde{\Phi}'_u(0) + C_{11}^D I_p \tilde{\Phi}'_\phi(0) \\
\frac{E_p A_p h_p}{2} \tilde{\Phi}'_u(L) - C_{11}^D I_p \tilde{\Phi}'_\phi(L)
\end{bmatrix}
\end{aligned}$$

where

$$\begin{aligned}
 \tilde{\Phi}_{\dot{u}}(0) &\equiv \Phi_{\dot{u}}(0) - \frac{h_p}{2} \Phi'_{\dot{v}}(0) - \frac{h_b}{2} \left[ \frac{h_p}{2} \Phi'_{\dot{v}}(0) + \Phi_{\dot{\phi}}(0) \right] \\
 \tilde{\Phi}_{\dot{\phi}}(0) &\equiv \Phi'_{\dot{v}}(0) + \frac{h_b}{2} \Phi''_{\dot{v}}(0) \\
 \tilde{\Phi}_{\dot{u}}(L) &\equiv \Phi_{\dot{u}}(L) - \frac{h_p}{2} \Phi'_{\dot{v}}(L) - \frac{h_b}{2} \left[ \frac{h_p}{2} \Phi'_{\dot{v}}(L) + \Phi_{\dot{\phi}}(L) \right] \\
 \tilde{\Phi}_{\dot{\phi}}(L) &\equiv \Phi'_{\dot{v}}(L) + \frac{h_b}{2} \Phi''_{\dot{v}}(L) \\
 \tilde{\Delta}_{\dot{u}} &\equiv \tilde{\Phi}_{\dot{u}}(L) - \tilde{\Phi}_{\dot{u}}(0)
 \end{aligned}$$

(b) In case of a CPBS with collocated PZT wafers:

$$\text{Actuator } \mathbf{G}(\omega) = \begin{bmatrix}
 -(2\mu_b + \lambda_b)A_b\Phi'_{\dot{u}}(0) - \lambda_b A_b\Phi_{\dot{v}}(0) - E_p A_p \tilde{\Phi}'_{\dot{u}+}(0) \\
 -\kappa_1 \mu_b I_b \Phi'_{\dot{v}}(0) - \omega^2 \frac{\rho_p A_p h_b h_p}{4} \tilde{\Phi}_{\dot{u}+}(0) - \frac{E_p A_p h_b h_p}{4} \tilde{\Phi}_{\dot{u}+}''(0) + \frac{C_{11}^D I_p h_b}{2} \tilde{\Phi}'_{\dot{\phi}-}(0) \\
 -K_1 \mu_b A_b [\Phi'_{\dot{v}}(0) - \Phi_{\dot{\phi}}(0)] - \omega^2 \frac{\rho_p A_p h_p}{2} \tilde{\Phi}_{\dot{u}-}(0) - \frac{E_p A_p h_p}{2} \tilde{\Phi}_{\dot{u}-}''(0) + C_{11}^D I_p \tilde{\Phi}'_{\dot{\phi}+}(0) \\
 -E_b I_b \Phi'_{\dot{\phi}}(0) + \frac{E_p A_p h_b}{2} \tilde{\Phi}'_{\dot{u}-}(0) \\
 (2\mu_b + \lambda_b)A_b\Phi'_{\dot{u}}(L) + \lambda_b A_b\Phi_{\dot{v}}(L) + E_p A_p \tilde{\Phi}'_{\dot{u}+}(L) \\
 \kappa_1 \mu_b I_b \Phi'_{\dot{v}}(L) + \omega^2 \frac{\rho_p A_p h_b h_p}{4} \tilde{\Phi}_{\dot{u}+}(L) + \frac{E_p A_p h_b h_p}{4} \tilde{\Phi}_{\dot{u}+}''(L) - \frac{C_{11}^D I_p h_b}{2} \tilde{\Phi}'_{\dot{\phi}-}(L) \\
 K_1 \mu_b A_b [\Phi'_{\dot{v}}(L) - \Phi_{\dot{\phi}}(L)] + \omega^2 \frac{\rho_p A_p h_p}{2} \tilde{\Phi}_{\dot{u}-}(L) + \frac{E_p A_p h_p}{2} \tilde{\Phi}_{\dot{u}-}''(L) - C_{11}^D I_p \tilde{\Phi}'_{\dot{\phi}+}(L) \\
 E_b I_b \Phi'_{\dot{\phi}}(L) - \frac{E_p A_p h_b}{2} \tilde{\Phi}'_{\dot{u}-}(0) \\
 -\frac{E_p A_p h_b h_p}{4} \tilde{\Phi}'_{\dot{u}+}(0) + \frac{C_{11}^D I_p h_b}{2} \tilde{\Phi}'_{\dot{\phi}-}(0) \\
 -\frac{E_p A_p h_p}{2} \tilde{\Phi}'_{\dot{u}-}(0) + C_{11}^D I_p \tilde{\Phi}'_{\dot{\phi}+}(0) \\
 \frac{E_p A_p h_b h_p}{4} \tilde{\Phi}'_{\dot{u}+}(L) - \frac{C_{11}^D I_p h_b}{2} \tilde{\Phi}'_{\dot{\phi}-}(L) \\
 \frac{E_p A_p h_p}{2} \tilde{\Phi}'_{\dot{u}-}(L) - C_{11}^D I_p \tilde{\Phi}'_{\dot{\phi}+}(L)
 \end{bmatrix}$$

$$\begin{aligned}
\text{Sensor } \mathbf{G}(\omega) = & \left[ \begin{aligned}
& -(2\mu_b + \lambda_b)A_b\Phi'_u(0) - \lambda_b A_b\Phi_\psi(0) - E_p A_p \tilde{\Phi}'_{u+}(0) - \frac{E_p A_p \bar{d}_{31} \bar{h}_{31}}{L} \tilde{\Delta}_{u1} \\
& - \kappa_1 \mu_b I_b \Phi'_\psi(0) - \omega^2 \frac{\rho_p A_p h_b h_p}{4} \tilde{\Phi}_{u+}(0) - \frac{E_p A_p h_b h_p}{4} \tilde{\Phi}_{u+}''(0) + \frac{C_{11}^D I_p h_b}{2} \tilde{\Phi}'_{\phi-}(0) \\
& - K_1 \mu_b A_b [\Phi'_\psi(0) - \Phi'_\phi(0)] - \omega^2 \frac{\rho_p A_p h_p}{2} \tilde{\Phi}_{u-}(0) - \frac{E_p A_p h_p}{2} \tilde{\Phi}_{u-}''(0) + C_{11}^D I_p \tilde{\Phi}'_{\phi+}(0) \\
& - E_b I_b \Phi'_\phi(0) + \frac{E_p A_p h_b}{2} \tilde{\Phi}'_{u-}(0) + \frac{E_p A_p \bar{d}_{31} \bar{h}_{31} h_b}{2L} \tilde{\Delta}_{u2} \\
& (2\mu_b + \lambda_b)A_b\Phi'_u(L) + \lambda_b A_b\Phi_\psi(L) + E_p A_p \tilde{\Phi}'_{u+}(L) + \frac{E_p A_p \bar{d}_{31} \bar{h}_{31}}{L} \tilde{\Delta}_{u1} \\
& \kappa_1 \mu_b I_b \Phi'_\psi(L) + \omega^2 \frac{\rho_p A_p h_b h_p}{4} \tilde{\Phi}_{u+}(L) + \frac{E_p A_p h_b h_p}{4} \tilde{\Phi}_{u+}''(L) - \frac{C_{11}^D I_p h_b}{2} \tilde{\Phi}'_{\phi-}(L) \\
& K_1 \mu_b A_b [\Phi'_\psi(L) - \Phi'_\phi(L)] + \omega^2 \frac{\rho_p A_p h_p}{2} \tilde{\Phi}_{u-}(L) + \frac{E_p A_p h_p}{2} \tilde{\Phi}_{u-}''(L) - C_{11}^D I_p \tilde{\Phi}'_{\phi+}(L) \\
& E_b I_b \Phi'_\phi(L) - \frac{E_p A_p h_b}{2} \tilde{\Phi}'_{u-}(0) - \frac{E_p A_p \bar{d}_{31} \bar{h}_{31} h_b}{2L} \tilde{\Delta}_{u2} \\
& - \frac{E_p A_p h_b h_p}{4} \tilde{\Phi}'_{u+}(0) + \frac{C_{11}^D I_p h_b}{2} \tilde{\Phi}'_{\phi-}(0) - \frac{E_p A_p \bar{d}_{31} \bar{h}_{31} h_b h_p}{4L} \tilde{\Delta}_{u1} \\
& - \frac{E_p A_p h_p}{2} \tilde{\Phi}'_{u-}(0) + C_{11}^D I_p \tilde{\Phi}'_{\phi+}(0) - \frac{E_p A_p \bar{d}_{31} \bar{h}_{31} h_p}{2L} \tilde{\Delta}_{u2} \\
& \frac{E_p A_p h_b h_p}{4} \tilde{\Phi}'_{u+}(L) - \frac{C_{11}^D I_p h_b}{2} \tilde{\Phi}'_{\phi-}(L) + \frac{E_p A_p \bar{d}_{31} \bar{h}_{31} h_b h_p}{4L} \tilde{\Delta}_{u1} \\
& \frac{E_p A_p h_p}{2} \tilde{\Phi}'_{u-}(L) - C_{11}^D I_p \tilde{\Phi}'_{\phi+}(L) + \frac{E_p A_p \bar{d}_{31} \bar{h}_{31} h_p}{2L} \tilde{\Delta}_{u2}
\end{aligned} \right]
\end{aligned}$$

where

$$\begin{aligned}
\tilde{\Phi}_u(0) & \equiv \Phi_u(0) - \frac{h_p}{2} \Phi'_\psi(0) - \frac{h_b}{2} \left[ \frac{h_p}{2} \Phi'_\psi(0) + \Phi'_\phi(0) \right] \\
\tilde{\Phi}_\phi(0) & \equiv \Phi_\psi(0) + \frac{h_b}{2} \Phi_\psi''(0) \\
\tilde{\Phi}_u(L) & \equiv \Phi_u(L) - \frac{h_p}{2} \Phi'_\psi(L) - \frac{h_b}{2} \left[ \frac{h_p}{2} \Phi'_\psi(L) + \Phi'_\phi(L) \right] \\
\tilde{\Phi}_\phi(L) & \equiv \Phi_\psi(L) + \frac{h_b}{2} \Phi_\psi''(L) \\
\tilde{\Phi}_{u+}(0) & = 2\Phi_u(0) - \frac{h_b h_p}{2} \Phi'_\psi(0) \\
\tilde{\Phi}_{\phi+}(0) & = 2\Phi'_\psi(0) \\
\tilde{\Phi}_{u+}(L) & = 2\Phi_u(L) - \frac{h_b h_p}{2} \Phi'_\psi(L) \\
\tilde{\Phi}_{\phi+}(L) & = 2\Phi'_\psi(L) \\
\tilde{\Phi}_{u-}(0) & = -h_b \Phi'_\phi(0) - h_p \Phi'_\psi(0) \\
\tilde{\Phi}_{\phi-}(0) & = h_b \Phi'_\psi(0) \\
\tilde{\Phi}_{u-}(L) & = -h_b \Phi'_\phi(L) - h_p \Phi'_\psi(L) \\
\tilde{\Phi}_{\phi-}(L) & = h_b \Phi'_\psi(L)
\end{aligned}$$

If the polarization directions of collocated PZT wafers are same, i.e.  $\bar{h}_{31} = \underline{h}_{31}$ , then

$$\begin{aligned}\tilde{\Delta}_{\hat{u}1} &\equiv \tilde{\Phi}_{\hat{u}+}(L) - \tilde{\Phi}_{\hat{u}+}(0) \\ \tilde{\Delta}_{\hat{u}2} &\equiv \tilde{\Phi}_{\hat{u}-}(L) - \tilde{\Phi}_{\hat{u}-}(0)\end{aligned}$$

If the polarization directions of collocated PZT wafers are opposite, i.e.  $\bar{h}_{31} = -\underline{h}_{31}$ , then

$$\begin{aligned}\tilde{\Delta}_{\hat{u}1} &\equiv \tilde{\Phi}_{\hat{u}-}(L) - \tilde{\Phi}_{\hat{u}-}(0) \\ \tilde{\Delta}_{\hat{u}2} &\equiv \tilde{\Phi}_{\hat{u}+}(L) - \tilde{\Phi}_{\hat{u}+}(0)\end{aligned}$$

## REFERENCES

Ach73

Achenbach, J.D. Wave Propagation in Elastic Solids, North-Holland Publishing Company, Amsterdam, (1973).

Alf74

Alford, R.M., Kelly, K.R. and Boore, D.M. "Accuracy of finite difference modeling of the acoustic wave equation" . Geophysics, 39 (6), 834–842 (1974).

All92

Alleyne, D.N. and Cawley, P. "Optimization of lamb wave inspection techniques" . NDT and E International, 25: 11–22 (1992a).

All92

Alleyne, D.N. and Cawley, P. "The interaction of lamb waves with defects" . IEEE Transactions on Ultrasonic, Ferroelectrics and Frequency Control, 39(3): 381–387 (1992b).

All01

Alleyne, D.N., Pavlakovic, B., Lowe, M.J.S. and Cawley, P. "Rapid, long-range inspection of chemical plant pipework using guided waves," Review of Progress in QNDE, Vol. 20, pp. 180–187 (2001).

Ant09

Anton, S. R., Inman, D. J., and Park, G. (2009). "Reference-free damage detection using instantaneous baseline measurements." AIAA Journal, Vol. 47, No. 8, pp. 1952–1964 (2009).

Ayr98

Ayres, J. W., Lalande, F., Chaudhry, Z., and Rogers, C. A. "Qualitative impedance-based health monitoring of civil infrastructures," Smart Materials and Structures, Vol. 7, pp. 599–605 (1998).

Bha02

Bhalla, S., Naidu, A. S. K., and Soh, C. K., "Influence of Structure-Actuator Interactions and Temperature on Piezoelectric Mechatronic Signatures for NDE," in Proceedings of ISSS-SPIE 2002 International Conference on Smart Materials Structures and Systems, December 12-14, Bangalore, India paper no ISSS-SA-502 (2002a).

Bha04

Bhalla, S., Soh, C.K.: Structural health monitoring by piezoimpedance transducers: II applications. *J. Aerosp. Eng.* 17(4), 166-175 (2004).

Bol99

Boller, C., Biemans, C., Staszewski, W., Worden, K. and Tomlinson, G. "Structural Damage Monitoring Based on an Actuator-Sensor System," ' In: Proceedings of SPIE Smart Structures and Integrated Systems Conference, Newport CA, March 1-4 (1999).

Bul09

Buli X. "Structural Health Monitoring Instrumentation, Signal Processing and Interpretation with Piezoelectric Wafer Active Sensor." Ph.D. thesis, Imperial Mechanical Engineering College of Engineering & Computing, September (2009).

Caw96

Cawley, P. and Alleyne, D. "The use of Lamb waves for the long range inspection of large structures," *Ultrasonics*, Vol. 34, pp. 287-290 (1996).

Cha95

Chang, F.-K. "Built-In Damage Diagnostics for Composite Structures," ' In: Proceedings of the 10th International Conference on Composite Structures (ICCM-10), Vol. 5, Whistler, B.C., Canada, August 14-18, pp. 283-289 (1995).

Cha95

Chaudhry, Z., Joseph, T., Sun, F., and Rogers, C., "Local-Area Health Monitoring of Aircraft via Piezoelectric Actuator/Sensor

Patches,” in Smart Structures and Integrated Systems, SPIE Conference, San Diego, CA, Proceedings of the SPIE, Vol. 2443 (1995).

Cha99

Chang, F. K. Implementation of a Real-time Impact Identification Technique for Stiffened Composite Panels, in Proceedings of the 2nd International Workshop on Structural Health Monitoring, Stanford University, CA, 225–233 (1999).

Cha01

Chang, F.-K. “Structural Health Monitoring: Aerospace Assessment,” Aero Mat 2001, 12th ASM Annual Advanced Aerospace Materials and Processes Conference, 12–13 June 2001, Long Beach, CA (2001).

Cra74

Crawley, E. F. and Lazarus, K. B., “Induced Strain Actuation of Isotropic and Anisotropic Plates”, AIAA Journal, Vol. 29, No. 6, pp. 944–951 (1991).

Cra87

Crawley, E. F. and de Luis, J., “Use of Piezoelectric Actuators as Elements of Intelligent Structures,” *AIAA Journal*, Vol. 25, No. 10, 1373–1385 (1987).

Cra89

Crawley, E. F. and K. B. Lazarus. “Induced Strain Actuation of Isotropic and Anisotropic Plates”, AIAA Journal, 29(6):944–951 (1989).

Cra90

Crawley, E. F. and Anderson, E. H., “Detailed Models of Piezoceramic Actuation of Beams,” *Journal of Intelligent Material Systems and Structures*, Vol. 1, No. 1, 4–25 (1990).

Cuc07

Cuc, A., Goughiutiu, V., Joshi, S., and Tidwell, Z. “Structural health

monitoring with piezoelectric wafer active sensors for space applications,” AIAA Journal, Vol. 45, No. 12, pp. 2838–2850 (2007).

Dal01

Dalton, R. P.; Cawley, P.; Lowe, M. J. S. (2001) “The Potential of Guided Waves for Monitoring Large Areas of Metallic Aircraft Structure” , *Journal of Nondestructive Evaluation*, Vol. 20, pp. 29–46, (2001).

Doy88

Doyle, J.F. A spectrally formulated finite elements for longitudinal wave propagation. *International Journal of Analytical and Experimental Modal Analysis*, 3, 1–5 (1988).

Doy97

Doyle, J.F. “Wave Propagation in Structures” 2nd edn, Springer-Verlag, New York (1997).

Doy00

Doyle, J.F. Application of the Spectral Element Method to Acoustic Radiation, NASA/CR–2000–210642 (2000).

Ell97

Ellerbrock, P. DC-XA Structural Health Monitoring Fiber-optic Based Strain Measurement System, *Proceedings of the SPIE*, **3044**: 207–218 (1997).

Gaz58

Gazis, D. C. “Exact Analysis of the Plane-strain Vibrations of Thick-walled Hollow Cylinders” , *Journal of the Acoustical Society of America*, **30**: 786–794 (1958).

Gaz59

Gazis, D.C. “Three-dimensional Investigation of the Propagation of Waves in Hollow Circular Cylinders” , *Journal of the Acoustical Society of America*, **31**: 568–578 (1959).

Giu98



Giurgiutiu, V., and Rogers, C. A., 1998a, "Recent Advancements in the Electro-Mechanical (EM) Impedance Method for Structural Health Monitoring and NDE, Proceedings of the SPIE's 5th International Symposium on Smart Structures and Materials, 1-5 March 1998, Catamaran Resort Hotel, San Diego, CA, SPIE Vol. 3329, pp. 536-547 (1998a)

Giu98

Giurgiutiu, V., and Rogers, C. A., "Application of the Electro-Mechanical (E/M) Impedance Method to Machinery Failure Prevention", Proceedings of the 52nd Meeting of the Society for Machinery Failure Prevention Technology, March 30 - April 2, 1998, Cavalier Hotel, Virginia Beach, VA, pp. 271-280 (1998b).

Giu00

Giurgiutiu, V. and Zagrai, A. ' 'Characterization of Piezoelectric Wafer Active Sensors,' ' Journal of Intelligent Material Systems and Structures, 11(12):959 - 976 (2000).

Giu00

Giurgiutiu, V.; Zagrai, A. "Characterization of Piezoelectric afer Active Sensors", Journal of Intelligent Material Systems and Structures, Technomic Pub., USA, Vol. 11, No. 12, December 2000, pp. 959-976 (2000).

Giu00

Giurgiutiu, V.; Zagrai, A. N. "Characterization of Piezoelectric Wafer Active Sensors", Journal of Intelligent Material Systems and Structures, Vol. 11, pp. 959-976, (2000a).

Giu00

Giurgiutiu, V.; Zagrai, A. N. "Damage Detection in Simulated Aging-aircraft Panels Using the Electrico-mechanical Impedance Technique", Adaptive structure and material systems symposium, ASME Winter annual meeting, ASME Winter Meeting, Nov. 5-10, 2000, Orlando, FL (2000b).

Giu01

Giurgiutiu, V.; Bao, J.; Zhao, W. "Active Sensor Wave Propagation Health Monitoring of Beam and Plate Structures", Proceedings of the SPIE' s 8th International Symposium on Smart Structures and Materials, 4–8 March 2001, Newport Beach, CA (2001).

Giu02

Giurgiutiu, V.; Zagrai, A. N.; Bao J.; Redmond, J.; Roach, D.; Rackow, K. "Active Sensors for Health Monitoring of Aging Aerospace Structures" , International Journal of the Condition Monitoring and Diagnostic Engineering Management, UK, Vol. 5, No. 3, August (2002).

Giu02

Giurgiutiu, V. and Zagrai, A. "Embedded Self-Sensing Piezoelectric Active Sensors for On-Line Structural Identification" , ' ASME Journal of Vibration and Acoustics, 124:116–125 (2002).

Giu03

Giurgiutiu, V., Zagrai, A. N., Bao, J., Redmond, J., Roach, D., Rackow, K., "Active Sensors for Health Monitoring of Aging Aerospace Structures," International Journal of the Condition Monitoring and Diagnostic Engineering Management, Vol. 6, No. 1, 3 21 (2003).

Giu03

Giurgiutiu, V., "Embedded NDE with Piezoelectric Wafer Active Sensors in Aerospace Applications," Journal of Materials (JOM-e), Special Issue on NDE, Vol. 55, No. 1 ( 2003).

Giu04

Giurgiutiu, V., Zagrai, A., and Bao, J. "Damage identification in aging aircraft structures with piezoelectric wafer active sensors," Journal of Intelligent Material Systems and Structures, Vol. 15, No. 9–10, pp. 673–687 (2004).

Giu05

Giurgiutiu, V., Zagrai, A.: "Damage detection in thin plates and

aerospace structures with the electro-mechanical impedance method” . Int. J. Struct. Health Monit. 4(2), 99–118 (2005).

Gop94

Gopalakrishnan, S. and Doyle, J. F. “Wave propagation in connected waveguides of varying cross-section” . Journal of Sound and Vibration, 175 (3), 347–363 (1994).

Gra75

Graff, K.F., Wave Motions in Elastic Solids, Dover Publications, Inc (1975).

Hau99

Hautamaki, C., Zurn, S., Mantell, S. C., and Polla, D. L. “Experimental Evaluation of MEMS Strain Sensors Embedded in Composites” , Journal of Microelectromechanical Systems, 8(3): 272–279. Seydel, R. E., and (1999).

Ihn02

Ihn, J.-B. and Chang, F.-K. ‘ ‘Built-in Diagnostics for Monitoring Crack Growth in Aircraft Structures,’ ’ In: Proceedings of the SPIE’ s 9th International Symposium on Smart Structures and Materials, 17–21 March 2002, San Diego, CA, Paper #4702–04 (2002).

Ihn08

Ihn, J.B. and Chang, F.K. “Pitch-catch active sensing methods in structural health monitoring for aircraft structures,” Structural Health Monitoring, Vol. 7, No. 1, pp. 5–15 (2008).

Kei95

Keilers, C. H., and Chang, F-K. “Identifying Delamination in Composite Beam Using Built-in Piezoelectrics” , Journal of Intelligent Material Systems and Structures, 6(5): 647–672 (1995).

Kes02

Kessler, S. S., “Piezoelectric-based *In Situ* Damage Detection of Composite Materials for Structural Health Monitoring Systems,” Ph.D. Dissertation, MIT, Cambridge, MA (2002).

Kes04

Kessler, S. S., Spearing, M. S., Shi, Y., and Dunn, C. "Packaging of Structural Health Monitoring Components", Proceedings of the SPIE, **5391**: 219–229 (2004).

Kes05

Kessler, S. S. and D. J. Shim, "Validation of a Lamb wave-based structural health monitoring system for aircraft applications," in Proc. SPIE 12th Int. Symp. Smart Structures and Materials, vol.5765, pp. 293–301 (2005).

Kim07

Kim, S. B. and Sohn, H., "Instantaneous Reference-free Crack Detection Based on Polarization Characteristics of Piezoelectric Materials," Smart Materials and Structures 16(6), 2375–2387 (2007).

Kol98

Kollar, L., and Steenkiste, R. J. Calculation of the Stresses and Strains in Embedded Fiber Optic Sensors, Journal of Composite Materials, **32**(18): 1647–1679 (1998).

Kra90

Krautkramer, J. and Krautkramer, H., Ultrasonic Testing of Materials, Springer-Verlag, Berlin (1990).

Kud93

Kudva, J. N., Marandis, C., and Gentry, J., "Smart Structures Concepts for Aircraft Structural Health Monitoring," Proceedings of the SPIE, Vol. 1917, 964–971 (1993).

Lam17

Lamb H. "On Waves in an Elastic Plate." Proceedings of the Royal Society of London. Series A, Containing Papers of a Mathematical and Physical Character, v.93, n.651, 1917, 293–312 (1917).

Lee00

Lee, U. "Vibration analysis of one-dimensional structures using the spectral transfer matrix method" . *Engineering Structures*, 22 (6), 681–690 (2000).

Lee01

Lee, U. (2001) Dynamic characterization of the joints in a beam structure by using spectral element method. *Shock and Vibration*, 8(6), 357–366.

Lia93

Liang, C., F. P. Sun and C. A. Rogers. "An Impedance Method for Dynamic Analysis of Active Material Systems" , accepted by ASME *Journal of Vibration and Acoustics*, also in *Proceedings*, 34th SDM Conference, LaJolla, CA, April 19–21, 1993, pp. 3587–3599 (1993).

Lia94

Liang C, Sun FP, Rogers C.A, "Coupled electro-mechanical analysis of adaptive material systems-determination of the actuator power consumption and system energy transfer", *Journal of Intelligent Material Systems and Structures*, Vol. 5, No. 1, pp. 12–20 (1994).

Lin01

Lin, X. and Yuan, F.G. ' 'Diagnostic Lamb Waves in an Integrated Piezoelectric Sensor/Actuator Plate: Analytical and Experimental Studies,' ' *Smart Materials and Structures*, 10: 907–913 (2001a).

Lin01

Lin, X. and Yuan, F.G. ' 'Damage Detection of a Plate using Migration Technique' ' , *Journal of Intelligent Material Systems and Structures*, 12(7) (2001b).

Liu03

Liu, T., Veidt, M., and Kitipornchai, S. "Modeling the Input-output Behavior of Piezoelectric Structural Health Monitoring Systems for Composites Plates," *Smart Materials and Structures*, Vol. 12, 836–844 (2003).

Liu09

Liu X L and Jiang Z W 2009 “Design of a PZT patch for measuring longitudinal mode impedance in the assessment of truss structure damage” , Smart Mater. Struct. **18** (2009) 125017 (8pp)

Lov26

Love, A. E. H. Some Problems of Geodynamics, Cambridge University Press, Cambridge (1926).

Lov44

Love, A. E. H., A Treatise on the Mathematical Theory of Elasticity, Dover, New York (1944).

Min51

Mindlin RD, Herrmann G, A one-dimensional theory of compressional waves in an elastic rod. Proceedings of the First US National Congress of Applied Mechanics, Chicago, 1951, 187–191 (1951)

Mou97

Moulin, E., Assaad, J., Delebarre, C., Kaczmarek, H., and Balageas, D., “Piezoelectric Transducers Embedded in a Composite Plate: Application to Lamb Wave Generation,” *Journal of Applied Physics*, Vol. 82, No. 5, 2049–2055 (1997).

Nar78

Narayanan, G.V.and Beskos, D.E. “Use of dynamic influence coefficients in forced vibration problems with the aid of fast fourier transform” . Computers & Structures, 9 (2), 145–150 (1978).

Ost09

Ostachowicz et al. 2009

Par00

Park, G., Cudney, H., Inman, D.J.: “Impedance-based health monitoring for civil structural components” . J. Infrastruct. Syst.,

ASCE 6(4), 153–160 (2000).

Par03

Park G, Sohn H, Farrar CR, Inman DJ., “Overview of piezoelectric impedance-based health monitoring and path forward.” , The Shock and Vibration Digest 35, 451–463 (2003).

Par03

Park, S.; Yoo, J. (2003b) “Electrochemical Impedance Spectroscopy for Better Electrochemical Measurements” , American chemical Society–Analytical Chemistry, P455–461, Nov, 1, (2003).

Par03

Park, G., Sohn, H., Farrar, C.R., and Inman, D.J. (2003a) “Overview of Piezoelectric Impedance-based Health Monitoring and Path Forward” , The Shock and Vibration Digest, Vol. 35, Issue 6, pp. 451–463, (2003).

Par05

Park, S., Yun, C. B., Roh, Y., and Lee, J. J. “Health monitoring of steel structures using impedance of thickness modes at PZT patches,” Smart Structures and Systems, Vol. 1, No. 4, pp. 339–354 (2005).

Par06

Park, S., Ahmad, S., Yun, C.–B., Roh, Y. “Multiple crack detection of concrete structures using impedance-based structural health monitoring techniques” . Exp. Mech. 46(5), 609–618 (2006).

Par06

Park, S., Yun, C.B., Roh, Y., and Lee, J.J. “PZT-based active damage detection techniques for steel bridge components,” Smart Materials and Structures, Vol. 13, No. 5, pp. 873–879 (2006).

Par07

Park, H. W., Sohn, H., Law, K. H., Farrar C. R. “Time reversal active sensing for health monitoring of a composite plate,” Journal of Sound and Vibration 302–306 (2007).

Par09

H. W. Park, S. B. Kim, and H. Sohn, "Understanding a time reversal process in Lamb wave propagation," *Wave Motion*, vol. 46, no.7, pp. 451–467, Nov. 2009.

Pak10

Park S., Lee C.G. and Sohn H. "Reference-free crack detection using transfer impedance," *Journal of Sound and Vibration* 329(12), 2337–2348 (2010).

Par10

Park, H.W., Lim, K. L., Kim, E. J. and Sohn, H., "Spectral element formulation for dynamic analysis of a coupled piezoelectric wafer and beam system," *Journal Computers & Structures* 88(9–10), 567–580 (2010).

Pra04

Prasad, S.M., Balasubramaniam, K., and Krishnamurthy, C. "Structural health monitoring of composite structures using Lamb wave tomography," *Smart Materials and Structures*, Vol. 13, No. 5, pp. 873–879 (2004).

Rag07

Raghavan, A. and Cesnik, C. E. S., "Review of guided-wave structural health monitoring," *The Shock and Vibration Digest* 39(91), 91–114 (2007).

Ray87

Rayleigh, J. W. S. "On Waves Propagated Along the Plane Surface of An Elastic Solid" , *Proceedings of the London Mathematical Society*, **17**: 4–11 (1987).

Ree92

Rees, D., Chiu, W. K., and Jones, R. "A Numerical Study of Crack Monitoring in Patched Structures Using a Piezo Sensor" , *Smart Materials and Structures*, **1**(3): 202–205 (1992).



Ros94

Rose, J.L., Ditri, J.J., Pilarski, A., Rajana, K., and Carr, F.T. "A guided wave inspection technique for nuclear steam generator tuning," *NDT&E International*, Vol. 27, pp. 307–310 (1994).

Ros99

Rose, J. L. *Ultrasonic Waves in Solid Media*, Cambridge University Press, Cambridge (1999).

Sch42

Scholte, J. G. On the Stoneley Wave Equation, *Proc. Kon. Nederl. Akad. Wetensch.*, **45**(20–5): 159–164 (1942).

Sch98

Schoess, J. N., and Zook, J. D. Test Results of Resonant Integrated Microbeam Sensor (RIMS) for Acoustic Emission Monitoring, *Proceedings of the SPIE Conference on Smart Electronics and MEMS*, **3328**: 326–332 (1998).

Soh07

Sohn, H., "Effects of Environmental and Operational Variability on Structural Health Monitoring," *Philosophical Transactions of the Royal Society A* 365(1851), 539–560 (2007).

Soh07

Sohn, H., Park, H. W., Law, K. H., Farrar, C. R., "Combination of a time reversal process and a consecutive outlier analysis for baseline-free damage diagnosis," *J. Intel. Mater. Smart Struct.* 18(4), 335–346 (2007).

Soh10

Sohn, H., Kim, S.B.: Development of dual PZT transducers for instantaneous crack detection in thin plate structures. *IEEE Trans. Ultrason. Ferroelectr. Freq. Control* 57(1), 229–240 (2010)

Spy82

Spyrakso, C.C. and Beskos, D.E. "Dynamic response of frameworks by fast fourier transform. Computers & Structures" , 15 (5), 495–505 (1982).

Sta03

Staszewski W. J., Lee B. C., Mallet L. and Scarpa F. 2003. " Structural health monitoring using scanning laser vibrometry: I. Lamb wave sensing." Smart Mater. Struct. 13 251–260 (2003).

Sto24

Stoneley, R. "Elastic Waves at the Surface of Separation of Two Solids" , Proceedings of the Royal Society of London, Series A, **106**: 416–428 (1924).

Sun95

Sun, F.P., Chaudhry, Z., Liang, C., and Rogers, C.A., "Truss Structure Integrity Identification Using PZT Sensor-Actuator," Journal of Intelligent Material Systems and Structures, Vol. 6, 134–139 (1995a).

Sun95

Sun F P, Chaudhry Z, Rogers C A, Majmunder M and Liang C 1995 "Automated real-time structural health monitoring via signature pattern recognition" Proc. SPIE 2443 236–247 (1995).

Sun95

Sun, F., Roger, C.A., and Liang, C., "Structural Frequency Response Function Acquisition via Electric Impedance Measurement of Surface-Bonded Piezoelectric Sensor/Actuator," in Proceedings of the 36th AIAA/ASME/ASCE/AHS/ASC Structures, Structural Dynamics, and Materials Conference, 3450–3461 (1995b).

Sun00

Sun, Z., Mao, Y., Jiang, W., and Zhang, D. "Investigation on Interaction of Lamb Waves and Circumferential Notch in Pipe by Means of Wavelet Transform" , Proceedings of the IEEE Ultrasonics Symposium, Vol. 1, San Juan, Puerto Rico, 827–830 (2000).

Tho02

Thomson, D. O. and Chimenti, D. E. (Editors) (2002) Review of Progress in Quantitative Nondestructive Evaluation, Chapter 2C “Guided Waves” and Chapter 7 “NDE Applications”, AIP Conference Proceedings Vol. 615, (2002).

Tua05

Tua, P., Quek, S., and Wang, Q. “Detection of cracks in cylindrical pipes and plates using piezo-actuated Lamb waves, Smart Materials and Structures,” Vol. 14, No. 6, pp. 1325–1342 (2005).

Van95

Van Way, C. B., Kudva, J. N., Schoess, J. N., Zeigler, M. L., and Alper, J. M., “Aircraft Structural Health Monitoring System Development Overview of the Air Force/Navy Smart Metallic Structures Program,” *Proceedings of the SPIE*, Vol. 2443, 277–284 (1995).

Vik67

Viktorov, I. A. Rayleigh and Lamb Waves, Plenum Press, New York. (1967).

Wan96

Wang X.M., Ehlers, C., and Neitzel, M., “Electromechanical Dynamic Analysis of the Piezoelectric Stack,” Smart Materials and Structures, Vol. 5, 492–500 (1996).

Wan99

Wang, C. S. and Chang, F-K. “Built-in Diagnostics for Impact Damage Identification of Composite Structures,” in Structural Health Monitoring 2000, Fu-Kuo Chang, ed., Technomic, Lancaster, PA, 612–621 (1999).

Wai04

Wait, J.R., Park, G., Sohn, H., and Farrar, C.R. “Active sensing system development for damage prognosis,” Proceedings, 1st international workshop on Advanced Smart Materials and Smart

Structures Technology, pp. 163–170, Honolulu, HI (2004).

Wil01

Wilcox, P. D., M. Lowe, J. S. and P. Cawley, “Mode and transducer selection for long range Lamb wave inspection,” *J. Intell. Mater. Syst. Struct.*, vol. 12, no. 8, pp. 553–565, Aug. (2001).

Wor61

Worlton, D. C. “Experimental Confirmation of Lamb Waves at Megacycle Frequencies” , *Journal of Applied Physics*, 32(6): 967–971 (1961).

Yan08

Yang Y, Lim Y Y and Soh C K, “Practical issues related to the application of the electromechanical impedance technique in the structural health monitoring of civil structures: I. Experiment,” *Smart Mater. Struct.* 17 (2008) 035008 (14pp)

Zag01

Zagrai, A.N., and Giurgiutiu, V., “Electromechanical Impedance Method for Crack Detection in Thin Plates,” *Journal of Intelligent Material Systems and Structures*, Vol. 12, 709–718 (2001).

Zag02

Zagrai, A.N. (2002) “Piezoelectric–Wafer Active Sensor Electro–Mechanical Impedance Structural Health Monitoring” , Ph.D. dissertation, University of South Carolina, (2002).

Zha07

Zhao, X., Gao, H., Zhang, G., Ayhan, B., Yan, F., Kwan, C. and Tomlinson, G., 1999, “Active health monitoring of an aircraft wing with embedded piezoelectric sensor/actuator network: I. Defect detection, localization and growth monitoring,” *Smart Mater. Struct.* 16 1208–1217 (2007).

## Summary (In Korean)

### 요 약 문

판 구조물의 무기저 손상 탐지를 위한 압전소자와 보체계(CPBS)의 동탄성학적인 해석을 제안한다. 특히, 손상해석에 사용되는 전기역학적 신호의 이론적인 분석을 판구조물의 모드 특성의 관점에서 분석하고, 판 구조물의 초기 조건과 관련된 기저 신호를 사용하는 기존의 임피던스 기반 손상 감지 기법의 한계점을 극복하기 위해 다음과 같은 연구를 수행하였다.

본 논문에서는 램파와 전기역학적 신호의 동탄성학적인 상관성을 이용하여 전기역학적 신호를 이해한다. 램파와 전기역학적 신호들의 상관관계가 파 중첩과 시간 스펙트럼(temporal spectrum)을 통해 정량적으로 규명된다. 판 구조물에 병치된 한쌍의 동일 PZT 는 극성으로 모드 변환된 램파 신호를 추출하는 것이 가능하다. 모드 변환 신호의 일련의 시간창(time window)에 대한 FFT(fast Fourier transform)를 통해, 시간 스펙트럼의 수렴은 가진주파수 범위내에서 판 구조물의 공진에 귀착됨을 보인다. 시간 스펙트럼의 RMS(root mean square)는 손상과 관련된 신호대 잡음비가 시간창 크기의 증가에 따라 증폭됨을 의미한다. 이 점에서, 모드변환된 램파 신호들은 판 구조물의 손상진단을 위한 전기 역학적 신호들로 통합된다.

병치 압전소자와 보체계(CPBS)를 위한 스펙트럼 요소가 주파수 영역에서 전기역학적 신호들을 계산하기 위해 정식화 된다. Euler-Bernoulli beam 이론과 1 차원 선형 압전성이 PZT 의 전기-역학적 거동을 모사하기 위해 사용된다. 고주파 대역에서 질량관성 효과와 전단변형 효과를 고려한 Mindlin-Herrmann 과 Timoshenko beam 이론이 기저보에 각각 적용된다. 제안된 SE 해석의 타당성이 FE 해석에 의한 수치결과와

실험 결과들로부터 검증된다. 마지막으로, 모드변환된 전기 역학적 신호들의 손상의 위치와 크기에 따른 영향이 SE 해석을 사용한 매개변수 연구(parameter study)를 통해 규명된다. 매개변수 연구에서, 판 구조물의 전기역학적 신호를 이용한 무기저 손상진단의 가능성이 제시된다.

Key Words: 동탄성(Elasto-dynamic), 램파(Lamb wave), 전기역학적 임피던스(Electro-mechanical impedance), 판 구조물(Plate), 병치 압전소자와 보체계 (Coupled PZT-beam system), 통합적 손상진단, 시간 스펙트럼(temporal spectrum), 스펙트럼 요소(Spectral element), 유한요소(Finite element), 평균제곱근(Root mean square)